Experimental Characterization of Commercially Available Carbon Nanotube Fibre in a Stiffness-Variable Actuator Design

A thesis submitted

in partial fulfillment of the requirements for the degree of

MASTER OF APPLIED SCIENCE

in Biomedical Engineering

By

Justin Dalrymple

March 2023

Ottawa-Carleton Institute for Biomedical Engineering

Department of Mechanical Engineering

University of Ottawa

Ottawa, Ontario, Canada K1N 6N5

Abstract

The growing demand for compact and compliant mobility assistive devices has driven interest in low-profile actuating technologies. With the increasing mobility needs of an aging population, such devices could meet this growing market if they can provide low power capabilities, high strength, and compatibility with standard industrial fabrication processes. As a result, researchers have been investigating smart materials, such as carbon nanotube (CNT) and their higher-order structures, as potential components for soft actuator systems.

However, reported works using this material within actuators have remained limited due to the material's prohibitive cost and fabrication complexity. Furthermore, presented actuator designs are difficult to compare due to custom fabrication procedures and inconsistent characterizations. The recent availability of commercial higher-order CNT products and the superior material consistency they provide present an opportunity to comprehensively analyze these materials in actuators without the challenges faced in previous work.

This thesis addressed this opportunity by evaluating a stiffness-variable actuator design leveraging a commercially available CNT fibre. The evaluation focused on the effects on the mechanical and electrical properties in addition to its electrothermal and electromechanical responses when changing selected actuator design and operational parameters. The findings highlight the importance of optimal coating and embedded pre-stretch to achieve optimal contractile stress and contractile strain performance, while increased fibre diameter diminishes these properties. Furthermore, the usage of commercial CNT yarn ensured consistent mechanical and electrical properties during the fabrication and testing of actuator prototypes.

This in-depth understanding of this actuator design's strengths, weaknesses, and the influence of selected operational and design parameters on performance establishes a foundation for future CNT-based actuator research within a repeatable framework.

Acknowledgements

The road to completing this master's thesis has been highly insightful and longer than expected but rewarding in many ways. It allowed me to get into the details of this particular field and build foundational knowledge that I could leverage in various external research opportunities, creating a more well-rounded research experience. Especially during the time I undertook this thesis, it would not have been possible without support from many persons along the way, the first of which is my supervising professor Dr. Marc Doumit. Your guidance and flexibility encouraged me in this non-linear journey and were imperative to my success. I cannot thank you enough for your patience and faith in my abilities to achieve this endeavour.

Additionally, I would like to express my gratitude towards the faculty and the many supporting staff I've interacted with throughout this time. From helping me obtain external funding to providing practical insights into my research topic, many aspects of my time here would not be possible without their support. Particularly professor Dr. Natalie Baddour and Leo Denner. You both helped me in countless ways, always open to hearing my ideas and willing to help me accomplish whatever crazy idea I had at the time. Similarly, my lab mates who listened to my problem-solution rollercoaster and always lent words of encouragement.

During this time, I had the opportunity to work with many industry mentors, aiding me in testing these theoretical ideas in practical applications, particularly within the space industry. Without the support, guidance, and, simply put, life advice from people like Dr. David Andrew Green, Dr. Aidan Cowley, and Dr. Cornelia Altenbuchner, I would never have had the chance to explore the many niches within this amazing field or honed in on the specific areas of interest that I foresee myself delving into in the future.

Lastly, I want to thank my family and friends who have supported me throughout my academic endeavours since day one. I promise to continue learning as many new things as possible to bolster my fact attacks when you're least expecting it.

Table of Contents

Acronyms

CNT Carbon Nanotube

CNT-HS Carbon Nanotube High-strength

EAP Electroactive Polymer

MD Coil Mean Diameter

MWCNT Multi-walled Carbon Nanotube

PEO Poly(ethylene Oxide)

PET Poly(ethylene Terephthalate)

PU Polyurethane

SBE Soft-bodied Exosuit

SI Spring Index

SMA Shape Memory Alloy

SMP Shape Memory Polymer

TCP Twisted-coiled Polymer

List of Figures

List of Tables

Chapter 1

Introduction

Interest in mobility assistive device research has steadily grown over the past decade with the development of lightweight materials and high-performance electronics. These devices aim to deliver economic benefits and enhanced user independence over personnel assistance, lending themselves to medical, industrial, and defence industries. Traditionally, assistive devices have taken the form of rigid scaffolds to provide structure and support to various joint areas of the body. However, their overbearing design, and cost have limited adoption [1, 2]. As an alternative, soft-bodied exosuits (SBEs), which provide partial support and rely on flexible materials, have gained attention due to their smaller footprint and superior user comfort [3]. Within this subfield, the most commonly reviewed SBE designs utilize tether, pneumatic or hybrid systems to drive actuation, and while effective, they are dependent on bulky components such as bowden cables or pressure tanks, countering the overarching goal of a low-profile device.

In the search for smaller and simple actuators, composites known as actuating textiles offer a low-profile solution key to the attractiveness of SBEs. These innovative materials are small actuating components that take advantage of the emergent properties of active material networks and are easily integrated into other fabrics. A variety of active materials can be used as their core components, such as shape memory polymers [4, 5, 6, 7] and shape memory alloys [8, 9] whose actuation can be driven and reversed consistently, both of which are effective within robotic applications. Still, these active materials commonly suffer from low cycle times [10, 11], which are not conducive for dynamic real-time systems.

Conversely, active materials built from carbon-based materials such as carbon

nanotubes (CNTs) have demonstrated faster cycle times, in addition to other desirable characteristics such as high strength-to-weight ratios and high conductivity [10,11]. As such, carbon-based actuators have garnered substantial attention and are widely reported in the literature. Though few are reported in a textile format compared to their counterparts, none have explicitly investigated SBE applications - presumably due to cost [12]. Furthermore, reported designs often focus on the experimental development of the CNTs, not lending themselves to commercial applications due to the significant material developmental cost and emergent property unknowns. Without an adequate understanding of the commercial CNT landscape in the context of an actuator component, particularly their costs and properties, any real-world applications will be limited due to perceived infeasibility.

1.1 Objective

To this aim, this thesis has three objectives. The first is to study the mechanical and electrical properties of a commercially available CNT product and how its foundational properties change throughout the various stages of the actuator fabrication process. The second is to develop a fabrication procedure that generates actuators with consistent properties. Finally, the last objective is to characterize the electromechanical and electrothermal responses of various stiffness-variable actuator prototypes under isolated fabrication and operational parameters to determine their relationship with the actuator's overall performance.

1.2 Methodology

In order to achieve the thesis objectives, a four-part methodology was applied to guide the research activities effectively. The first was to quantify the material's reference properties by analyzing the commercial yarn's electrical and mechanical properties in response to uniaxial loading before converting it to an active material. The second was to evaluate the commercial yarn's electrical and mechanical properties while in a twisted state and undergoing uniaxial loading, determining any changes in behaviour due to the spring-like geometry. The third was to apply an epoxy coating procedure on the pre-stretched twisted yarn resulting in a stiffness-variable actuator, and examine its electromechanical responses when electrically stimulated. Lastly was to evaluate the effects of various fabrication and operating condition modifications to determine how they modulate its actuating performance.

1.3 Contribution

This thesis provides a comprehensive literature review of CNT-based actuators, including their design, fabrication processes, actuating mechanisms and the various strengths and weaknesses that result. This review emphasizes the lack of collective characterization of this group of actuators, particularly the lack of commercial product usage, limiting the repeatability of fabrication. Furthermore, it reviews the most performant designs, particularly composites that use twisted and coiled geometries, and highlights a selection of key operational parameters that play a significant role in such an actuator design. These include the applied voltage, precursor fibre diameter, pre-stretch of the coiled sample, and the guest material used during the manufacturing procedure. With this information, a fabrication apparatus is built to selectively control these parameters, resulting in actuators with consistent capabilities.

Subsequently, this thesis provides a two-part experimental mechanical and electrical characterization of the commercially available DexMat CNT fibre, and the PRO-SET® epoxy guest material to identify relationships between these isolated materials and their operating parameters. This analysis includes effects on their stiffness under passive conditions, details missing from previous actuator investigations in the literature.

Finally, a comprehensive experimental evaluation is performed on DexMat CNT yarn-based stiffness-variable actuators, revealing the relationships between their resulting performance and the isolated fabrication and operation parameters. Based on this evaluation, various trade-offs were identified and shown to hinder or enhance various actuating behaviours, including the highest generated stresses and strains.

1.4 Outline

This thesis is structured into six chapters as follows:

Chapter 1 introduces the motivation behind the need for a comprehensive analysis of a commercially available CNT yarn and fibre as a viable component for linear actuators, the objectives, methodology, contributions and outline of this thesis.

Chapter 2 presents a review of the literature and is organized into four main sections. It begins with a description of traditional actuating materials and the

more emergent field of active materials. This is followed by a comparison between CNTs and other electroactive polymer (EAP) actuating materials, and a description of the selected commercial DexMat Galvron™ CNT products and their properties. Next, it covers various actuator design considerations, highlighting their role in a prospective actuator's capabilities and behaviours. Lastly, it gives a brief overview of the current state of electrically driven CNT-based actuators, emphasizing the strengths and weaknesses of their respective designs.

Chapter 3 describes the experimental setup in three sections. The first reviews the electrothermally-driven stiffness-variable actuator design selected to be investigated. The second covers the fabrication apparatus, its design, capabilities and limitations, as well as its corresponding validation through the creation of consistently manufactured actuators. Lastly, the selection of tests and their corresponding procedures used for the experimental evaluations are detailed.

Chapter 4 presents an experimental characterization of the two components within the stiffness-variable actuator design. The first section investigates the precursor DexMat 100 μm Galvron™ CNT fibre in various stages of the fabrication process, evaluating its mechanical, electrical and thermal properties compared to values reported by the manufacturer. Subsequently, an investigation of the PRO-SET® epoxy guest material is presented, looking at the material's mechanical and electrical properties under variable temperature operating conditions and material thicknesses. The results of these characterizations are summarized to identify trends corresponding to the isolated component's fabrication properties.

Chapter 5 presents an experimental evaluation of a stiffness-variable actuator built from the DexMat Galvron™ CNT products designed with various fabrication parameters and tested with various operational conditions. Each of these parameters is isolated into sub-chapters, which include any unique fabrication processes and testing setups required to illustrate their particular effects on the overall actuator electromechanical performance. This evaluation comprised multiple tests, including resistivity, electrothermal response, and electromechanical response through isometric and isotonic tests. The results of these tests are summarized to identify the numerous parameters responsible for enhancing or diminishing specific actuating behaviours.

Chapter 6 reviews the results and contributions of this thesis and presents concluding remarks regarding the actuator's design and performance contrasted against the reported capabilities of related actuators. This discussion highlights the key

areas that benefited from using the DexMat Galvron™ products and presents an objective argument for the viability of these commercially available materials for larger applications. Lastly, a discussion of future work to improve the development and testing of these actuating actuators is also presented.

Chapter 2

Background

This chapter presents a literature survey to provide context for the concepts pertinent to this thesis. The presented materials are divided into four sections: traditional soft-bodied actuator technologies used within assistive devices, an overview of commonly reported active materials, an overview of CNTs as actuator components and a review of existing CNT-based actuator designs. Section 2.1 discusses the range of applications for traditional actuator materials and the challenges associated with each. Section 2.2 presents the novel area of active materials and highlights how they can fill the gaps endemic to traditional technologies. Section 2.3 presents an overview of CNTs as actuator components, their properties, actuating mechanisms and the particular commercial product utilized as the foundational material for this thesis. Finally, Section 2.4 reviews existing CNT-based actuators, noting their design considerations and potential given an improved characterization of their underlying materials.

2.1 Traditional Actuating Technologies

Traditional actuators used with mobility assistive devices today commonly employ one of three primary drivers to support their actuation: electrical, pneumatic or hydraulic.

Electrical systems offer the smallest and simplest designs by reducing power source and device complexity. Using a universal power source allows the designs to take advantage of a wider selection of configurations without much additional complexity. Although auxiliary electrical systems such as motors and batteries contribute to the overall size of these systems, they are comparably smaller than their pneumatic and hydraulic-based counterparts. Moreover, careful selection of the output power can significantly reduce the system's overall size and is a crucial area of improvement as underlying components such as batteries are developed and miniaturized.

Pneumatic systems leverage compressed air to drive the actuation of various components. These systems are slightly more complex than their electrical counterparts and often smaller than comparable hydraulic systems. While they still require more bulky equipment than electrical systems, the open-loop design reduces complexity compared to their hydraulic counterparts. However, this benefit also comes at the cost of lower pressure generation, reducing the resulting power outputs of the system. Similarly, without the natural lubrication of fluid, these systems suffer higher frictional resistances, reducing their operating efficiencies than hydraulic systems.

Hydraulic systems operate similarly to pneumatic systems by leveraging a hydraulic liquid instead of air. This fluid change allows for greater power outputs and faster delivery speeds due to the incompressible nature of fluids. However, reliance on these fluids also necessitates sufficient storage equipment and a closed-loop system increasing complexity, size, and weight. Additionally, certain hydraulic fluids suffer from temperature variance and potential toxicity, reducing their safety for human device usage.

These technologies offer sufficient actuation support but present numerous drawbacks not conducive to many applications, particularly those of a biomedical nature. This has further driven the desire for smaller, low-powered, increasingly flexible systems. Such novel devices designed with compliance in mind are capable of greater efficiencies and power-to-weight ratios, which are well suited to the future of biomedical device development.

2.2 Active Materials

Active materials are a family of materials that embody properties capable of mechanical change when introduced to a particular stimulus. Typically, they are stimulated with electrical, thermal, or chemical energy sources and can generate consistent behaviours. Compared to the more traditional actuating devices mentioned previously, these are commonly small-scale, offering a unique opportunity to build complex actuating systems by utilizing smaller building blocks. This ground-up approach also allows for an exponential increase in the applications that could utilize these technologies owing to their size. From millimetre scale sensors to active textiles, their unique properties promote countless applications generally less amiable to larger actuating technologies. While this family encompasses a large collection of materials, the most often reported fall within the subcategories of shape memory alloys (SMAs), shape memory polymers (SMPs), and electroactive polymers (EAPs).

SMAs are alloy metals which are often composed of zinc, copper, gold, iron, nickel, aluminum or titanium [13] and have a shape-setting behaviour when introduced to a specific high temperature. After setting, any mild deformation at a lower temperature can be reversed to its original state through high-temperature re-exposure. Due to their metallic nature, they have the benefit of being conductive, which lends itself to applications where self-sensing properties are desired [14]. This property also aids thermal transfer when stimulated, which can be driven using direct sources such as joule heating. As an actuator, their shape memory abilities can be leveraged by setting the material into a spring-like structure. While this is the most common design, more unique shapes can be leveraged for a particular desired motion [15, 16].

Generally, cycle times for actuators built with these materials tend to average approximately 2-10 s [11,17], making them unfeasible for real-time quick draw applications. This is primarily due to their thickness, as it takes longer to heat and cool a larger object. However, this size provides the structural integrity of the overall material. In instances where researchers have attempted to reduce the cross-section of these materials to improve this cycle time, the mechanical integrity of the material dropped substantially [18], outlining the underlying limitation of these materials. Moreover, as a consequence of the underlying metal material, SMAs are commonly stiff depending on their set geometry, which can be a benefit depending on the application.

Similarly, SMPs are a family of materials that can also utilize heat-setting, though over a more limited "memory" range. When exposed to a high temperature, they undergo internal chemical cross-linking that imprints their current formation into the polymer once cooled. Analogous to SMAs, they can shift between their relaxed

and set state when exposed to a higher temperature.

Compared to SMAs, SMPs generally require external heating sources as they are often non-conductive and suffer from similar low cycle times due to their reduced thermal conductivity. Additionally, actuation with these materials must incorporate counter loads to return them to their unattenuated states. However, their elastic nature provides additional flexibility compared to the stiffness of the SMAs and allows them to form tighter structures, such as coils, which can significantly increase their mechanical performances [19].

The subgroup of EAPs actively deform through charge manipulation within the material and include a wide variety of materials that handle this process differently. Typically, this manipulation can be accomplished through direct electrical or ionic stimuli. With direct electrical stimulation, the material experiences an increase in electrostatic forces between itself or another material, triggering a relative attraction or repulsion behaviour as the charges along the materials are displaced. With ionic mechanisms, the material is placed in contact with an ionic substance which facilitates the transfer of ions into the EAP, either through direct contact or an electrical field. The sorption of ions causes swelling of the material and, consequently, a longitudinal compression. Each of these methods can be influenced by geometry and allow for unique activation behaviours depending on the underlying actuator shape as it undergoes this swelling and unswelling cycle.

While these inexpensive mechanisms require low power and can generate consistent actuation behaviours when employed, their effectiveness strongly relies on the underlying material's ability to translate the charges. In the case of direct electrical-based EAPs, the strength of the electrostatic forces is minimal [20], limiting any larger-scale actuation or sensor applications. Conversely, while ionic EAPs offer greater actuation forces, they rely on an ionic bath increasing design complexity. Further, since ionic mechanisms rely on the absorption of ions, the cycle times often perform worse than SMAs and SMP-based materials without additional hardware to hasten the disassociation post actuation through greater electromagnetic fields in the case of electrochemical stimuli or an evaporative mechanism for contact absorption stimuli.

The trade-offs between flexibility and strength, efficiency and speed, and overall complexity exist in each of these materials. Finding a material that can capitalize on each of these would offer a substantial opportunity for improved active materials. This is where CNT's aim to address. Though they are commonly classified as an EAP on their own, their unique mechanical and electrical properties distinctly separate them from other EAP materials and highlight the potential influence they could have on future active materials.

2.3 Carbon Nanotubes as Actuator Components

CNTs are widely considered advanced materials with a variety of unique properties desirable in countless applications. Their high conductivity, low weight, and high tensile strengths allow them to augment all sorts of designs to obtain additional abilities such as improved sensors, stronger materials and smaller actuators. While these characteristics have inspired many to investigate how they could incorporate CNTs into a variety of applications, their fabrication complexity and cost have hindered the predicted uptake since their invention. However, consistent work on new fabrication techniques has decreased the cost and improved the quality and speed of their production [21, 22, 23]. These improvements have pushed the industry to develop commercial products to capitalize on this potential market. This new found availability presents an opportunity to establish a standard baseline for their capabilities within an actuator design with greater precision previously impossible.

CNTs can be incorporated in one of three forms: powders, fibres or yarns. Powder infiltration involves coating a host material with CNTs which provide increased strength and conductivity [24] depending on the extent of the coating. CNTs can also be a pulled into fibres initially and further bundled into yarns, both offering high conductivity and tensile strength due to the homogeneity of the material and high concentration of CNTs. Typically, fibre and yarn formats are more commonly leveraged due to their familiar geometry to the countless other materials used in the established textile industry, easing the technical knowledge required for embedding these materials in various applications.

2.3.1 Carbon Nanotube Fibre and Yarn Material Properties

CNT fibres and yarns inherit many of their impressive properties from the underlying CNT material, demonstrating high tensile strengths of 80 GPa [25] and low resistivity ranging from 7×10^{-8} to $10\,000 \times 10^{-8}$ $\Omega.m$ [26, 27, 28]. Their composite structure allows stresses to be distributed amongst the many individual fibres, which are much stiffer, allowing them to remain highly flexible [29]. Such a geometry also enhances conductivity due to electron hopping between the individual fibres as the current passes down the longitudinal axis of the material. Here, resistance is defined by two dimensions of yarn, the resistance of the longitudinal edge of the fibre bundle and the contact resistance between parallel fibres.

The balance between these two resistances can vary depending on the bundle density. For yarns, bundling is accomplished through twisting individual fibres together. Thus, this density is modulated by tuning the helical angle to increase the radial pressure of the yarn. The helical angle is the angle between the fibre twist and the axial direction, defined in Eq. 2.1 and visualized in Figure. 2.1. Ideally, this angle can be optimized, known as the critical angle, which was found to be 25-50 ℃ [20].

$$\alpha = \arctan \frac{2}{\pi r T} \tag{2.1}$$

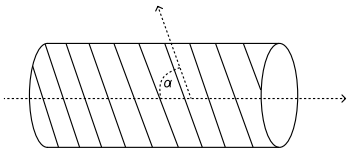

Figure 2.1: Helical angle α along the carbon nanotube yarn

The raw mechanical and electrical capabilities however are poorer than those seen in individual CNTs. Pure CNT have been reported to have tensile strengths of 100 GPa [30], resistivity as low as 1×10^{-8} $\Omega.m$ [31], and a young's modulus of 1 TPa [30, 32]. This diminished mechanical and electrical property translation from the nano to the macro structures remains a challenge, but has been linked to the fabrication quality, and the underlying geometry of the yarn [33, 34].

Yarn fabrication processes involve one of three techniques; direct spinning from a CVD furnace [35, 36], wet-spinning of CNTs [37, 38] or dry spinning from multi-walled carbon nanotube (MWCNT) forests [39, 40]. Depending on the application of the fibres, a technique can be selected to enhance or diminish specific properties from their original CNT precursor material [41].

Yarn quality is most often measured by the consistency of the longitudinal alignment of the underlying CNTs during the spinning procedure and has been a key point of improvement for each of these techniques [33]. This can also be accomplished as a post-treatment process where chemical additives [42], or external mechanical pressures such as cyclical loading [43].

Complimenting CNT alignment, bundling can be used to emphasize different internal forces within the yarn. Twisting the fibres results in greater interaction between the underlying CNT bundles via Van der Waals forces, and the increased lateral friction makes them more resistant to tensile stresses and tensile strains [34, 44, 45]. This relationship is not linear, as seen by the solid lines in Figure. 2.2 and

thus must be tuned to maximize the tensile gains achieved with an increasing helical angle. It should be noted that such changes inversely diminish the young's modulus of the resulting yarn [29]. As twisting increases the density of the CNT bundles, it reduces the internal porous structure of the fibre in a predictable manner [46]. These nanoscale pores are a consequence of imperfect packing of the CNT bundles, which negatively affect the overall strength and conductivity of the material [47]. Furthermore, one can tailor the winding geometries to improve the strength for a particular directional force or impart an embedded chirality within the fibre which can be exploited in eventual actuator designs [48, 49].

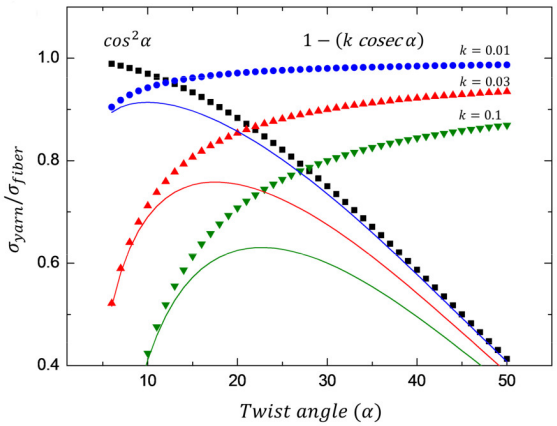

Figure 2.2: Theoretical relationship between the strength of the yarn or fibre and the twist angle α where k is a contribution factor, and σ_{yarn} and σ_{fibre} are the strength of the yarn and elementary fibre respectively. This relationship is derived from the classical yarn mechanics theory [50], where $\cos^2\alpha$ describes the decline in yarn strength and $[1-(k\csc\alpha)]$ describes the strength drop-off due to the increasing transverse forces as a function of twist angle. (Adapted with permission of Elsevier from [51])

Each of these aspects of the CNT yarn can be modulated to create a material tuned for an end application. For example, one could design a CNT yarn that is not very conductive but extremely strong or a material that is extra resistant to fracture from specific application-specific forces. This tunability is still somewhat complicated owing to the small size nature of the precursor material and fabrication difficulty. When reviewing reported CNT yarns, it is no surprise that almost all were fabricated in a lab and limited to the lab testing settings. However, this is beginning to change, with a few commercial offerings becoming available over the last decade. Though these have primarily been for pure CNT powders, some have showcased their CNT yarn and fibre-like materials, albeit mainly restricted to industrial access.

2.3.2 Actuation Mechanisms

The aforementioned properties of CNT yarns can support various actuating mechanisms either directly within the yarn itself or through an intermediary guest material.

When stimulated electrically, CNT yarns experience small electromagnetic forces along their longitudinal axis. While this effect is relatively minimal, it can be amplified by incorporating twisted structure into the yarn [20,49,52]. With this geometry, the coils of each portion of CNT yarn emit electromagnetic forces upon one another, effectively creating small magnetic fields along its longitudinal direction. The combined effect of these small forces along the yarn contributes to a contraction along the longitudinal axis, illustrated in Figure 2.3.

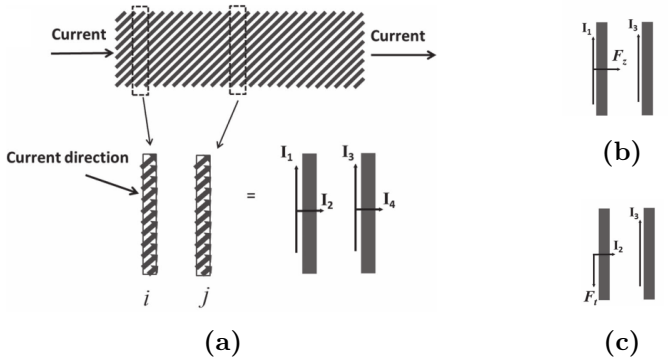

Figure 2.3: Electromagnetic actuation mechanism behind contractive and torsional motions. (a) Schematic of two parallel cross-sectional disks i and j taken in the carbon nanotube yarn. (b), (c) Schematic of the currents and forces experienced by each disk. F_z and F_t represent the contractive and torsional forces respectively. (Adapted with permission of John Wiley & Sons Ltd from [20])

This contractive force can be modelled as:

$$F_z = \frac{\mu I_1 I_3 l}{2\pi r} \tag{2.2}$$

Where l is the effective length of the fibre in the perpendicular direction, μ is the magnetic permeability and r is the radius of the singular CNT fibre.

When leveraged as an intermediary, their high conductance has been shown to be effective in triggering thermoelectric changes in surrounding materials boasting a quick method for supplying heat to a localized area in a controlled manner. Additionally, their minimal coefficient of thermal expansion [53] makes them resistant to

degradation in these applications. Actuators composed of CNT yarns with surrounding sheaths [54, 55] or infiltrated composites [56, 57] have been shown to facilitate the transmission of thermal energy into thermally sensitive materials, generating predictable and controllable actuation.

Due to the porosity of assembled CNT yarns and fibres, sorption and electrochemical mechanisms can play an interesting role for driving actuation behaviours as well. With the introduction of an ionic compound, the absorption of the charged molecules into the porous fibres can drive contraction. When the charged particles enter the fibre's structure, the increase of like charges causes an internal repulsion of the aligned MWNTs or MWNTs bundles [58, 59, 60] as shown in Figure 2.4.

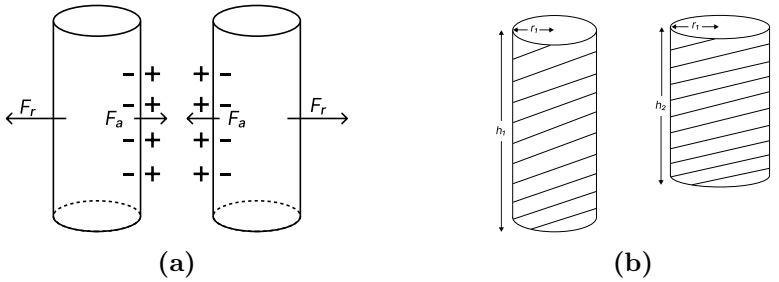

Figure 2.4: Ionic actuation mechanism behind contractive and torsional motions. (a) Schematic of two parallel MWNTs bundles infiltrated by additional ionic charges where F_r are the repulsive forces, and F_a are the attractive forces. $F_r >> F_a$. (b) Schematic of a carbon nanotube yarn after before (left) and after (right) infiltration where $r_2 > r_1$ and $h_1 > h_2$.

This repulsion causes the volumetric expansion and thus an expansion of the coil diameter, reducing the coils stiffness and resulting in the axial contraction. Equation (2.3) highlights the stiffness relationship of a coiled CNT yarn, where stiffness (S) depends on the material's shear modulus (G), the yarn diameter (d), the coil diameter (D), and the number of turns in the coil (N) [61].

$$S = \frac{Gd^4}{8D^3N} \tag{2.3}$$

Taking advantage of this structural change, actuation can be realized by triggering the volumetric expansion of the material [55, 62, 63, 64, 65], resulting in expressed longitudinal changes. Ionic liquids, such as water and ethanol, induce response times and actuation strengths dependent on their polarity and diffusion rate [62, 64].

In practice, these actuators commonly utilize variable submersion of the CNT to control the actuation, though this can be quite complex. Conversely, attempts

at mimicking this process with gels has showed some promise [63]. Generally, ionic activation induces superior contractile strains compared to temperature-dependent or electromagnetic actuation techniques [55], although electrolyte dependency and long cycle times remain an issue.

2.3.3 DexMat Carbon Nanotube Fibres and Yarns

The primary material used in the successive experimentation was the commercial CNT fibre and yarn manufactured by DexMat Technologies. Of all the prospective commercial manufactures on the market such as Timesnano, Nanograffi, and Huntsman Corp., they are the only supplier with a variety of available products at competitive prices. Additionally, when reviewing the properties of the DexMat fibres/yarns compared to other commercially available offerings, the DexMat products reported higher tensile strengths and conductivities most likely owning to their greater CNT lengths, CNT packing densities and Herman orientation factors [66]. DexMat supplies three primary CNT "Galvron" products: fibres that are less than or equal to 100 μm in diameter, braided yarns which are 150 μm and above and ribbons. Some of their yarn products are labelled as carbon nanotube high-strength (CNT-HS) which have the additional benefit of greater tensile strengths. One of the key benefits of investigating with a commercial product is the standardized information available. Table 2.1 presents a summary of the products used within this thesis and their corresponding properties.

Table 2.1: DexMat Carbon Nanotube Product Properties [67, 68, 69]

Property	Diameter (μm)		
	40†	100†	200‡
Actual Diameter (μm)	40 ± 5	100 ± 30	200 ± 20
Linear Mass ($mg \cdot m^{-1}$)	1.7 ± 0.2	13 ± 1	32 ± 3
Density ($g \cdot cm^{-3}$)	1.4 ± 0.1	1.5 ± 0.3	1.0 ± 0.1
Linear Resistance ($\Omega \cdot m^{-1}$)	140 ± 30	17 ± 3	7.0 ± 2
Conductivity ($MS \cdot m^{-1}$)	6 ± 1	8 ± 2	4.0 ± 0.6
Break Force (g)	100 ± 20	1750 ± 150	3000 ± 400
Tensile Strength (MPa)	800 ± 150	2000 ± 400	1000 ± 100
Tenasity ($MN \cdot tex^{-1}$)	600 ± 100	1300 ± 100	1000 ± 100
Cost per metre ($USD)*	80	100	200

† Fibre
‡ Yarn
* Price at the time of writing

2.4 Carbon Nanotube Fibre and Yarn Actuator Design

2.4.1 Design Considerations

With the considerable amount of beneficial properties highlighted in 2.3.1 and the methods of exploiting those properties covered in 2.3.2, the main question dictating the end design are the application parameters. Noting the performance characteristics required by the actuator, the working conditions and any environment limitations would provide a framework for what CNT-based actuator scheme would be best suited. Determining the right combination of geometry and actuation mechanisms is integral to any performant actuator.

When utilized within an actuator design, often, these singular properties require enhancement to be effective on a macro scale. This is often accomplished through complimentary structure geometries, such as overtwisting, bundling or plying illustrated in 2.5, seen in many of the linear actuator designs [49, 56, 70].

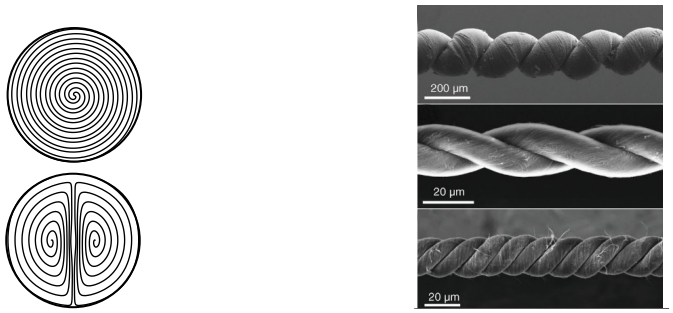

(a) **(b)**

Figure 2.5: Internal and external structures of carbon nanotube yarns. (a) Internal structure of a carbon nanotube yarn, Dual-Archimedean (top) and Fermat (bottom) designs. (b) SEM images of external fibre structures, coiled (top), two-ply (middle), and four-ply (bottom) (Adapted with permission of The American Association for the Advancement of Science from [48]).

When an overtwist is introduced into the fibre, it becomes analogous to a stiff spring, where fundamental spring properties, such as spring indexes and twist angle, are more pronounced and characterized by the standard spring equation. While this can be seen to a lesser extent by the original form of the fibres and yarns, which is somewhat twisted after the spun fabrication process, the overtwisting amplifies these effects by expanding the diameter of the spring material. Without any stimulation,

this geometry already contains far greater potential energy than its standard form. The overtwist can also be optimized for particular mechanical properties such as increased contractile strain and stresses depending on the helical angle introduced [62].

If the desired force is of greater concern, multiplier methods such as composing bundles of fibres in the form of thicker yarns [49, 70] has been effective. In these designs, the forces are distributed among the bundled fibres, improving the contractile performance and mechanical stress resistance. This technique can be used in conjunction with others to improve the overall strength performance at the cost of stroke length. Further, combining various fibres or yarns into more complex geometries seen in 2D or 3D designs can take advantage of a particular scaffold geometry [49, 64], or the differential response between layers [56] for a unique operating behaviour.

More complex actuators can be designed by using additional materials in conjunction with the CNT fibre or yarn to complement the geometric enhancements. Such is the case for composite actuators that use sheathing or guest infiltration interfaces described in Figure 2.6. In a sheathing format, the CNT material is a conduit of thermal energy to a surrounding thermoreactive material which undergoes either contraction or expansion when heated. Similarly, guest infiltration takes advantage of the same interaction, however in this case, the guest materials are allowed to be absorbed into the CNT fibres. In this form, thermoreactivity of the guest material triggers a volumetric expansion within the CNT fibre pores, expanding the fibre radially and consequentially contracting the fibre axially.

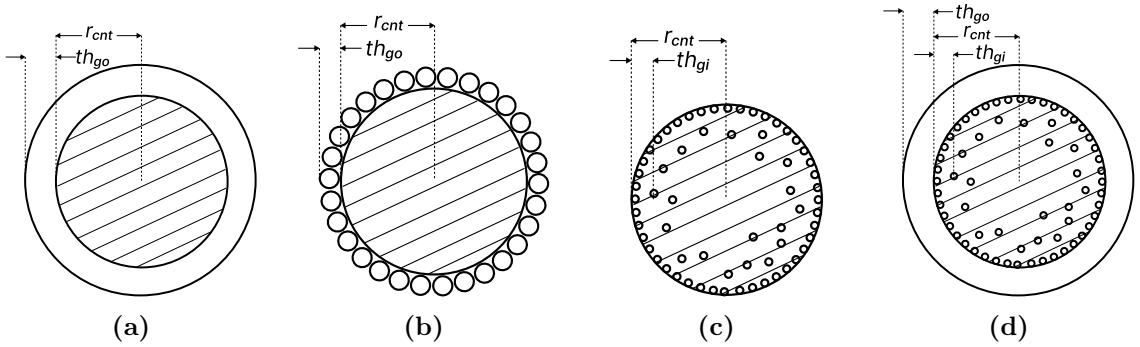

Figure 2.6: Cross-sectional schematic of composite carbon nanotube actuator designs. These are the sheathing methods via (a) coating, and (b) wrapping, (c) the infiltration method and (d) a combination of both infiltration and sheathed coating methods. Here, r_{cnt} is the radius of the CNT fibre or yarn, th_{gi} is the thickness of the infiltrated guest material, th_{go} is the thickness of the outer guest material.

Infiltration can also be used to encase higher tensioned twisted CNT fibres, leveraging the guest materials variable stiffness when thermally stimulated to control

actuation. Such systems operate as a two-spring system, throughout this thesis referred to as the stiffness-variable design, modelled as a balance between the tension of an inner coil and the stiffness of the surrounding guest material. This allows for an enhancement of the default guest infiltration method by providing additional potential energy.

The actuation mechanisms provide further constraints on any actuator design, whether through electrical, thermal, or ionic means. Utilizing thermal activation methods, whether generated via electrical, photonic or otherwise [48], as shown in the sheath [54, 55], guest infiltration [71] and stiffness-variable [56, 72] methods, restrict the actuator to an environment with a stable thermal profile to ensure consistent and controllable behaviour. While this can be tailored for sensor applications to provide active sensing of the environment when the temperature changes, this limitation is important for actuator design. Moreover, designs which use ionic delivery require the complexity of liquid containment which has been shown to be a significant limiting factor for this type of actuator [63,70]. Though this can be overcome as mentioned in 2.3.2 with gel electrolytes for electrochemical interactions, pure sorption mechanisms have no solution.

Designs can also bypass the reliance on external materials all together by simplifying relying on the electromagnetic forces between the coils of the CNT fibre or yarn, making for a more versatile actuator even though the smaller contractile strains limit their utility. Regardless of the driving mechanism, additional considerations need to be given to the power source of these actuators and the control systems required to maintain their operation similar to any traditional actuator.

Lastly, any design must also consider the actuator's eventual applications due to its underlying nanoscale material, especially if intended for the medical field. Though a few studies [73] have found weak and reversible irritation in vivo, they were limited to CNTs in their powdered format. More macro 2D and 3D designs could present unique effects on the corresponding topical areas. Such designs presumably include additional materials surrounding the actuating components, reducing their potential irritant effects. Dedicated studies would be required to investigate their safety adequately and is outside the scope of this thesis.

2.4.2 Existing Single-Dimensional Designs

The desirable properties of CNT yarns and fibres have naturally enticed a plethora of industries to improve biomedical devices [54], sensors [74, 75, 76, 77], and energy storage [78,79]. Still, their fabrication procedures remain costly, pushing the material

out of the commercial application space. To the author's knowledge, there has not been a commercial product developed or in development that utilizes CNT fibre or yarn in an actuator format. Consequently, all the reported advancements in CNT fibre or yarn actuator technologies have remained in the lab setting though these advancements have shown significant performance and relative cost reduction due to improved fabrication methods. Further, while these actuators have been shown to produce both rotational and linear motions depending on their design and support a variety of driving mechanisms as covered in section 2.4.1, this section will focus solely on the electrically driven linear actuators as it best aligns with nature of the thesis.

Reported single-dimensional actuators can be categorized as those which utilize the CNT fibre or yarn as the sole actuator component and those composed of multiple materials, i.e. composite fibres where the CNT fibre or yarn is but one.

In the primary material designs, actuators often follow a twisted-coiled polymer (TCP) design pattern by incorporating some form of overtwist into the fibre or yarn. As mentioned in the section 2.4.1, this overtwist allows for a build of potential energy and, when stimulated, supports a contraction. This has been established countless times [49,62,63] such as with Chen et al. Spring-Like-Fibres (SLF). These actuators were capable of generating contractile strains of 14%, contractile stress of 1.6 MPa, and tensile strength of 220 MPa [49] operated on low voltages ($<$10 V/cm) without noticeable fatigue after 4000 cycles. Additionally, by tuning the helical angle to 32°, peak performance for the contractile stress and tensile stress reached their maximum values [62], further emphasizing the importance of the material geometry.

Utilizing electrochemical drivers for a similarly designed multi-plied yarn developed as seen by Lee et al. and Kim et al. [63, 70] resulted in more significant contractile stresses and strains at the cost of increased cycle times. Further, investigations on electrolyte replacement from aqueous to gel solutions [63, 70] reduce the fabrication complexity making them more appealing for future actuator applications.

Incorporating additional materials in the form of composites can increase the default abilities of these more basic actuator designs. Including elastic materials such as the CNT yarn-spandex composite fibres investigated by Foroughi et al. allowed the team to amplify the contact between the CNT and spandex fibres, increasing the spandex fibres' thermoelastic response when the CNT yarn was electrically stimulated [54]. This composite design generated impressive contractile strains of 33%, far exceeding many of the alternative designs, which average ≈5-15%. Similar results were seen with designs that instead used poly(ethylene terephthalate) (PET) as the complementary fibres instead of Spandex, highlighting how various peak forces and activation times can be modulated depending on the ratio between CNT yarns and

complementary material [80].

Instead of interweaving the non-CNT material into the composite fibre, coating the CNT yarns as seen in sheathed designs, such as those reported by Mu et al., optimize the surface area between the thermal transducer (CNT yarn) and the surrounding guest material. Here, their sheath was maintained by pre-coating the twisted CNT yarn core with a solvent that prevented the infiltration. Three coatings were tested, a poly(ethylene oxide) (PEO), tetrafluoroethylene and sulfonyl fluoride vinyl ether mixture ($PEO - SO_3$), elastomeric polyurethane (PU) or nylon6 [55] resulting in two different coated designed designated by $PEO-SO_3@CNT$, PU@CNT and nylon6@CNT respectively. These samples resulted in maximum contractile strains of ≈13-15% and work capacities of 0.64-1.33 $J \cdot g^{-1}$. Furthermore, the sheath/core ratio to bias angle had been shown to have a direct relationship to the sheath stability, increasing sheath fracture behaviour with an increase in the bias angle.

Allowing the infiltration of the CNT yarn has also been investigated with a variety of guest materials such as paraffin wax [48], $PEO - SO_3$, PU [55, 81], a methanol-elastomer mixture [57], Polystyrene (PS) and poly(styrene-b-isoprene-b-styrene) (SIS) [71]. In each of these cases, the guest material experienced a variable volumetric change when thermally stimulated through the CNT yarn. This resulted in contractile strains ranging from 5-30% and contractile stresses from 16.4 to 85 MPa.

The variable stiffness of a infiltrated guest material can also be leveraged to facilitate actuating behaviour. This is what Xu et al. had achieved with their stiffness-variable design by infiltrating a spring-like CNT yarn core in a higher tension state. The electrical stimulation of their actuator caused the surrounding guest material to undergo a decrease in stiffness, allowing the inner core to temporarily relax until the stimulus was removed. This design managed to produce better mechanical results indicated in Table. 2.3, while utilizing low power and temperature inputs of 40°C compared to alternatives such as the Spandex or Sheath-Run composites, which required operating temperatures of 70°C and 85-100°C, respectively. Though capitalizing on the greater potential energy available, it allowed for standalone actuation without the requirement of external load to equalize the actuator after stimulation [56]. Further, as this design is driven thermally (through the CNT core transducing electrothermal energy), they have also shown the same capabilities through photonic power sources [72].

From the actuator designs reported, the variety of ways CNT fibres and yarns can be utilized and the additional beneficial properties they provide to any actuator design is apparent. In the cases where guest materials are leveraged, their selection

can be integral to tuning the overall activity of the actuator, particularly by selecting the desired range of variable temperature sensitivities. Regardless of design, each of these reported actuators depended on in-lab fabrication methods for the included CNT fibres and yarns, contributing to the overall complexity and cost of the resulting actuator. Shifting to commercial materials that offer better quality could improve the resulting properties in the actuator design and increase their utility for a broader range of applications that have been limited by cost or performance. Determining how these commercial materials compare to in-lab materials within actuator designs, particularly one of the more performant designs, such as the stiffness-variable actuator, would provide the foundational work for future actuators using commercial products.

Table 2.2: Summary of Primary Carbon Nanotube Fibre and Yarn Based Actuators

Name	Actuating Mechanism	Contractile Strain* (%)	Contractile Strain Rate ($\%/s$)	Contractile Stress* (MPa)	Contractile Stress Rate (MPa/s)	Ultimate Strain (%)	Tensile Strength (MPa)	Activation Time (s)	Relaxation Time (s)	Work Capacity (J/g)
Sping-Like-Fibre (SLF) [49]	Electromagnetic	14	140†	1.6	20	245	220	0.100	0.100	0.0116†
Hierarchically arranged Helical Fibre (HHF) [62]	Ionic (Electrochemical)	15	340	1.5	8.4	240	212	0.045	17	0.0267
Single Electrode ($TBA \cdot PF6/PC$) [63]	Ionic (Electrochemical)	16.5	≈16.5†	—	—	—	—	≈1	≈1	≈1.6
Single Electrode ($TEA \cdot BF4/PC$) [63]	Ionic (Electrochemical)	≈10.5	≈21†	—	—	—	—	≈0.5	≈1	≈1.6
Single Electrode ($THA \cdot PF6/PC$) [63]	Ionic (Electrochemical)	≈15	≈5†	—	—	—	—	≈3	≈3	≈1.75
Hierarchically twisted CNT artificial muscle (HTAM) ($THA \cdot PF$) [70]	Ionic (Electrochemical)	15.1	—	—	—	121	94.8	—	—	3.78
Twisted CNT Yarn [20]	Electromagnetic	10	—	—	—	—	—	—	—	—

† Calculated from data provided in current literature.
* Presented stresses and strains are engineering stresses and strains.

Table 2.3: Summary of Composite Carbon Nanotube Fibre and Yarn Based Actuators

Name	Type	Actuating Mechanism	Contractile Strain* (%)	Contractile Strain Rate (%/s)	Ultimate Strain (%)	Tensile Strength (MPa)	Activation Time (s)	Relaxation Time (s)	Work Capacity (J/g)
Hybrid Carbon Nanotube Yarn Muscles (HCNYM) [48]	Sheathed	Electrothermal	3	≈60†	—	—	0.025	0.025	—
Knitted CNT/SPX_1 [54]	Sheathed (reverse)	Electrothermal	16	≈6.4†	895	78	≈2.5	≈2.5	0.640
Knitted CNT/SPX_4 [54]	Sheathed (reverse)	Electrothermal	25	≈10†	880	84	≈2.5	≈2.5	—
Knitted CNT/SPX_8 [54]	Sheathed (reverse)	Electrothermal	33	≈13.2†	600	75	≈2.5	≈2.5	—
Knitted CNT/SPX_{12} [54]	Sheathed (reverse)	Electrothermal	24	≈9.6†	700	82	≈2.5	≈2.5	—
Sheath Run Artificial Muscle (SRAM) $PEO - SO_3@CNT$ [55]	Sheathed	Electrothermal	≈8	≈2†	—	—	≈4	≈1.5	0.64
Sheath Run Artificial Muscle (SRAM) $PU@CNT$ [55]	Sheathed	Electrothermal	≈12.5	≈2.3†	—	—	≈5.5	≈6	1.33
Sheath Run Artificial Muscle (SRAM) $CNT@nylon$ [55]	Sheathed	Ionic (Sorption)	≈15	—	—	—	—	—	0.99
CNT hybrid yarn artificial muscles (HYAM) $PEO - SO_3@CNT$ [55]	Infiltrated	Electrothermal	≈5.5	≈1.38†	—	—	≈4	≈1.5	≈0.4
CNT hybrid yarn artificial muscles (HYAM) $PU@CNT$ [55]	Infiltrated	Electrothermal	≈9	≈1.63†	—	—	≈5.5	≈6	0.11
CNT hybrid yarn artificial muscles (HYAM) $CNT@nylon$ [55]	Infiltrated	Ionic (Sorption)	≈11.5	—	—	—	—	—	0.11
Stiffness-variable Carbon Nanotube Spring-like Nanocomposite Yarn [56]	Variable Stiffness & Infiltrated	Electrothermal	≈12	≈4†	—	—	3	2	—
Hybrid Carbon Nanotube-Polypyrrole-Coated Yarn $CNT - PET$ [65]	Sheathed	Ionic (Electrochemical)	0.08	≈0.0005†	—	—	≈157	≈34	—
Hybrid Carbon Nanotube-Polypyrrole-Coated Yarn $CNT - PET/PPy$ [65]	Sheathed	Ionic (Electrochemical)	0.22	≈0.022†	—	—	≈10	≈20	—
	—	—	—	—	—	—			

† Calculated from data provided in current literature.
* Presented stresses and strains are engineering stresses and strains.

Chapter 3

Experimental Setup

In the following chapter, the experimental setup used to fabricate and test the produced actuators is outlined. First, Section 3.1 describes the investigated stiffness-variable actuator design to highlight the various components and interactions that support its actuating behaviour. Next, Section 3.2 presents the fabrication apparatus responsible for the controlled tuning of the precursor CNT fibre sample throughout each step of the fabrication procedure, such as coiling, stretching and curing, followed by accompanying validation samples and test results. Finally, Section 3.3 concludes the chapter by describing the testing procedures and equipment used to characterize the mechanical and electrical properties as well as the electrothermal and electromechanical responses of the fabricated actuators.

3.1 Stiffness-Variable Actuator Design

The stiffness-variable actuator design, shown in Figure 3.1, leverages the variable stiffness of the infiltrated and sheathed guest material surrounding a high tension twisted-coiled CNT fibre core to perform actuation. As described briefly in Chapter 2, this stiffness variability is driven thermally, either through external sources or electrothermally, using the CNT as the conductive medium. In this thesis, the latter method was selected to characterize this design's strengths and weaknesses adequately. Additionally, while the primary actuation driver is the regulation of the CNT fibre's tension through thermal stimulation, using the electrothermal driving mechanism allows the twisted-coiled core to undergo electromagnetic attraction between its coils, further adding to its actuating behaviour. The two materials selected for this evaluation were chosen due to their commercial availability, the key focal point of this thesis, and contrasting opportunities to previously reported designs from Xu et al. [56, 72].

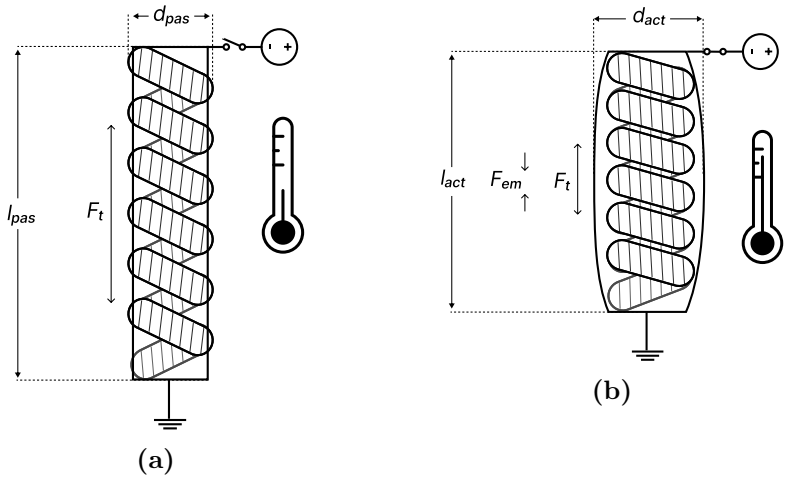

Figure 3.1: Stiffness-Variable actuator design in its (a) inactive and (b) active states where F_t is the tension force, F_{em} is the electromagnetic force, d_{act} and d_{pas} are the diameters and l_{act} and l_{pas} are the lengths. Note, $d_{act} > d_{pas}$ and $l_{act} < l_{pas}$.

For the core, the DexMat Galvron™ CNT fibres were chosen, while the PRO-SET® 125 epoxy resin and PRO-SET® 229 epoxy hardener were opted for as a guest material due to their availability and low cost. The selection of epoxy in particular also allowed for a better comparison to the previously reported stiffness-variable actuator in the literature. An in-depth characterization of their individual properties and how those properties vary with temperature and various fabrication modifications is described in Chapter 4.

3.2 Fabrication Apparatus

3.2.1 Design

To controllably fabricate stiffness-variable actuators, a programmable fabrication apparatus was designed and built. This apparatus was composed of a servo motor, a sled system to ensure constant axial tension, an LCD screen to display the relevant data when performing the fabrication, a control panel and an Arduino to control each component programmatically. The apparatus's design underwent various iterations to best handle the CNT fibres investigated, the first of which is shown in Figure 3.2

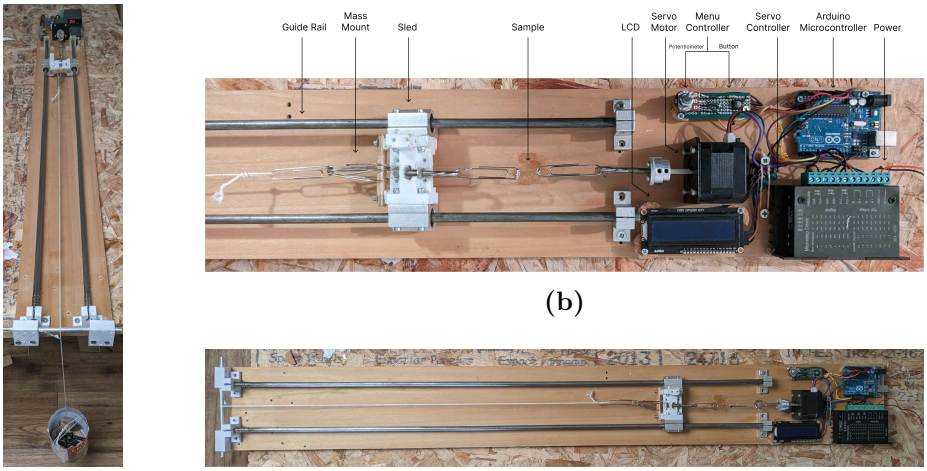

(a) **(b)** **(c)**

Figure 3.2: Initial version of the fabrication apparatus in (a) loaded, (b) annotated and (c) ariel views.

The material mounting mechanism connected the sample of interest to the apparatus and held it securely during actuator fabrication. Various fibre mounting connectors were tested to reduce the setup time for each sample, particularly sandwiching the fibre between two washers, tying the fibres on washers, and soldering the fibres onto paperclips. In the first scenario, the washer sandwich did not provide enough friction to keep the material in place during twisting, often slipping out as the fibre increased in tension. In an attempt to increase the friction between the washers, rubber, plastic, and wood were added, but none substantially improved the results. The second design bound the fibre to the washer by tying it, which fared better during testing. Unfortunately, due to the stiffness of CNT fibres, the knotting procedure led to fracturing when introduced to greater tensions. The final design involved wrapping the fibre around the loop of a paperclip and soldering it into place

prior to placing it on the twisting apparatus. This ensured the fibre could not slip during the twisting procedure and provided the end state required for further testing its electrical abilities.

When testing the mounting setup, it became apparent that there were inconsistencies in the rails guiding the sled. This was primarily due to the slight warping of the rails and the uneven pressure on the bearings supporting the sled. Even with the realignment of the mounting points, any slight shift in the tension would result in the sled getting stuck, allowing the tension in the fibre to build up and either fracture the sample or cause jumps in its movement, completely bypassing the benefits of a contact load during the twisting procedure. Further iterations of this design removed the sled apparatus entirely and used a guiding bar to ensure the sled mounting point did not rotate with the sample when undergoing twisting. Additionally, a curing platform was used to fix the tension applied to each sample during the curing period, shown in Figure 3.3. This final design was used to fabricate all tested samples to characterize the twisted-coiled precursor and stiffness-variable actuators.

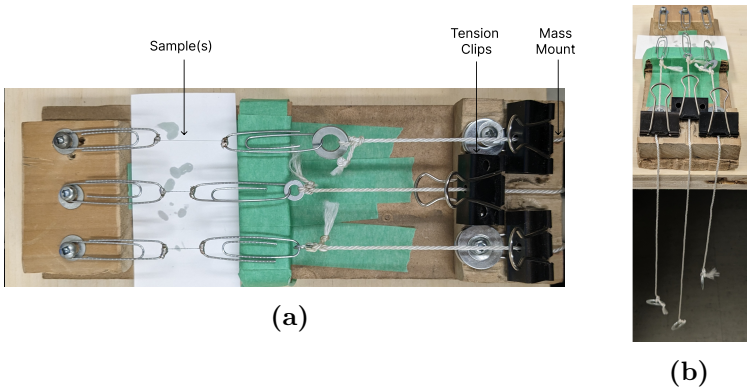

(a) **(b)**

Figure 3.3: Curing apparatus in (a) annotated, and (b) front views.

Finally, the software was designed to provide an intuitive user experience for the apparatus user. Screens were separated into clear menus for the twisting configuration, such as setting the number of twists per cycle, the number of cycles per session, the speed of each twisting cycle and real-time statistics of how many cycles have occurred. The corresponding code and screenshots can be found in Appendix A.

While these modifications improved the twisting procedure required for the actuator fabrication, the entire process remained lengthy due to the time required to cure the epoxy coating.

3.2.2 Procedure

The apparatus facilitated three processes; twisting the CNT fibre, stretching the twisted-coiled fibre, and coating the loaded twisted-coiled fibre.

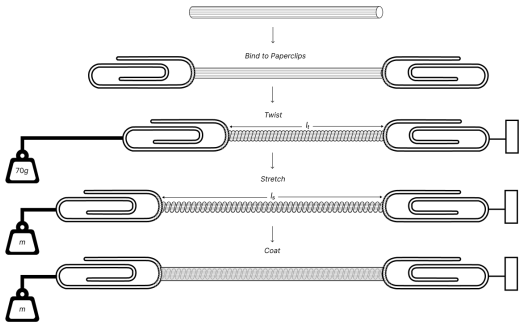

Figure 3.4: Overview of the stiffness-variable actuator fabrication procedure. From top to bottom, the precursor fibre, the pre-twisting stage, the twisting state, the stretching stage and the coating stage. Here, m is the mass used to stretch the twisted-coiled fibre. l_t is the twisted-coiled fibre length and l_s is the length of the twisted-coiled fibre after stretching. $l_s > l_t$.

(a) **(b)** **(c)** **(d)** **(e)**

Figure 3.5: Sample in each stage of the fabrication process. (a) The precursor fibre , (b), the sample pre-twisted before (left) and after (right) the soldering process, (c) twisted-coiled, (d) stretched, and (e) coated.

Table 3.1: Fabrication Procedure Base Properties

Property	Value
Pre-stretch	15%
Twisting Load	70 g
Sample Length	≈2-3 cm
Sample Diameter	100±30 μm [68]
Total Twists	≈90-100
# of Coating Applications	4
Time Before Initial Coat	10 min
Time Between Coats (Coating Interval)	10 min
Total Curing Time	24 hr
Curing Temperature	25 °C

3.2.2.1 Pre-Twisting Setup

The pre-twisting procedure involved three steps. First was binding the CNT fibre to a paperclip by first bending the paperclip into an elongated fashion, wrapping the CNT fibre around the bent portion and surrounding this wrap point with thin gauge copper wire, as illustrated in Figure 3.5(b). This copper wire kept the CNT fibre in place and provided the solder with additional contact points since the CNT fibre was resistant to bonding alone. Then the copper/fibre wrapping was slid into position, the paperclip was re-bent to its original shape, and the wrapping was soldered. This procedure was performed on both ends of the CNT fibre sample.

3.2.2.2 Twisting and Coiling

After the sample had undergone the pre-twisting procedure, it was connected to the apparatus's mount points and placed under tension with a 70 g free-hanging mass. Next, the twisting function was initiated via the graphical interface visible on the LCD, which began twisting the sample. The winding function was limited to a speed of 100 RPM and ten twists per cycle to mitigate the potential fracturing of the fibre during the winding process. The sample would undergo multiple cycles until the entirety of the sample was visibly coiled.

3.2.2.3 Stretching

Applying a particular amount of pre-stretch to the twisted-coiled sample began by first moving it to the loading configuration of the apparatus, and its starting length was measured under the 70 g load using a ruler and image processing software. Then, after a certain percentage of stretch was determined, additional mass was added to the load until the required calculated length and the actual length were within 1% tolerance. A scale measured the mass before loading and after achieving the predefined stretch.

3.2.2.4 Coating

The application of the epoxy coating occurred after the completion of the previous two steps. Here, a 3-1 ratio of PRO-SET® 125 epoxy resin was added to PRO-SET® 229 epoxy hardener in a container and mixed vigorously for 15 s. After mixing, the

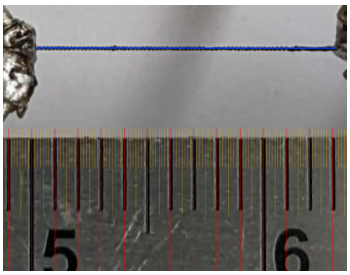

Figure 3.6: Example length measurement with a digital ruler highlighted in red/yellow and the sample highlighted in blue. Images were scaled to match the digital ruler which had a precision of 0.1 ± 0.05 mm.

epoxy rested for ten minutes to increase its viscosity since it tended to bead significantly on the CNT fibre if applied immediately. Then, using a Quetip™ drops of the epoxy mixture were applied to the high-tension twisted-coiled fibre in a brushing manner. The number of applications and length between applications depended on the characteristic tuning further explored in chapter 5, however, unless stated otherwise, the base procedure involved four applications at ten minutes intervals. After completing the application steps, the sample dried for $24h$ at room temperature.

3.2.3 Apparatus Validation

Validation of the fabrication process and the facilitating apparatus involved a series of small tests on each fabrication step.

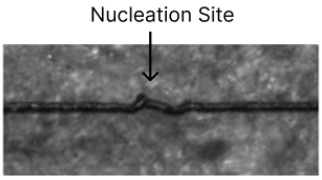

Figure 3.7: Coil nucleation site along the carbon nanotube fibre due to twisting.

The first was the twisting procedure. One of the key aspects of fibre coiling is the coil activation point, where the introduced twists cause coils to nucleate along their axis, as shown in Figure 3.7. Ideally, the coil activation point is modelled by (3.1) [4], assuming consistent fibre diameter, where T_c is the number of twists per centimetre until coiling, ϕ is the twisting load stress, E is the material's young modulus, D is the material's diameter, and G is the materials shear modulus. However, due to missing data on the shear modulus, the determination of the range of values expected is limited. Instead, this test focused on the consistency of results as opposed to ideal

accuracy using five 100 μm samples fabricated under the standard twisting conditions to determine at which point this activation occurred. The overall grouping seen in Table 3.2 shows consistent results with a mean of 20.24 [$\sigma = 0.69$] twists per centimetre. In Table 3.2, T_{tot} is the total number of twists per centimetre.

$$T_c = \frac{8\sqrt{2\phi E}}{\pi DG} \cdot \frac{1}{100} \tag{3.1}$$

Table 3.2: Coil Activation Validation Summary of 100 μm Manufactured Stiffness-Variable Actuator Samples

Sample	Initial Length (cm)	Final Length (cm)	T_{tot}	T_c
s_1	2.53	0.87	36.11	19.36
s_2	2.63	0.77	39.62	20.19
s_3	2.89	0.90	36.45	19.96
s_4	1.86	0.57	41.89	20.41
s_5	2.45	0.97	39.25	21.26

Validating the stretching procedure was difficult due to the fabrication apparatus's limited precision capabilities and the samples' size. To improve this process, image processing of the values using a ruler reference and a more precise digital representation did allow for more accurate reading at such small scales. Further, as each sample varied in length and diameter due to its manufacturer's tolerance, selecting the specific load required to achieve an exact stretch percentage would naturally include some error. Five samples were fabricated with a fixed ideal stretch percentage of 20% shown in Table 3.3 to determine if the apparatus could achieve consistent pre-stretch results. Among the selection of test samples, the variation from the intended stretch value varied by ≈0.9%.

Table 3.3: 20% Pre-Stretch Validation Summary of 100 μm Manufactured Stiffness-Variable Actuator Samples

Sample	Length (cm)			Pre-stretch (%)	
	Initial	Twisted-Coiled	Stretched	Actual	Δ
s_1	2.45	0.97	1.15	18.92	1.08
s_2	2.46	0.89	1.05	18.95	1.56
s_3	2.43	1.13	1.35	19.64	0.36
s_4	2.70	0.94	1.53	19.98	0.02
s_5	2.35	0.70	0.83	18.50	1.50

Finally, three samples with 20% pre-stretch were created using the outlined procedure to ensure that each of these steps produced consistent actuators when utilizing a constant set of fabrication parameters. Their fabrication properties are summarized in Table 3.4, where the Coil Mean Diameter (MD) is defined by (3.2), and

the Spring Index (SI) is defined by (3.3). The resulting samples successfully generated consistent stresses shown in Figure 3.8 and strains shown in Figure 3.9 under the same voltage stimuli. Additional data tables can be found in A.4. Each stress reported is the mean of three trials at each voltage step.

$$MD = OuterCoilDiameter - WireDiameter \tag{3.2}$$

$$SI = \frac{MD}{WireDiameter} \tag{3.3}$$

Table 3.4: Fabrication Properties of 100 μm Carbon Nanotube Manufactured Stiffness-Variable Actuator Samples with 20% Pre-stretch

Sample	Length (cm)		Pre-stretch (%)	MD (μm)	SI	T_{tot}	T_c	$\Omega \cdot cm^{-1}$
	Initial	Final						
s_1	2.45	1.15	18.92	97.00	0.97	39.25	21.26	0.3260
s_2	2.46	1.06	18.95	92.00	0.92	40.22	20.31	0.3389
s_3	2.43	1.35	19.64	69.44	0.69	41.20	21.43	0.3195

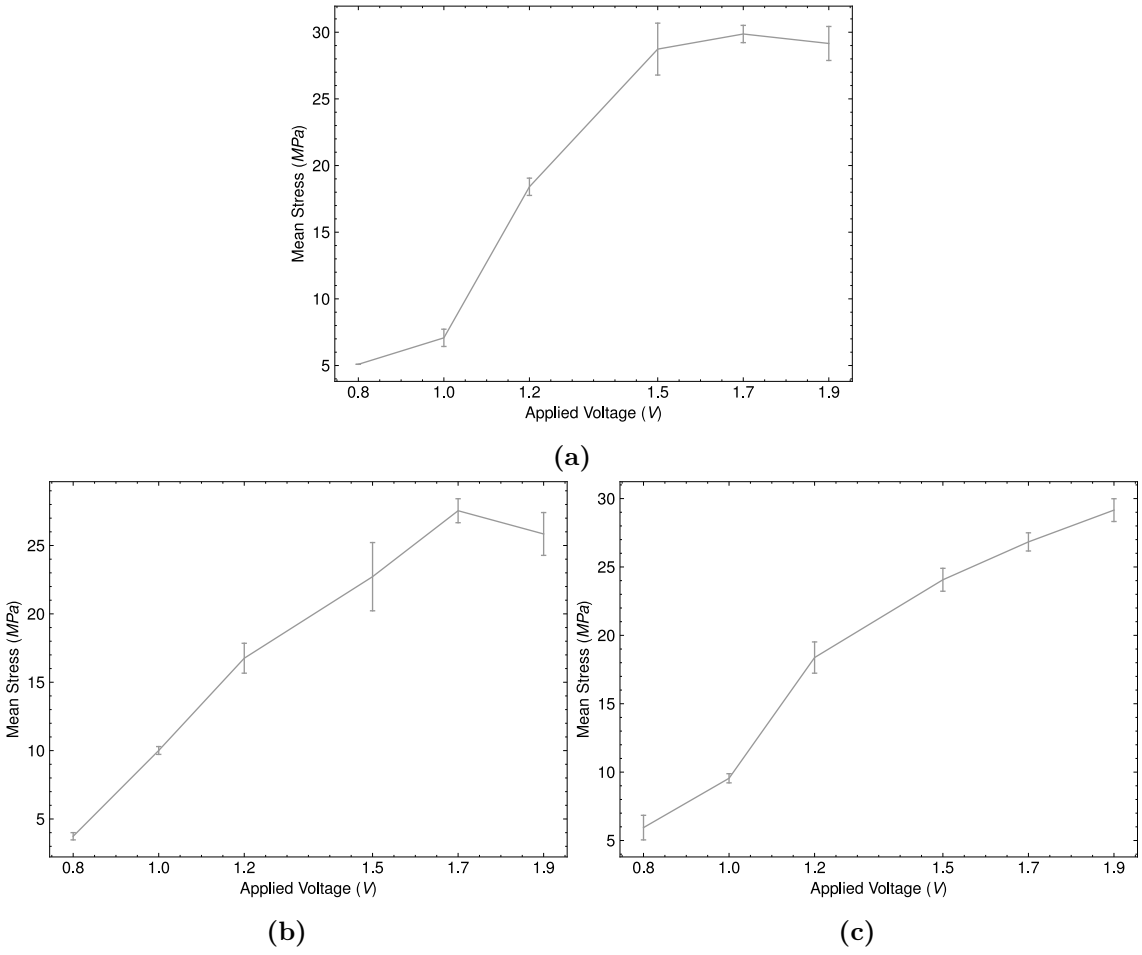

Figure 3.8: Mean contractile engineering stress vs applied voltage for fabricated stiffness-variable actuator validation samples (a) s_1, (b) s_2 and (c) s_3 over three actuation cycles at each voltage.

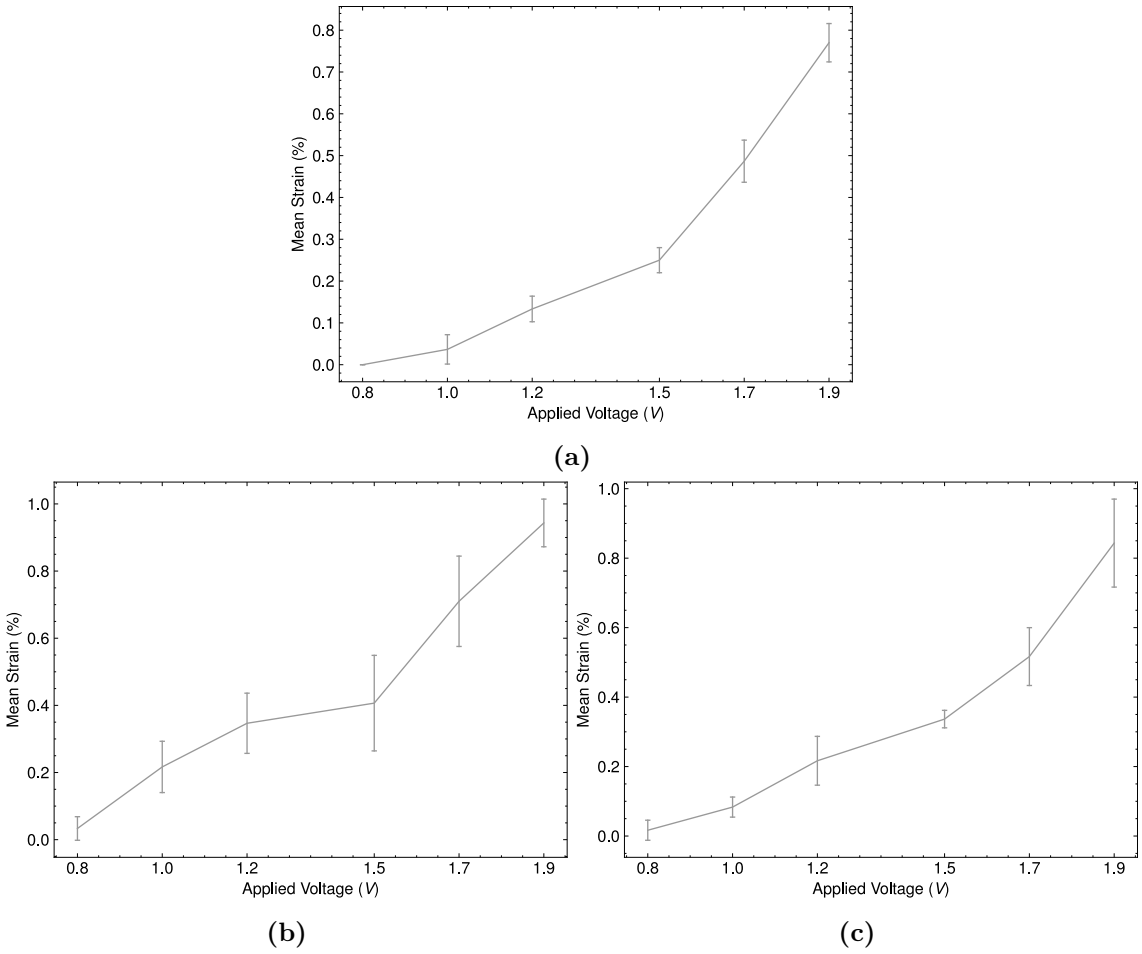

Figure 3.9: Mean contractile engineering strain vs applied voltage for fabricated stiffness-variable actuator validation samples (a) s_1, (b) s_2 and (c) s_3 over three actuation cycles at each voltage using a 4 g hanging load.

3.3 Experimental Equipment and Procedures

3.3.1 Test Selection

The selection of tests aimed to measure the six characteristics, namely the tensile strength and breakage strain, resistance, stimulated surface temperature and contractile stress and strain, critical in assessing the utility of these electrothermal actuators. These characteristics are highly connected. While they are passive, the tensile properties, particularly the material's stiffness, sets the internal mechanical

resistances that the electromechanical responses have to counteract during actuation. Similarly, the electrical resistances regulate the thermal responses of the CNT as a conductor, thus affecting the variable stiffness of the surrounding epoxy and, consequently, the resulting electromechanical response.

The particular procedures used to measure each of these properties are outlined in the following subsections.

3.3.2 Mechanical Properties

The DexMat Galvorn™ CNT fibres used by the stiffness-variable actuators had their mechanical properties characterized by a series of tensile tests to failure performed using the Instron 4202 Universal Tensile Machine™ , which supports force precisions of 0.1 N and variable strain rates. For these tests, a load cell of 500 N was selected and set to a 10% range (50 N) to more accurately capture the 500-3000 MPa range of stresses expected with these materials as outlined by the manufacturer's specification. The tests were conducted at a strain rate of 1 $mm \cdot s^{-1}$ and marked as completed once the sample's tensile strength reached 30% of its peak value.

3.3.3 Electrical Properties

CNT fibres are known to have very low resistances owing to their precursor CNTs, whose resistances are on par with common metals such as copper. These low values necessitated a method that could eliminate the influence of the testing equipment on the measured resistances, whose own resistances would be within a similar magnitude. As such, a four-point resistance measurement was performed using a Keithley 2010™ multimeter. This multimeter supported 1 $u\Omega$ precision [82] and many filtering functions for noisy signals. No filtering functions were applied within these measurements due to the relatively stable signals.

For each tested sample, resistances were taken between each fabrication stage. This involved connecting the probes to either end of the sample using a four-point setup and recording the displayed value after ten seconds to allow the signal to settle. In the cases where higher precision pre-stretches were of concern, such as investigating the twisted-coiled precursor samples, they were instead mounted within a tensile device known as the Biotester 5000™ developed by CellScale which operated using a 23 N load cell and supported force and displacement precisions up to 1 mN and 1 μm, respectively [83]. This device applied a calculated displacement

to achieve the desired sample pre-stretch, at which point the standard resistance measurement occurred as illustrated in Figure 3.10. Recalibration of the Biotester occurred between each sample to minimize any displacement alterations that may have occurred during the mounting/unmounting process.

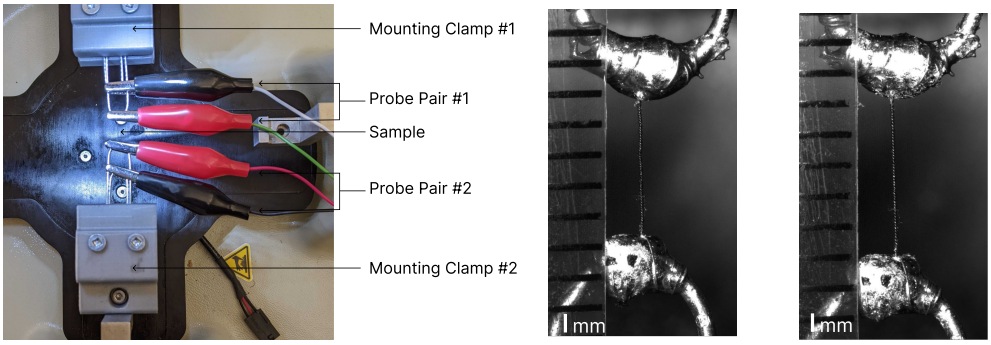

(a) **(b)** **(c)**

Figure 3.10: Twisted-Coiled actuator sample mounted in the (a) Biotester and with (b) 0% and (c) 15% pre-stretch next to the reference ruler.

3.3.4 Electrothermal Response

The stiffness-variable actuator design relies on the joule heating of the sheathing guest material to variably change its stiffness. In this design, the CNTs acts as the medium to transfer the thermal energy necessitating an adequate understanding of their thermal conductivity properties to tune this stiffness accurately. To measure these thermal changes, a FLIR E6-XT™ infrared camera was employed that supported 9 Hz image frequency, $\pm$ 2℃ temperature accuracy and a -20 to 550 ℃ temperature range [84]. Voltage stimulation was provided via a KAIWEETS PS-3010F™ power source which supported up to 30 V, and 10 A with 0.01 V and 0.01 A resolutions [85].

Testing the thermal responses began by first mounting the sample in the Biotester and then connecting the sample to the power supply with an intermediary control switch for manual control. The Biotester was used to ensure consistent tension in the sample, so it remained horizontal and to module the pre-stretch in twisted-coiled samples, similar to the procedure outlined in Section 3.3.3. When initializing a test, a timer was started that provided an indicator to track three-second cycles to direct the manual triggering of the power switch. During each stimulation cycle, the thermal camera was manually handled and pointed toward the sample in the setup to record the max temperature observed. Each test included three cycles with a five-second rest period in between each to ensure consistency of the temperature results for applied

voltages of 0.8, 1.0, 1.2, 1.5, 1.7, and 1.9 V. This range was selected after an initial investigation into the durability of the epoxy during actuation. It was observed that the applied voltages greater than 2.2-2.3 V led to a bubbling, excessive globing and burning of the epoxy, depicted in Figure 3.11, during actuation. As such, keeping below this threshold would ensure minimal damage to the sample during testing while providing insight into the effects due to increasing voltage stimuli.

Figure 3.11: Damaged sample after exposure to a 2.5 V for 5 s, resulting in epoxy discolouration and reduction along the centre portion of the sample. Globs at the ends are exaggerated due to the resetting of the epoxy at the increased liquid state.

3.3.5 Electromechanical Response

Understanding the connection between the electrical stimulus and the corresponding mechanical response is vital to the stiffness-variable actuator design. To determine the extent of this relationship, two tests were created that utilized a multi-voltage electrical stimulus on CNT samples in each stage of the fabrication process.

The first test measured the stress produced under isometric conditions. Tested samples were placed into the Biotester's mount points while connected to the power leads from the Kaiweets power supply. When connected, a test campaign was initiated on the Biotester that involved five stimulation-relax cycles of three and five seconds, respectively, where the Biotester measured the generated force and cycle lengths of each actuation. Each cycle set was repeated for 0.8, 1.0, 1.2, 1.5, 1.7, and 1.9 V at a 100 Hz sampling rate to ensure higher time precision during actuation. The peak results were averaged over each actuation cycle's top three maximum values.

The second series of tests measured the strain produced under isotonic conditions when stimulated. A testing apparatus, shown in Figure 3.12, was built to hold the sample and provide an electrical connection while supporting a load. After mounting, the sample was tested under a four gram load condition over three cycles at 0.8, 1.0, 1.2, 1.5, 1.7, and 1.9 V. The captured test recording was parsed into images of the sample at the beginning and end of its actuation cycle and analyzed using the Biotester's image analysis suite, LabJoy™.

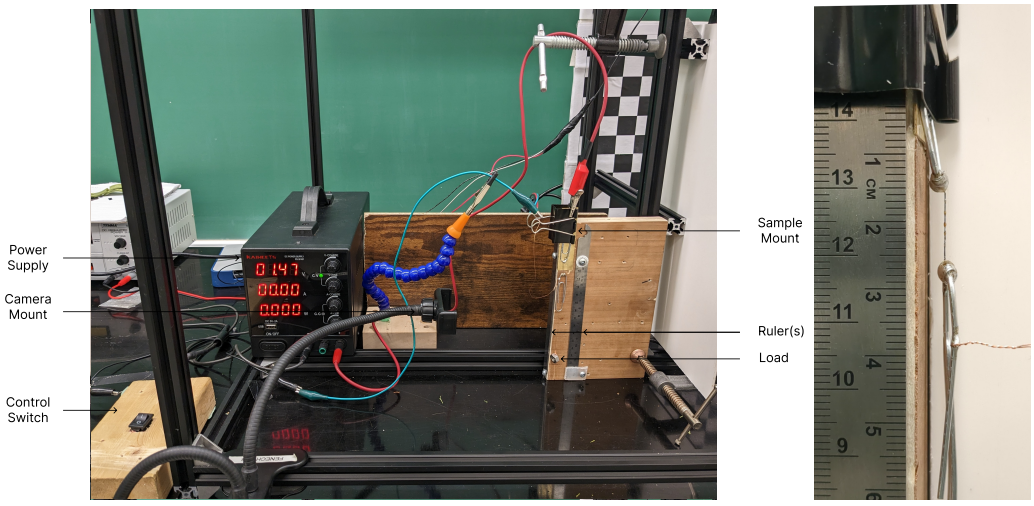

Figure 3.12: Strain testing apparatus (a) annotated and (b) camera views.

Chapter 4

Experimental Evaluation of Actuator Components

To fully understand the capabilities of any actuator design, it is necessary first to characterize its underlying components integrally responsible for its emerging performance. This chapter presents a comprehensive experimental evaluation of the commercial stiffness-variable actuator components, the DexMat 100 μm Galvorn CNT-HS™ fibre and the PRO-SET® 125 epoxy resin and PRO-SET® 229 epoxy hardener. Presented first are the mechanical, electrical, electrothermal and electromechanical characterizations of the commercial CNT fibre in its uncoiled, twisted-coiled, stretched and coated formats. This is followed by the mechanical properties, and electrical response of the PRO-SET® epoxy is detailed, providing additional information on how these components will work together.

4.1 DetMat Galvorn CNT-HS™ 100 μm Fibre Properties

4.1.1 Mechanical Properties

Uniaxial tensile tests were used to verify the commercial break strength data reported by the manufacturer's specifications to ensure consistency within the commercial samples and, to highlight the effect of each fabrication step on these properties. Three 100 μm diameter CNT fibre samples were selected at uncoiled, twisted-coiled, and coated fabrication stages to undergo the loading campaign described in Section 3.3.2, shown in Figure 4.1.

While the reported manufacturer tolerances are quite large, as seen in Table 3.1, the results obtained from the tensile tests were well within the specifications. For the 100 μm diameter pre-twisted fibres, this resulted in a mean maximum strength of 1993.72 [$\sigma = 92.23$] *MPa*. Furthermore, the ultimate strain and corresponding necking strain, that being the strain between the tensile strength and the ultimate strain, remained at 7.15 [$\sigma = 1.05$]% and 0.11 [$\sigma = 0.06$]%, respectively, emphasizing the relatively high stiffness of the material, at 32.02 [$\sigma = 7.81$] $GPa \cdot m^{-1}$, and highly localized deformation. The stiffness was also slightly non-linear, particularly outside the 1-3% strain range, with plastic behaviour beginning at 3.5% strain.

As the fibre goes from uncoiled to twisted-coiled, a trend appears in the resulting sample's tensile strength and overall flexibility. Twisted fibres show a diminished ability to withstand loads by a factor of ≈2.75, ($t(4) = -20.5901; p = 3.3 \times 10^{-5}$), as seen when comparing the maximum strengths reported in Tables 4.1 and 4.2, with a mean of 721.50 [$\sigma = 54.29$] *MPa*. This reduction is due to microfractures appearing during the twisting procedure [45]. Although DexMat uses longer CNTs in their fibre and yarn fabrication [66], the locations conglomeration act as fracture points and would experience higher stresses as the fibre underwent torsional stresses. In contrast, the introduction of coiling increased the ultimate strain ≈7.48 times, ($t(4) = 13.8969; p = 1.5 \times 10^{-4}$), with a mean of 53.45 [$\sigma = 5.64$]%. Similarly, the necking strains increased partially compared to their pre-twisted counterparts, though inconsistently, showcasing how the fibre damage brought on by twisting reduces the localization of deformation during loading. These samples' stiffness were significantly smaller, ($t(4) = -6.8752; p = 2.3 \times 10^{-3}$), as well, at 1.06 [$\sigma = 0.10$] $GPa \cdot m^{-1}$, owing to their coiling structure, and showed a more exponential behaviour with an increasing load.

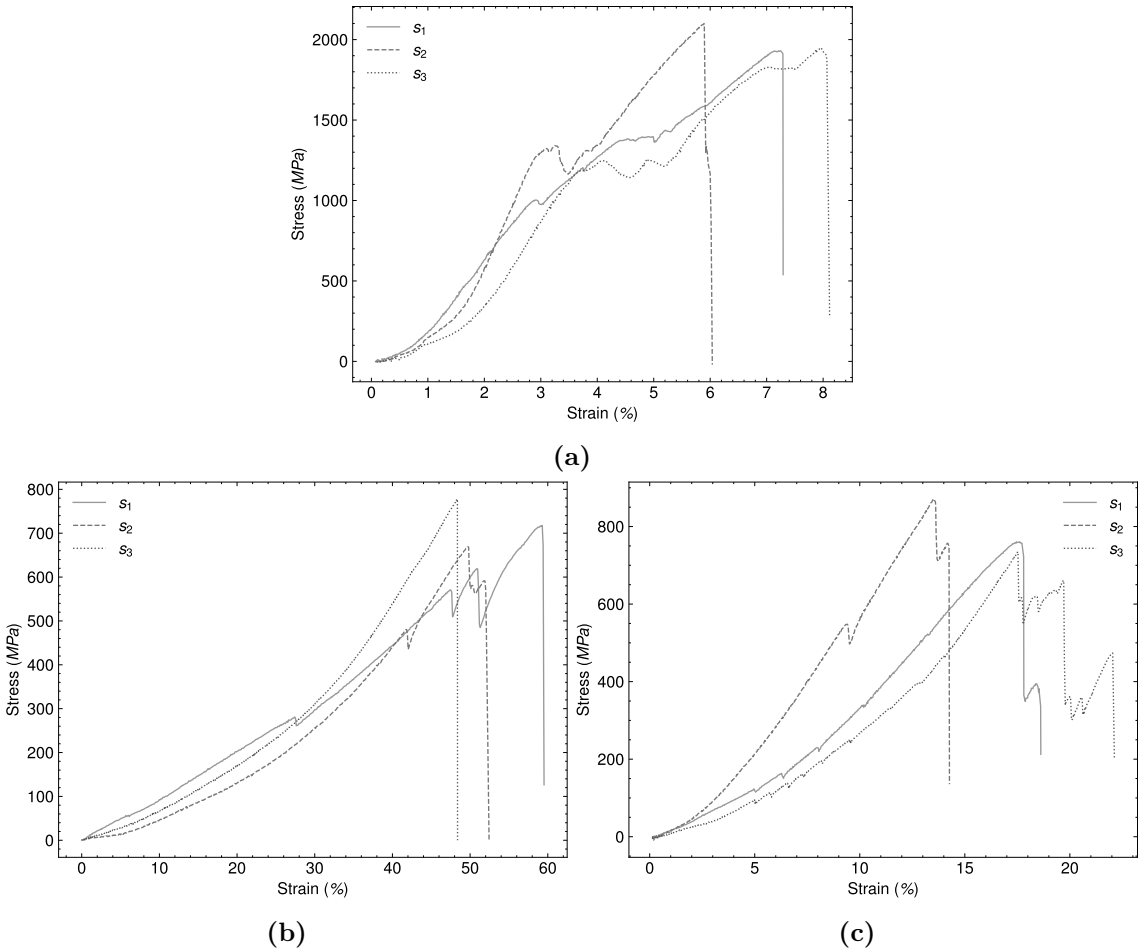

Figure 4.1: Monotonic to failure uniaxial tensile test of (a) pre-twisted, (b) twisted-coiled and (c) coated with 15% pre-stretch 100 μm carbon nanotube sample sets composed of three fibre samples, s_1, s_2 and s_3.

The failure behaviour also changed with the introduction of the epoxy coating. Compared to the twisted-coiled samples, the coated samples experienced an extended failure over a greater strain. This intuitively makes sense when one considers the bonding attribute of the epoxy itself. When the epoxy soaks into the fibre, even the upper layers, it adds additional reinforcement to the underlying fibres. Though this did not result in a discernible improvement in the tensile strength, ($t(4) = 1.2984; p = 2.6 \times 10^{-1}$), with a mean of strength of 789.15 [$\sigma = 72.10$] MPa, the effect on the ultimate strain is apparent ($t(4) = -8.8162; p = 9.1 \times 10^{-4}$), even when accounting for the embedded 15% pre-stretch. This is demonstrated in Figure 4.1(c) and Table 4.3, where the ultimate strain was 18.34 [$\sigma = 3.29$]%. Similarly, the stiffness increased significantly, ($t(4) = 3.1335; p = 3.5 \times 10^{-2}$), compared to the twisted-coiled samples with a measured value of 3.86 [$\sigma = 1.55$] $GPa \cdot m^{-1}$, and was

visibly more linear.

Table 4.1: Monotonic to Failure Uniaxial Tensile Test Summary of 100 μm Pre-twisted Samples

Sample	Tensile Strength (MPa)	Ultimate Strain ($\%$)	Necking Strain ($\%$)	Young's Modulus[§] ($GPa \cdot m^{-1}$)	Toughness ($MJ \cdot m^{-3}$)
s_1	1931.63	7.29	0.04	34.25	76.01
s_2	2099.70	6.04	0.15	38.56	60.70
s_3	1949.84	8.12	0.15	23.40	82.04

[§] Calculated at 2.5% strain.

Table 4.2: Monotonic to Failure Uniaxial Tensile Test of 100 μm Twisted-Coiled Samples

Sample	Tensile Strength (MPa)	Ultimate Strain ($\%$)	Necking Strain ($\%$)	Young's Modulus[§] ($GPa \cdot m^{-1}$)	Toughness ($MJ \cdot m^{-3}$)
s_1	717.47	59.62	0.23	1.05	192.61
s_2	669.34	52.54	2.72	0.96	131.02
s_3	777.69	48.38	0.02	1.17	134.70

[§] Calculated at 35% strain.

Table 4.3: Monotonic to Failure Uniaxial Tensile Test Summary of 100 μm Coated Samples

Sample	Tensile Strength (MPa)	Ultimate Strain ($\%$)	Necking Strain ($\%$)	Young's Modulus[§] ($GPa \cdot m^{-1}$)	Toughness ($MJ \cdot m^{-3}$)
s_1	760.63	18.62	1.16	3.30	60.15
s_2	871.15	14.27	0.73	5.60	54.74
s_3	735.68	22.12	4.59	2.67	68.31

[§] Calculated at 10% strain.

Overall, these results support the high mechanical strength claims of CNT fibres but also allude to the reduction in those properties as the material undergoes torsional modifications. Conversely, the later fabrication modifications, such as twisting, can increase the breaking stains and dramatically decrease their stiffness, while the consecutive coating increases the necking strains and stiffness of the material. Finally, the consistency of the mechanical properties, especially regarding the manufacturer's specification, highlights the benefit of utilizing a commercial fibre product instead of in-house fabrication.

4.1.2 Electrical Properties

Similar to the mechanical tests, the objectives of the resistance measurements were to verify those reported by the manufacturer's specifications and to observe how each fabrication stage affected their resulting values. First, nine samples in their

pre-twisted and twisted-coiled and stretched formats were mounted in the Biotester and tested following the procedure described in Section 3.3.3. Then, four of these samples were placed on the conventional fabrication apparatus and underwent the final coating stage while stretched. Once cured, they were remounted and had their resistances remeasured. Resistances reported in Table 4.4 are normalized to pre-twisted lengths of the corresponding sample.

Table 4.4: Resistance vs Fabrication Stage Test Summary for 100 μm Samples

Sample	Resistance ($\Omega \cdot cm^{-1}$)			
	Pre-Twisted	Coiled	Stretched	Coated
s_1	0.3935	0.3947	0.4080	—
s_2	0.5355	0.5564	0.5688	—
s_3	0.9295	0.9741	1.0216	—
s_4	0.5155	0.5272	0.5478	—
s_5	0.4559	0.4762	0.4862	—
s_6	0.3776	0.3850	0.3876	0.3884
s_7	0.3273	0.3350	0.3416	0.3479
s_8	0.4263	0.4381	0.4472	0.5693
s_9	0.4401	0.4602	0.4615	0.4615

The pre-twisted resistances measured were significantly greater than the values mentioned in the specifications, reporting a mean of 0.4890 [$\sigma = 0.1774$] $\Omega \cdot cm^{-1}$ compared to 0.17±0.03 $\Omega \cdot cm^{-1}$ [68]. This can be explained by the connection resistance between the paperclip and the fibre, better described by a multi-resistor circuit shown in Figure 4.2. Additionally, due to fabrication tolerances, these connection resistances varied between samples, as indicated by the large σ, reducing the sample-sample resistive measurement significance.

Figure 4.2: Sample resistive model where R_{c1} and R_{c2} are the CNT-Paperclip connection resistances and R_{cnt} is the resistance of the fibre.

However, when looking at how those resistances changed within each sample, a clear trend appeared. As the yarns were twisted and coiled, their resistances increased by 1.6% on average. Ideally, when the current passes through the fibre, it tends to encounter the least resistance along the axial pathway of the CNT [86]. Such a system can be represented as a simple wire where the current only flows along a one-dimensional path demonstrated in Figure 4.3. This pathway is distorted when the fibre is twisted and coiled, and its new bunched spring formation connects the coiled potions along their perpendicular sides. This contact point has a greater resistance than the axial pathways but would allow electrons to jump between the

coils. Therefore as the coiling reduces the effective length of the fibre, it also lessens the distance the electrons need to travel.

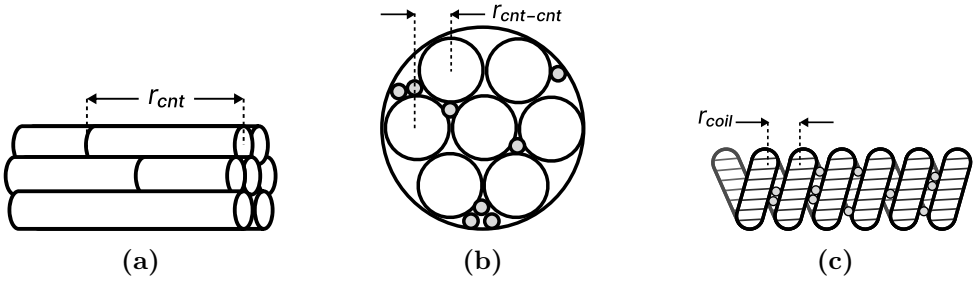

Figure 4.3: Summary of the various resistances within a CNT fibre bundle (a), its cross-section (b) and when twisted and coiled (c), where r_{cnt} is the resistance along a CNT, $r_{cnt-cnt}$ is the resistance between CNTs within a CNT fibre, and r_{coil} is the resistance between each coil. $r_{coil} >> r_{cnt-cnt} > r_{cnt}$. Gray circles represent epoxy globules.

While this represents the behaviour of an ideal conductive material as its geometry is modified, the CNT yarns have been shown to undergo microfractures when twisted [45], decreasing the axial connectivity in the process. Since the axial resistance plays a more significant role in determining the resulting resistance of the material, its effective increase due to torsional stresses exceeds the resistance decreases gained from coil contact. However, this does not discount the role inter-coil resistance plays altogether. Stretching the twisted-coiled yarns decreased the inter-coil contact, returning the preferred path to the axial direction and consequently increasing the fibre resistance a further 1.4% on average. Finally, the introduction of the coating was shown to have a lesser affect the overall resistance of the fibre compared to its stretched state, with only a mean increase of only 0.3%. Since the resistance is predominantly defined by the resistances of the internal CNT core and the pathway to that core is not altered through the coating process, the involvement of the epoxy on the composite's resistance is negligible. This is somewhat intuitive since introducing insulating material between parallel conductors should reduce its overall bandwidth, assuming inter-conductor electron transfer. In the case of these yarns, however, the leading pathway of the electrons is along the CNTs themselves [45], whose structure is not affected by the absorption of the epoxy coating. Furthermore, while the internal resistance of the epoxy is temperature dependant, as described in Section 4.2.2, its scale is vastly larger than that of the inter-CNT connections and thus can be ignored.

Generally, the greatest effector on the fibre's resistance was the torsional stresses that damage the structures of the fibre. While coiling can ideally decrease this effect, it is comparatively minimal in scale and did not play a significant role, ($t(16) = 0.1873; p = 8.5 \times 10^{-1}$), within these fibres. When stretched, this intercoil effect is lost, and the additional stress on the fibre further increases the overall resistance,

though the increases were less than 2%. Overall, the entire process resulted in a mean increase of the resistance of the sample by $\approx 3.3\%$. While the trends are apparent within each of these tests, there were a variety of areas that could have reduced the accuracy of the readings. Whether through the multiple mounting and unmounting stages required to test the samples, the two stages of stretching procedures, or, most notably, the welding quality between the solder, the paperclip and the CNT fibre, future work could benefit from improving each of these processes.

4.1.3 Electrothermal Response

As the thermal transfer medium for the infiltrated epoxy, the CNT fibre's ability to conduct thermal energy directly correlates to the actuator's performance. This series of tests aimed to determine the relationship between the voltage and the resulting temperature of the CNT core and how structural changes may play a role in modulating these values. Four 100 μm diameter CNT samples for each of the successive fabrication stages outlined in Section 3.3.3 underwent this series of tests using the procedure described in Section 3.3.4.

Joule heating is directly proportional to the voltage used to stimulate a conductor as described in (4.1), where Q is heat, V is voltage, R is the conductor's resistance, and t is the time the voltage is applied. This equation can also be rewritten to describe the relationship between the mass of the object m, its particular heat capacity C and the change in temperature ΔT. In the case of these tests, the application time, resistance, heat capacity and mass are constant for each sample, only with the fixed voltage being modulated. As such, a thermal response and ΔT proportional to the square of the voltage was expected.

$$Q = \frac{V^2}{R} \cdot t = m \cdot C \cdot \Delta T \tag{4.1}$$

$$Q \propto \frac{V^2}{R} \propto \Delta T \tag{4.2}$$

The first trend observed highlights the relationship between the applied voltage and the exponential increase in temperature at different fabrication stages. These temperature-voltage rates were shown to peak at the applied voltage of 1.9 V for the pre-twisted, twisted-coiled and stretched samples with 7.5, 15 and 12.5 ℃ $\cdot V^{-1}$ respectively, while the coated sample saw its largest increase at 1.7 V with 33.5 ℃ $\cdot V^{-1}$. The complete set of rate data can be seen in Table 4.5.

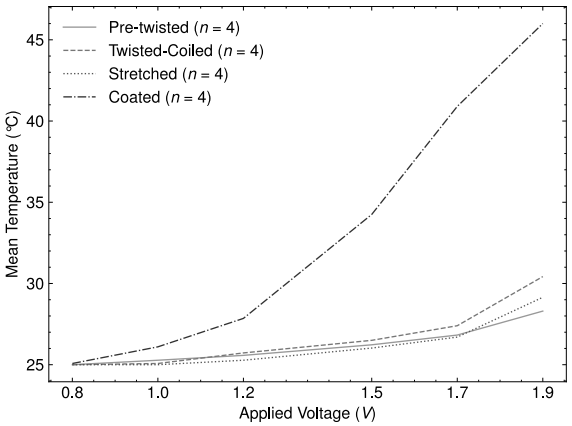

Figure 4.4: Fabrication stage comparison of the mean electrothermal responses.

Table 4.5: Mean Temperature-Voltage Rates of 100 μm Carbon Nanotube Samples at Selected Fabrication Stages

Fabrication Stage ($n = 4$)	Response Rate (℃ $\cdot V^{-1}$)				
	0.8-1.0 V	1.0-1.2 V	1.2-1.5 V	1.5-1.7 V	1.7-1.9 V
Pre-twisted	1.5	1.5	2.0	3.0	7.5
Coiled	0.5	3.0	2.7	4.5	15
Stretched	0.0	1.5	2.3	3.5	12.5
Coated	5.0	8.5	21.3	33.5	25.5

The difference in the rate and magnitude between the various sample sets alludes to changes in thermal conductivity due to their structure. The first transition from the pre-twisted to the twisted-coiled format, shown to increase the resistance of the sample in 4.1.2, should have decreased the heat produced by the conductor. However, the observed maximum mean temperature change from 28.3 [$\sigma = 0.6$] to 30.4 [$\sigma = 0.7$] ℃ was minimal when accounting for the standard deviation albeit statistically significant, ($t(6) = 4.7247; p = 3.2 \times 10^{-3}$). In the subsequent transition from the twisted-coiled to stretched stage with maximum mean temperatures going from 30.4 [$\sigma = 0.7$] ℃ to 29.2 [$\sigma = 0.2$] ℃ the difference was insignificant ($t(6) = -3.6093; p = 1.1 \times 10^{-2}$), mirroring the transitional resistance change. In contrast, the last transition from stretched to coated did show an exaggerated and significant increase in temperature, ($t(6) = 11.4188; p = 2.7 \times 10^{-5}$), from 29.2 [$\sigma = 0.2$] ℃ to 46.0 [$\sigma = 2.9$] ℃ even though it did not experience a resistance increase.

While it is clear the resistance does not play the primary role in determining the temperature response of these samples, even when including any changes due to temperature itself denoted by these material's temperature coefficient of ≈0.002 $ppm \cdot ℃^{-1}$ [87], it points to the underlying sample structure as the main contributor to the response. For the pre-twisted samples, the entire length of precursor CNT

fibre is exposed during the test, providing additional cooling along its surface area due to the ambient atmosphere. This surface area is reduced when it transitions to a twisted-coiled format and then increased when it is stretched, aligning more with the behaviour observed. Furthermore, when looking at the coated samples, the epoxy coating surrounds the internal conductor, insulating it during the stimulation. As such, the fabrication steps that have been shown to reduce the exposed conductive area of the underlying fibres positively influenced the resulting thermal response.

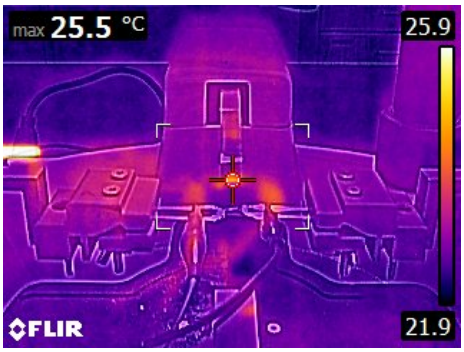

Figure 4.5: Manual thermal capture through the FLIR E6™ thermal camera.

Though these tests could discern the overall trends of these thermal responses, the low refresh rate of the thermal camera, in conjunction with the quick activation time of the sample, restricted thermal measurements to snapshots only. Additionally, attempts to precisely and consistently lock onto the relatively small heated area, shown in Figure 4.5, proved difficult and could be improved with a dedicated mounting apparatus in future experiments.

4.1.4 Electromechanical Response

Four samples were fabricated for each fabrication stage to undergo the Isometric stress and Isotonic strain testing procedure outlined in Section 3.3.5. The results of these test series are presented in the following subsections.

4.1.4.1 Isometric Stress Testing

The actuation of the samples within the first three stages of the fabrication process is driven by the electromagnetic forces between the parallel CNT fibres that make up the fibre bundle, described in Section 2.3.2. Beginning with the pre-twisted CNT fibre, a small response was observed at higher voltages though its magnitude

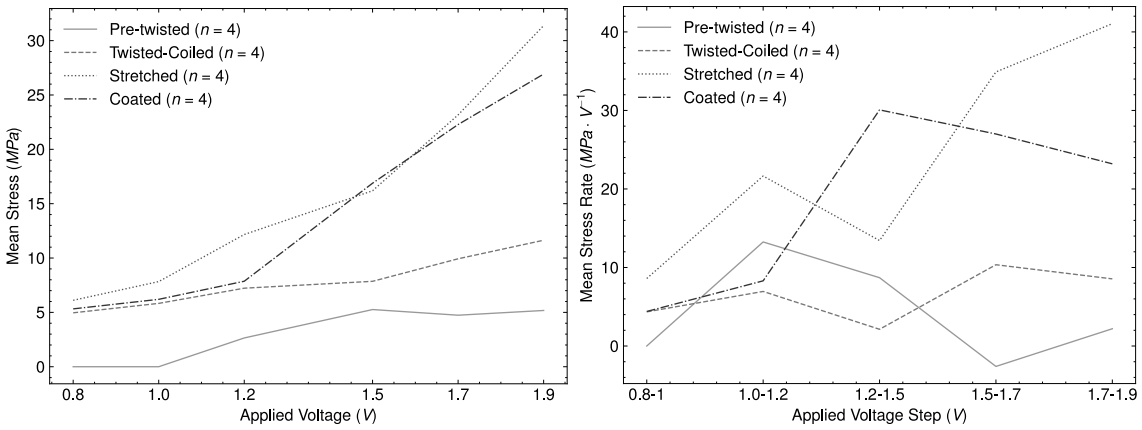

(a) **(b)**

Figure 4.6: Mean contractile engineering stress vs applied voltage at selected fabrication stages (a) and the corresponding stress-voltage rate between each voltage step (b).

remained relatively small. This could be due to the small amount of embedded twist in the fibre created during its commercial fabrication process, though more precise measurements would be required to validate this hypothesis due to the magnitudes falling within the Biotester's $\pm 30mN$ fluctuation tolerance.

When the sample is twisted and coiled, the increase in electromagnetic forces is depressed by the restricted space between each coil, limiting the actuation. In this state, the expressed stresses were limited to ≈5-14 MPa as seen in Table B.2, although a significant increase ($t(6) = 6.5296; p = 6.1 \times 10^{-4}$), when compared to its precursor state at $1.9v$. Once additional space was introduced between these coils via a 15% stretch, the added room allowed the actuation to occur more effectively and led to a signifcantly ($t(6) = 12.5011; p = 1.6 \times 10^{-5}$) greater generated forces from ≈5-34 MPa (Table B.3).

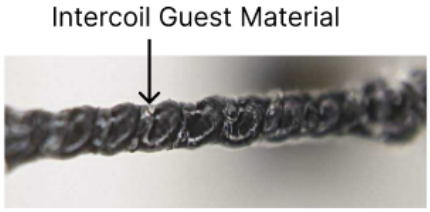

Figure 4.7: Sample with epoxy guest material in between coils impeding full movement.

Finally, the coated samples experienced a more complex actuation mechanism through the electromagnetic forces of the underlying CNT yarn and the reduction of stiffness within the epoxy coating resisting the contraction. Compared to the

uncoated stretched samples, this modification diminished the maximum contractile stress response ($t(6) = -3.1636; p = 1.9 \times 10^{-2}$), measuring between ≈5-29 MPa for the tested voltage range (Table B.4).

Similarly, a reduced stress-voltage rate could also be seen between various voltages, as shown in Figure 4.6. Since the coating resists the movement of the underlying yarn during stimulation, the time required to achieve a sufficient temperature to reduce its stiffness must be considered. Further, introducing a guest material between the coils, depicted in Figure 4.7, restricts the distance they can travel when contracting, dampening its response.

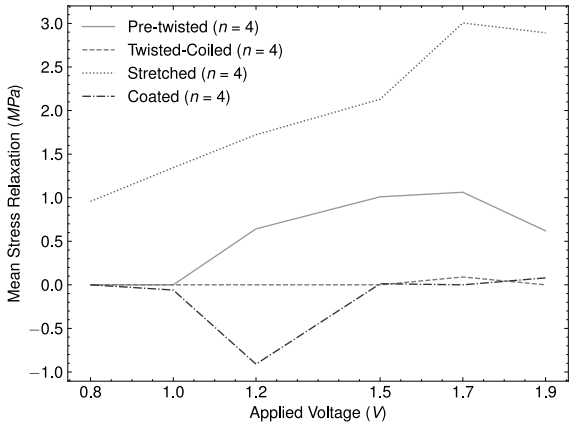

Figure 4.8: Stress drop at consecutive voltage intervals during isometric test cycles for pre-twisted, twisted-coiled, stretched and coated sample sets.

Actuation cycles also exhibited force drops over consecutive voltage intervals highlighted in Figure 4.8. This behaviour appeared to affect the stretched samples most significantly, with to an increasing degree as the voltage increased. Coated samples, on the other hand, experienced the opposite effect, a stress increase after relaxation, particularly around the epoxy relaxation point of 1.2 V. This shows the slight loosening of the tension within the encased fibre after the completion of an actuation cycle caused by the momentary reduction in the surrounding epoxy's stiffness.

Overall, the increase in voltage was shown to increase the force generated and the rate at which it occurred, with a relatively minor stress loss between voltage test intervals. This rate was non-constant, however, with the most significant increase between 1.5-1.7 V for most of the fabrication stages apparent in Table B.6. The inclusion of greater twisting in the form of coils, enhanced with adequate spacing between such coils through stretching, increased the mean expressed stresses most significantly from ≈14 MPa in the twisted-coiled samples to ≈34 MPa in the stretched samples. Moreover, with the epoxy coating, the mechanical responses and

their corresponding rate were reduced due to the mechanical resistance created by the guest material, though these were still larger than the pre-twisted samples.

4.1.4.2 Isotonic Strain Testing

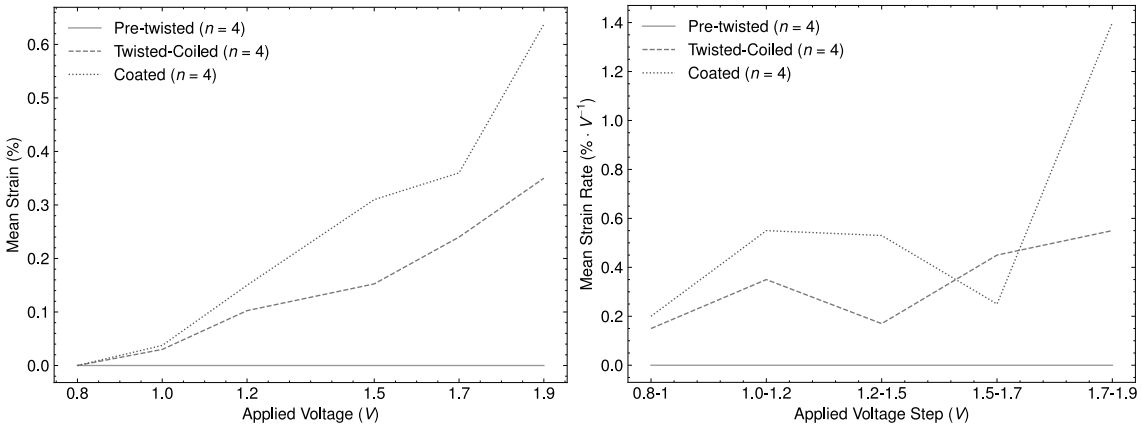

(a) **(b)**

Figure 4.9: Mean contractile engineering strain vs applied voltage at selected fabrication stages using a 4 g load (a) and the corresponding strain-voltage rate between each voltage step (b).

Strains for all samples were relatively small regardless of the fabrication stage, with a peak of 0.64%, and increased with increasing voltage, similar to the measured isometric responses. The pre-twisted yarns showed the weakest performance, lacking the superior electromagnetic forces that accompany their twisted-coiled alternatives, and, in most cases, did not measure any strains under each of the voltages supplied. With additional coiling, the effectiveness of the geometry change requires sufficient spacing between the coils to actuate. Using a load of 4 g was not large enough to provide adequate spacing between the coils resulting in a maximum strain of 0.35 [σ = 0.06]%, a small but significant increase, ($t(6) = 12.2474; p = 1.8 \times 10^{-5}$), compared to the pre-twisted sample set under the.

The strains were much more significant, ($t(6) = 3.1105; p = 2.1 \times 10^{-2}$), when the yarns were coated, measuring 0.62 [σ = 0.16]%. Since the coils are encased in their stretched state, the stimulation releases the tension and allows them to contract as if they were sufficiently loaded in their stretched state. The applied voltage was integral to this response, with limited actuation occurring before 1.2 V, owing to the unchanged stiffness of the epoxy coating prior to this point. The pre-loaded state of the coated yarns is the primary benefit of their design, removing their dependence on an external load to achieve continuous actuation.

The magnitude of strain appeared most affected by the space available for contraction, and the magnitude of the electromagnetic forces between the parallel fibres, coiled or not, could optimally generate. Furthermore, the applied voltage's role was not insignificant, as without sufficient thermal energy resulting from the current running through the CNT fibre, the epoxy coating remained stiff, resisting any internal contraction of the high tension CNT fibre core.

4.1.5 Summary

The process of converting the precursor DexMat Galvorn CNT-HS™ fibres into the fabricated stiffness-variable actuator results in the reduction of some of the underlying properties of the base material. The magnitude of these diminished properties can vary greatly, such as the 65% decrease in strength compared to the 3% decrease in conductance, potentially limiting applications that depend on the more affected properties. Regarding their resulting actuation abilities, the process of twisting+coiling and stretching improves the contractile stresses expressed and the contractile strains when loaded, which is complemented by the built-in strain resetting mechanism of the coating process.

Table 4.6: Stiffness-Variable Actuator Fabrication Stage Transition Experimental Summary

Fabrication Stage Δ	Effect on Quality						
	Resistance ($\Omega \cdot cm^{-1}$)	Surface Temperature (℃)	Tensile Strength* (MPa)	Ultimate Strain* (%)	Stiffness ($GPa \cdot m^{-1}$)	Contractile*	
						Stress (MPa)	Strain (%)
Pre-twisted→ Twisted-Coiled	↑ (1.6%)	NC†	↓ (-63.8%) ⟨1993→722⟩	↑ (648%) ⟨7.2→53.5⟩	↓ (-96.6%) ⟨32.1→1.1⟩	↑ (121%) ⟨5.26→11.64⟩	↑ ⟨0.00→0.35⟩
Twisted-Coiled→ Stretched	↑ (1.4%)	NC†	N/A	N/A	N/A	↑ (169%) ⟨11.64→31.38⟩	N/A
Stretched→Coated	↑ (0.3%)	↑ (57.5%) ⟨29.2→46.0⟩	↑ (9.3%) ⟨722→789⟩	↓ (-38.8%)§ ⟨53.5→33.3⟩	↑ (251%) ⟨1.1→3.9⟩	↓ (-14.2%) ⟨31.38→26.92⟩	↑ (82.8%) ⟨0.35→0.62⟩

† No change
* Presented stresses and strains are engineering stresses and strains.
§ Calculated by adding 15% to the mean strain measured.

4.2 PRO-SET® Epoxy Properties

4.2.1 Mechanical Properties

The stiffness-variable actuator design depends on the variable stiffness of the epoxy as it undergoes a temperature change. To properly characterize these properties, epoxy samples were created and mechanically tested within the Instron 4202 Universal Tensile Machine™ under different strain rates and applied temperatures.

The first test series conducted was a monotonic to failure uniaxial tensile test using a 5 $mm \cdot s^{-1}$ strain rate at room temperature. The second test series, a load-unload test, was performed with strain rates of 5 $mm \cdot s^{-1}$, and 8 $mm \cdot s^{-1}$ over two cycles per sample. The load-unload series was repeated for three temperatures, room temperature, 30, and 50 ℃ supplied by a Wagner HT3500™ mounted heat gun and verified by a FLIR E6™ thermal camera. The heat gun was used at its lowest setting (121℃) until the sample reached the desired temperature before initiating the test.

Two types of samples were created for this investigation, a thinner sample measuring 28x7.5x1 *mm* (LxWxD) and a thicker sample set 28x7.5x1.5 *mm*. In the mould shown in Appendix C.1, this accounted for 6 and 10 *ml*, respectively. Each of these test series were performed on the thinner samples, while the thicker samples only underwent the monotonic to failure uniaxial tensile tests. Each test series was repeated with three samples.

4.2.1.1 Monotonic to Failure Uniaxial Tensile Testing

The thinner samples had a tensile strength of 38.90 [$\sigma = 3.95$] MPa with a corresponding ultimate strain of 4.29 [$\sigma = 0.09$]%. When the samples were thicker, these values increased to 44.37 [$\sigma = 0.34$] MPa and 6.33 [$\sigma = 0.44$]%, respectively. Additionally, the minor necking strains and complementary low toughness of 0.60 and 0.99 [$\sigma = 0.26$] $MJ \cdot m^{-3}$, seen in Tables 4.7 and 4.8, for the thin and thick samples respectively highlighted the material's brittleness at room temperature.

More significant changes in the fracture behaviour were illustrated by the shift in sample starting temperature at room temperature, 30 and 50 ℃ highlighted in Figure 4.11. The linearity of the stress-strain curves is completely gone, with clear signs of deformation. This is most apparent when looking at the peak tensile strength

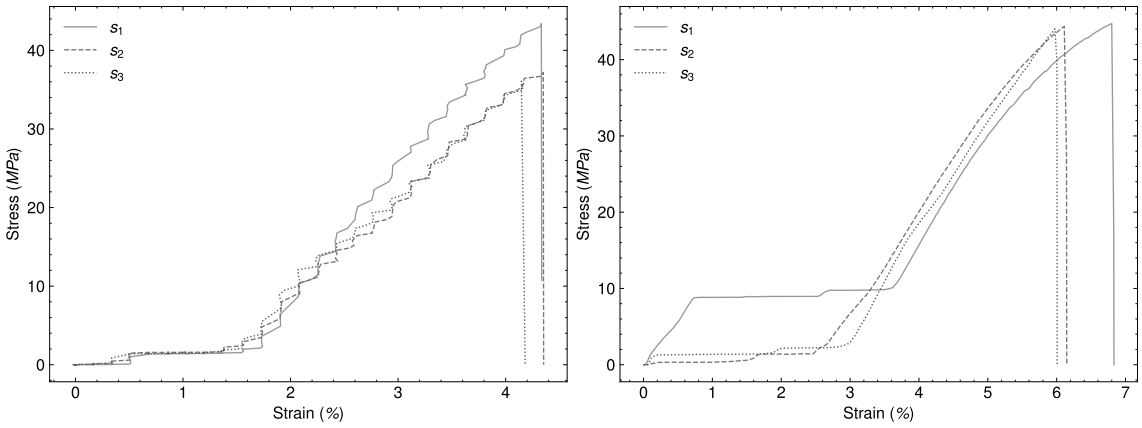

Figure 4.10: Monotonic to failure uniaxial tensile test of a (a) thin epoxy sample and (b) thick epoxy sample at room temperature and using a strain rate of 5 $mm \cdot s^{-1}$.

Table 4.7: Monotonic to Failure Uniaxial Summary of Thin Epoxy Samples with a 5 $mm \cdot s^{-1}$ Strain Rate At Room Temperature

Sample	Tensile Strength (MPa)	Ultimate Strain ($\%$)	Necking Strain ($\%$)	Young's Modulus[§] ($GPa \cdot m^{-1}$)	Toughness ($MJ \cdot m^{-3}$)
s_1	43.41	4.34	0.00	0.69	0.67
s_2	37.21	4.35	0.00	0.58	0.59
s_3	36.07	4.18	0.04	0.62	0.54

[§] Calculated at 2.5% strain.

Table 4.8: Monotonic to Failure Uniaxial Summary of Thick Epoxy Samples with a 5 $mm \cdot s^{-1}$ Strain Rate At Room Temperature

Sample	Tensile Strength (MPa)	Ultimate Strain ($\%$)	Necking Strain ($\%$)	Young's Modulus[§] ($GPa \cdot m^{-1}$)	Toughness ($MJ \cdot m^{-3}$)
s_1	44.73	6.83	0.03	0.60	1.28
s_2	44.35	6.15	0.04	0.67	0.89
s_3	44.04	6.01	0.03	0.64	0.79

[§] Calculated at 5% strain.

and ultimate strains of these higher temperature samples outlined in Tables 4.7, 4.9 and 4.10. As the starting temperature rose, the tensile strengths dropped, first from 38.90 [$\sigma = 3.95$] to 24.30 [$\sigma = 1.66$] ($t(2) = -9.4452; p = 1.1 \times 10^{-2}$) and then further to 6.75 [$\sigma = 2.94$] ($t(6) = -13.5054; p = 5.4 \times 10^{-3}$).

A similar trend was also seen in their respective stiffness, starting at 0.64 [$\sigma = 0.04$] $GPa \cdot m^{-1}$ at room temperature and dropping to 0.49 [$\sigma = 0.25$] $GPa \cdot m^{-1}$ at 30 ℃ ($t(2) = -9.4452; p = 1.1 \times 10^{-2}$) and then 0.10 [$\sigma = 0.02$] $GPa \cdot m^{-1}$ at 50 ℃ ($t(2) = -13.5054; p = 5 \times 10^{-3}$).

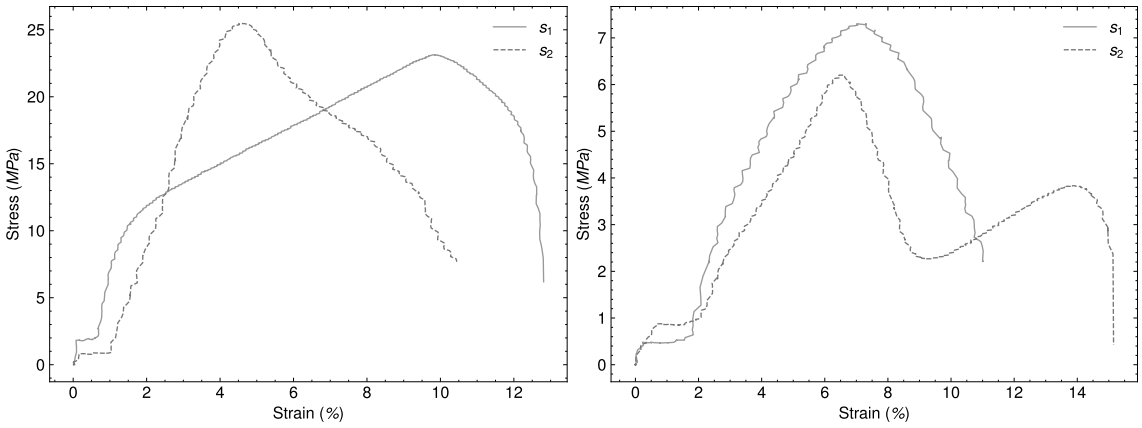

Figure 4.11: Monotonic to failure uniaxial tensile test of a thin epoxy sample at a strain rate of 5 $mm \cdot s^{-1}$ and (a) 30 ℃ and (b) 50 ℃.

Table 4.9: Monotonic to Failure Uniaxial Summary of Thin Epoxy Samples at 30 ℃

Sample	Tensile Strength (MPa)	Ultimate Strain ($\%$)	Necking Strain ($\%$)	Young's Modulus[§] ($GPa \cdot m^{-1}$)	Toughness ($MJ \cdot m^{-3}$)
s_1	23.13	12.96	2.97	0.67	2.10
s_2	25.48	10.45	5.74	0.31	1.56

[§] Calculated at 1.5% strain.

Table 4.10: Monotonic to Failure Uniaxial Summary of Thin Epoxy Samples at 50 ℃

Sample	Tensile Strength (MPa)	Ultimate Strain ($\%$)	Necking Strain ($\%$)	Young's Modulus[§] ($GPa \cdot m^{-1}$)	Toughness ($MJ \cdot m^{-3}$)
s_1	7.31	11.00	3.69	0.12	0.49
s_2	6.20	15.15	8.69	0.09	0.48

[§] Calculated at 4% strain.

4.2.1.2 Load-Unload Uniaxial Tensile Testing

Though the monotonic to failure tensile tests shed light on the boundary limits of the material, a more useful test is looking at its load-unload response as a more common operating environment within the stiffness-variable actuator design. The first series of tests explored the strain rate's effect on the mechanical properties of the thin epoxy samples. As shown in Figure 4.12, and the Tables 4.11 and 4.12, the increase in strain rate from 5-8 $mm \cdot s^{-1}$ had no significant effect on these properties.

In contrast, changes were much more distinct when testing the effect of the operating temperature on the mechanical properties, highlighted in Figure 4.13. When the epoxy's starting temperature increased, the material's stiffness decreased as shown

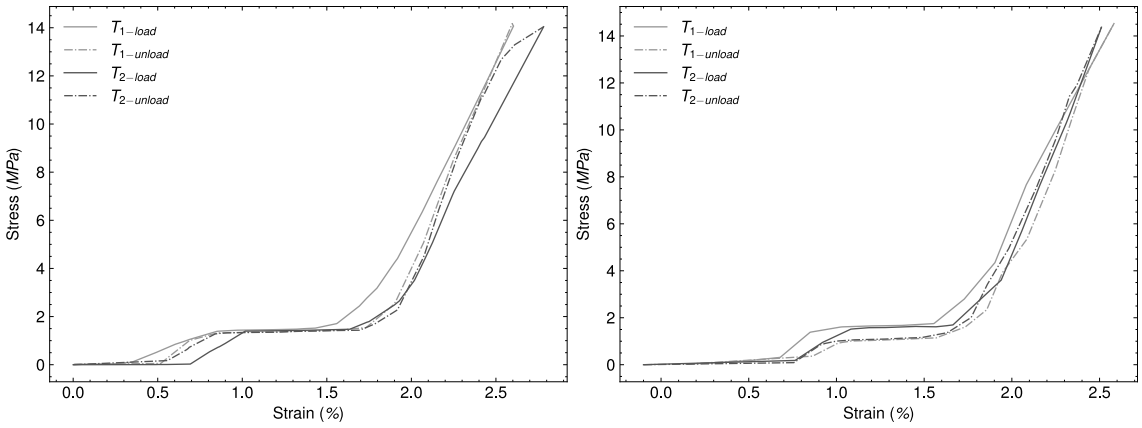

Figure 4.12: Two successive cycles, T_1 and T_2, of a load-unload uniaxial tensile test on a thin epoxy sample at a strain rate of (a) 5 $mm \cdot s^{-1}$ and (b) 8 $mm \cdot s^{-1}$ at room temperature.

Table 4.11: Load-Unload Tensile Test Summary of Thin Epoxy Samples with a 5 $mm \cdot s^{-1}$ Strain Rate At Room Temperature

Sample	Tensile Strength (MPa)	Ultimate Strain (%)	Young's Modulus ($GPa \cdot m^{-1}$)	Toughness ($MJ \cdot m^{-3}$)	Hysteresis[§0] ($MJ \cdot m^{-3}$)
s_{1a}	14.31	2.60	0.55[§1]	0.09 (-0.08)	0.009
s_{1b}	14.28	2.78	0.46[§1]	0.09 (-0.10)	0.012
s_{2a}	14.28	3.11	0.25[§1]	0.10 (-0.07)	0.033
s_{2b}	14.28	3.11	0.25[§1]	0.10 (-0.07)	0.033
s_{3a}	14.05	2.08	0.63[§2]	0.07 (-0.06)	0.010
s_{3b}	14.09	2.03	0.69[§2]	0.06 (-0.06)	0.032

[§0]Calculated by subtracting the toughness from the load and unload measurements.
[§1]Calculated at 2.5% strain.
[§2]Calculated at 2% strain.

in Tables 4.13 and 4.14, following the trend previously observed in the monotonic to failure testing. Additionally, the hysteresis became exaggerated with increasing temperature due to the difference between the cool-down rate of the material and the unload strain rate. This was seen most signifcantly between room temperature to 30 ℃ ($t(10) = 4.0973; p = 2.1 \times 10^{-3}$), and less significantly with the transition from 30 to 50 ℃ ($t(10) = 2.6367; p = 2.4 \times 10^{-2}$).

Maintaining the starting temperature proved to be more difficult with the 50 ℃ samples, resulting in a quicker drop of the temperature between 50 and 30 ℃ and the change in tensile responses between the successive cycles within the 50 ℃ testing set. Secondary cycles of these samples were in the range of 43 to 48 ℃ though hysteresis trends remained consistent. Additional sample data can be found in Appendix C.2.

Table 4.12: Load-Unload Tensile Test Summary of Thin Epoxy Samples with a 8 $mm \cdot s^{-1}$ Strain Rate At Room Temperature

Sample	Tensile Strength (MPa)	Ultimate Strain ($\%$)	Young's Modulus ($GPa \cdot m^{-1}$)	Toughness ($MJ \cdot m^{-3}$)	Hysteresis[§0] ($MJ \cdot m^{-3}$)
s_{1a}	14.26	2.58	0.41[§1]	0.09 (-0.07)	0.018
s_{1b}	13.92	2.50	0.41[§1]	0.07 (-0.07)	0.001
s_{2a}	13.80	1.92	0.40[§2]	0.05 (-0.05)	0.000
s_{2b}	14.22	2.08	0.38[§2]	0.06 (-0.06)	0.002
s_{3a}	14.26	2.58	0.41[§1]	0.09 (-0.08)	0.011
s_{3b}	13.82	2.48	0.42[§1]	0.07 (-0.07)	0.010

[§0]Calculated by subtracting the toughness from the load and unload measurements.
[§1]Calculated at 2.2% strain.
[§2]Calculated at 1.7% strain.

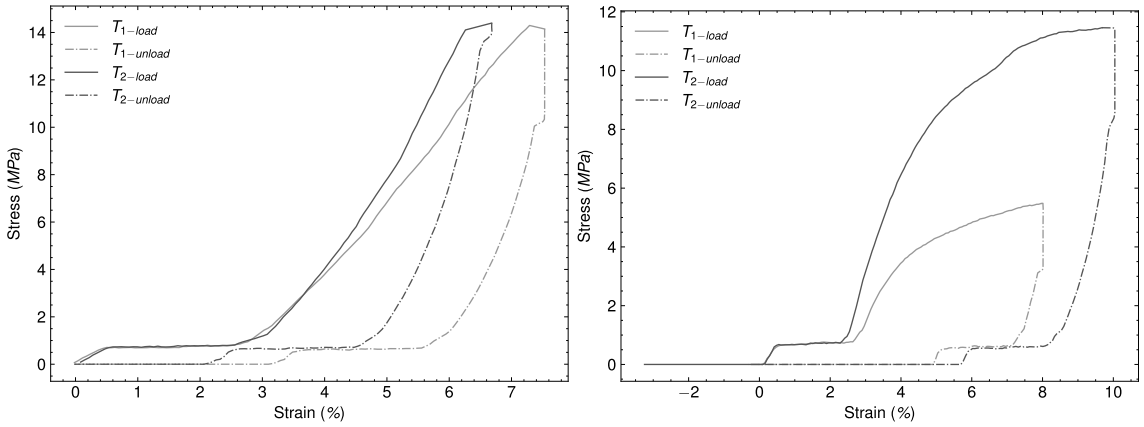

Figure 4.13: Two successive cycles, T_1 and T_2, of a load-unload uniaxial tensile test on a thin epoxy sample at a strain rate of 5 $mm \cdot s^{-1}$ and initial temperature of (a) 30 ℃ and (b) 50 ℃.

4.2.2 Electrothermal Properties

In addition to the epoxy's mechanical abilities, how the material behaves electrically could also play an essential role in the stiffness-variable actuator design due to the driving mechanism being electrical. Here, a testing apparatus, illustrated in Figure 4.14, was created to observe this behaviour as the temperature of the material was increased and as the material returned to room temperature during cool down.

The resin sample was created using the recommended 3-1 ratio of the PRO-SET® 125 epoxy resin and PRO-SET® 229 epoxy hardener and allowed to set in a cylindrical vessel 11.3 mm deep, 30.6 mm wide with two paper clip leads ≈2 cm

Table 4.13: Load-Unload Tensile Test Summary of Thin Epoxy Samples with a 5 $mm \cdot s^{-1}$ Strain Rate At 30 ℃

Sample	Tensile Strength (MPa)	Ultimate Strain ($\%$)	Young's Modulus ($GPa \cdot m^{-1}$)	Toughness ($MJ \cdot m^{-3}$)	Hysteresis[§0] ($MJ \cdot m^{-3}$)
s_1a	14.30	7.29	0.14[§1]	0.38 (-0.10)	0.278
s_1b	14.40	6.68	0.16[§1]	0.30 (-0.14)	0.164
s_2a	14.32	6.61	0.18[§1]	0.31 (-0.06)	0.249
s_2b	14.18	5.62	0.21[§1]	0.25 (-0.04)	0.163
s_3a	14.10	4.83	0.27[§2]	0.22 (-0.09)	0.132
s_3b	14.23	4.11	0.35[§2]	0.15 (-0.12)	0.032

[§0]Calculated by subtracting the toughness from the load and unload measurements.
[§1]Calculated at 5% strain.
[§2]Calculated at 4% strain.

Table 4.14: Load-Unload Tensile Test Summary of Thin Epoxy Samples with a 5 $mm \cdot s^{-1}$ Strain Rate At 50 ℃

Sample	Tensile Strength (MPa)	Ultimate Strain ($\%$)	Young's Modulus ($GPa \cdot m^{-1}$)	Toughness ($MJ \cdot m^{-3}$)	Hysteresis[§0] ($MJ \cdot m^{-3}$)
s_{1a}	5.48	7.95	0.09[§1]	0.23 (-0.03)	0.216
s_{1b}	11.46	9.68	0.16[§1]	0.64 (-0.04)	0.482
s_{2a}	3.32	10.18	0.07	0.27 (-0.05)	0.212
s_{2b}	6.34	12.01	0.08	0.51 (-0.03)	0.480
s_{3a}	5.26	9.10	0.05[§3]	0.31 (-0.06)	0.260
s_{3b}	10.02	9.66	0.12[§3]	0.66 (-0.03)	0.630

[§0]Calculated by subtracting the toughness from the load and unload measurements.
[§1]Calculated at 4% strain.
[§2]Calculated at 3.5% strain.
[§3]Calculated at 6% strain.

apart from each other, as shown in Figure 4.14. Each paperclip lead was connected to a Keithley multimeter lead pair to obtain the four-point resistance measurement previously described in Section 3.3.3.

The resin was heated using a Wagner HT3500™ heat gun, set to 121℃ mounted alongside the sample at a distance of ≈10 *cm*. A FLIR E6™ thermal camera tracked the resin temperature in real-time and was also mounted alongside the sample to ensure stable reading during the lengthy test campaign. Finally, a video was taken of the equipment during the test campaign and post-analyzed to record the temperature and its corresponding resistance measurement to capture both readings. The heat application continued until the epoxy was visibly bubbling, at which point the heat gun was switched off. The temperate measurement continued until the epoxy returned to its starting resistance value, completing the test.

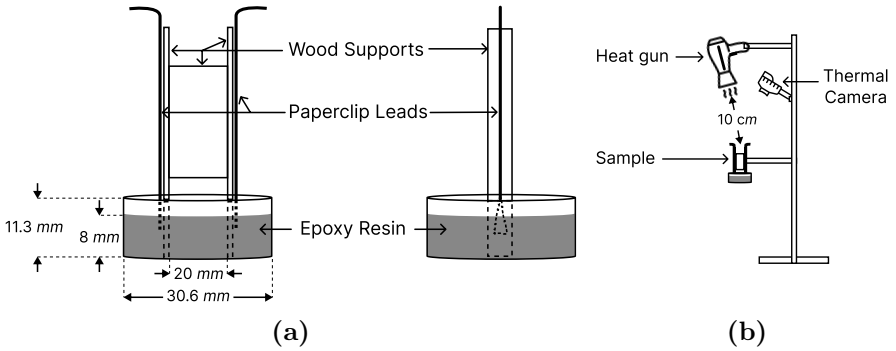

Figure 4.14: Epoxy electrothermal test sample (a) in its front (left) and side (right) views, and (b) the corresponding test setup.

The initial resistance measurements were out of range for the multimeter, denoting an open-circuit behaviour of the resin setup at room temperature. As the temperature increased from 24 to 60 ℃, the resistance exponentially decreased from greater than 400 $M\Omega$ to ≈20 $M\Omega$ before settling at ≈4 $M\Omega$ around 80 ℃. While this change is significant relative to their original values, the resistance in the epoxy is substantially larger than the resistances measured in the CNT fibre, alluding to a minor role as a conductor within the stiffness-variable actuator composite.

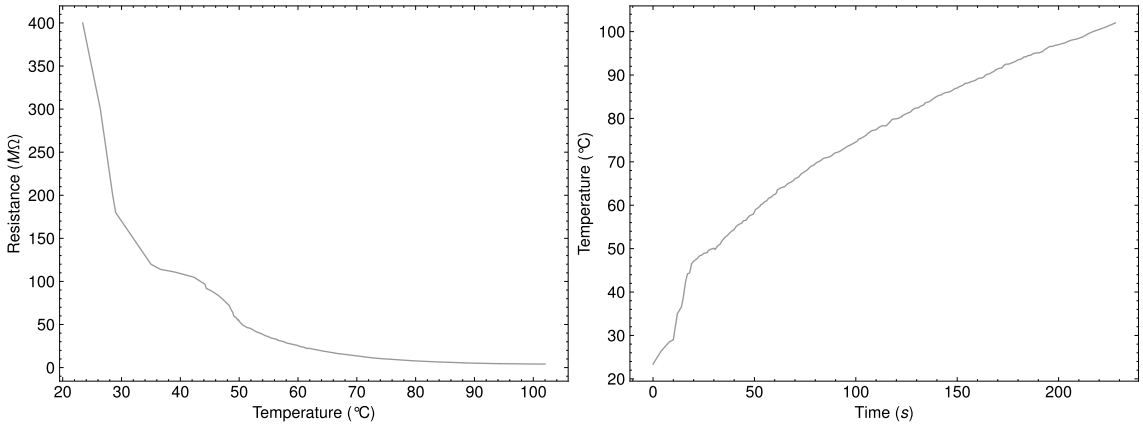

Figure 4.15: Electrothermal response of the epoxy when heated with the (a) resistance vs temperature and (b) temperature vs time.

4.2.3 Summary

Of the two parameters investigated, the temperature plays the most significant role in the pertinent properties of the stiffness-variable actuator design, particularly the stiffness. Furthermore, since the thickness investigation did not provide considerable differences within the measured properties at these scales, it can be inferred that the minuscule amounts used in the coating would have substantially smaller values. It should also be noted that these tests solely focused on the epoxy, not its interaction with the epoxy yarns' fibrous material, which could change these properties. Nevertheless, understanding how these two parameters affect the overall properties of the epoxy lends insights into future actuator designs that leverage epoxy composites.

Table 4.15: Epoxy Experimental Summary

Design / Operational Parameter	Δ	Effect on Quality				
		Resistance ($M\Omega$)	Tensile Strength* (MPa)	Ultimate Strain* (%)	Stiffness ($GPa \cdot m^{-1}$)	Ductility ($MJ \cdot m^{-3}$)
Thickness [mm]	$\uparrow$ $1.5 \rightarrow 2.5$	N/A	$\downarrow$ (13.9%) $\langle 38.90 \rightarrow 44.37 \rangle$	$\uparrow$ (45.9%) $\langle 4.29 \rightarrow 6.33 \rangle$	NC† $\langle 0.63 \rightarrow 0.64 \rangle$	$\uparrow$ (65.0%) $\langle 0.63 \rightarrow 0.99 \rangle$
Temperature [℃]	$\uparrow$ [1] $[22 \rightarrow 80]$ [2] $[22, 30, 50]$	$\downarrow^1$ $\langle \infty \rightarrow 4 \rangle$	$\downarrow^2$ $\langle 38.90, 24.30, 6.75 \rangle$	$\uparrow^2$ $\langle 4.29, 11.63, 13.07 \rangle$	$\downarrow^2$ $\langle 0.64, 0.49, 0.10 \rangle$	$\nearrow\searrow^2$ $\langle 0.99, 1.83, 0.48 \rangle$

† No change
* Presented stresses and strains are engineering stresses and strains.

Chapter 5

Experimental Evaluation of Stiffness-Variable Actuator

The stiffness-variable actuator design has many fabrication and operational parameters that can be modified to alter its performance. With the extensive characterizations of its underlying components in Chapter 4, an evaluation can be conducted to examine how those fabrication parameters can elevate or hinder the resulting actuator's capabilities. This chapter investigates three of these fabrication parameters; the diameter of the inner CNT material, the pre-stretch within the CNT coil and the epoxy coating application interval, to determine their effect on the mechanical and electrical properties of the actuator and includes comparisons to its uncoated twisted-coiled precursor design where applicable. This is followed by a summary of the evaluation results and how such design decisions should be leveraged for future applications is presented.

5.1 Effects due to Precursor Fibre Diameter

5.1.1 Fabrication Procedure and Sample Descriptions

The first parameter explored was the diameter of the CNT fibre within the actuator. Three products of varying diameters were selected from the Dexmat commercial offerings, the 40 μm CNT-HS fibre, the 100 μm CNT-HS fibre and the 200 μm yarn to be investigated for this parameter. Unfortunately, initial work attempting to fabricate samples with the 40 μm fibre failed to withstand the twisting process, fracturing before reaching coil activation. Furthermore, while the first two are described as single filament, untwisted and unbraided fibres, the 200 μm is a multifilament yarn made with a combination of different sized 20-30 μm single filaments in a braided fashion. This adds variability to the parameter analysis, but without additional single filament products that could withstand the fabrication procedure, this limitation was accepted to explore the trends that could occur with larger diameter materials, albeit not ideal.

The fabrication process outlined in Section 3.2.2 was followed for the 100 μm and 200 μm sample sets, with a constant coiling load of 70 g and a pre-stretch of 20%. For the comparative twisted-coiled samples, the pre-stretch was applied using the Biotester to reduce variability between sample stretching and testing. A summary of the sample's fabrication properties can be seen in the Tables 5.1 to 5.4.

Table 5.1: Fabrication Properties of 100 μm Carbon Nanotube Stiffness-Variable Samples with 20% Pre-stretch

Sample	Length (cm)		Pre-stretch (%)	MD (μm)	SI	T_{tot}	T_c	$\Omega \cdot cm^{-1}$
	Initial	Final						
s_1	2.45	1.15	18.92	97.00	0.97	39.25	22.08	0.3260
s_2	2.46	1.06	18.95	92.00	0.92	40.22	22.34	0.3389
s_3	2.43	1.35	19.64	69.44	0.69	41.20	23.90	0.3195

Table 5.2: Fabrication Properties of 200 μm Carbon Nanotube Stiffness-Variable Samples with 20% Pre-stretch

Sample	Length (cm)		Pre-stretch (%)	MD (μm)	SI	T_{tot}	T_c	$\Omega \cdot cm^{-1}$
	Initial	Final						
s_4	2.33	0.77	22.77	204.00	1.02	19.76	13.32	0.1378
s_5	2.62	1.05	22.79	166.00	0.82	20.58	13.34	0.1033
s_6	2.32	1.12	20.17	164.55	0.82	18.53	13.36	0.1295

Table 5.3: Fabrication Properties of 100 μm Carbon Nanotube Twisted-Coiled Samples with 20% Pre-stretch

Sample	Length (cm)		Pre-stretch (%)	MD (μm)	SI	T_{tot}	T_c	$\Omega \cdot cm^{-1}$
	Initial	Final						
s_7	3.25	1.39	20.63	99.31	0.99	40.62	21.85	0.4175
s_8	2.72	1.14	20.00	115.10	1.15	37.84	18.00	0.5500
s_9	1.92	0.81	20.57	101.56	1.02	44.39	20.89	0.4992

Table 5.4: Fabrication Properties of 200 μm Carbon Nanotube Twisted-Coiled Samples with 20% Pre-stretch

Sample	Length (cm)		Pre-stretch (%)	MD (μm)	SI	T_{tot}	T_c	$\Omega \cdot cm^{-1}$
	Initial	Final						
s_{10}	2.77	0.91	19.86	234.03	1.17	24.14	15.85	0.1434
s_{11}	2.79	0.74	20.90	231.60	1.16	22.58	11.83	0.2157
s_{12}	2.92	0.80	20.26	225.00	1.13	21.58	13.01	0.1807

5.1.2 Electrical Properties

As seen in each of the fabricated sample sets, increasing the underlying material diameter results in a decrease of the resistance within the sample. The stiffness-variable actuators (the coated samples) experienced a significant decrease of 62.4% ($t(4) = -17.2556; p = 6.6 \times 10^{-5}$), with mean values of 0.3281 [$\sigma = 0.0080$] $\Omega \cdot cm^{-1}$ for 100 μm samples and 0.1235 [$\sigma = 0.0147$] $\Omega \cdot cm^{-1}$ for 200 μm. For the twisted-coiled samples, a similar decrease was seen at 63.2% ($t(4) = -7.0415; p = 2.1 \times 10^{-3}$), accompanied by a mean values of 0.4890 [$\sigma = 0.0545$] $\Omega \cdot cm^{-1}$ for the 100 μm samples and 0.1799 [$\sigma = 0.0295$] $\Omega \cdot cm^{-1}$ for the 200 μm samples.

These results follow the inherent difference of commercial product's properties outlined in Table 2.1. where the 200 μm fibres conductivity was half that of the 100 μm fibres. The findings for both the stiffness-variable actuators and the twisted-coiled actuators noted above follow this trend, reaffirming the behaviour determined in Section 4.1.2 whereby the resistance within the CNT is the primary factor for the overall resistance of the actuator.

5.1.3 Electrothermal Response

The electrothermal response results, summarized in Figure 5.1, show a surface temperature decrease as the core's diameter increases, given the same stimuli.

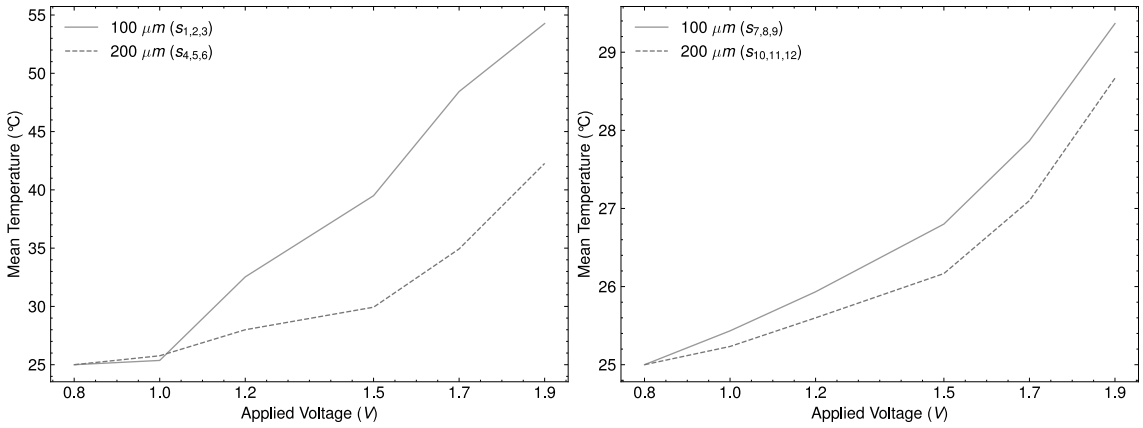

(a) **(b)**

Figure 5.1: Mean temperature vs applied voltage for the fabricated (a) stiffness-variable and (b) twisted-coiled sample sets with 100 and 200 μm CNT fibre diameters.

At a glance, this trend counters the relationship described by (4.2) where the heat is directly proportional to the applied power. However, as these resistances decrease, the internal resistances of the system become more important. This can more accurately be described by (5.1) where R_{int} is the internal resistance of the power supply itself.

$$Q = \frac{V^2}{R_{int} + R} \cdot t \tag{5.1}$$

To determine how this heat dissipates over the volume, *vol*, of the object, we can divide the equation by the volume of the object and rewrite the resistance as a relationship between the material's resistivity, ρ, and its volume shown in (5.2). Here we can see with equal lengths L, internal resistances R_{int}, application times t and applied voltages V, the samples with larger volumes will have proportionally smaller thermal responses, even though their resistance is smaller.

$$\frac{Q}{vol} = \frac{V^2}{\pi r^2 L(R_{int} + \frac{\rho L}{\pi r^2})} \cdot t = \frac{V^2}{\pi r^2 L R_{int} + \rho L^2} \cdot t \tag{5.2}$$

Within the stiffness-variable samples, these thermal responses ranged from 25.0 [$\sigma = 0.0$] to 54.3 [$\sigma = 2.4$] ℃ for the 100 μm samples and 25.0 [$\sigma = 0.0$] to 42.3 [$\sigma = 5.1$] ℃ for the 200 μm samples. In the twisted-coiled samples, narrower values were

observed ranging between 25.0 [$\sigma = 0.0$] to 29.4 [$\sigma = 0.6$] ℃ for the 100 μm samples and 25.0 [$\sigma = 0.0$] to 28.7 [$\sigma = 0.4$] ℃ for the 200 μm samples.

Though the effect of the larger diameter fibre did not play a significant role when uncoated ($t(4) = -1.8562; p = 1.3 \times 10^{-1}$), the introduction of the epoxy coating led to a 12° difference ($t(4) = -3.6727; p = 2.1 \times 10^{-2}$) in the responses of stiffness-variable samples. This alludes to a difference in the interaction between the epoxy and the underlying fibres. In this case, the thicker fibres would have a larger volume left untouched by the epoxy, assuming infiltration was limited in depth on both sample sets. This lower epoxy-fibre ratio is likely the primary contributing factor to this reduced response.

Table 5.5: Mean Temperature-Voltage Rates of 100 μm and 200 μm Carbon Nanotube Stiffness-Variable Samples

Sample Set ($n = 3$)	Diameter (μm)	Response Rate (℃·V^{-1})				
		0.8-1.0 V	1.0-1.2 V	1.2-1.5 V	1.5-1.7 V	1.7-1.9 V
1	100	1.9	35.8	23.2	44.7	29.2
2	200	3.9	11.2	6.4	25.0	36.7

Table 5.6: Mean Temperature-Voltage Rates of 100 μm and 200 μm Carbon Nanotube Twisted-Coiled Samples

Sample Set ($n = 3$)	Diameter (μm)	Response Rate (℃·V^{-1})				
		0.8-1.0 V	1.0-1.2 V	1.2-1.5 V	1.5-1.7 V	1.7-1.9 V
1	100	1.7	2.5	2.9	5.4	7.5
2	200	1.2	1.9	1.9	4.7	7.9

Responses remained non-linear regardless of diameter, and those of the 200 μ samples did exhibit a lower response rate as shown in Tables 5.5 and 5.6. These temperature-voltage rates peaked at the applied voltage of 1.9 V for the 100 μm twisted-coiled, 200 μm stiffness-variable and twisted-coiled sample sets with rates of 7.5, 36.7 and 7.85 ℃ $\cdot V^{-1}$ respectively. For the 100 μm stiffness-variable sample set, peaks occurred at 1.7 V with a rate of 44.65 ℃ $\cdot V^{-1}$. Therefore, a greater voltage stimulus is needed for a comparable thermal response within the 200 μm sample designs. Additional data on the individual sample sets can be found in Appendix D.1.2.

5.1.4 Electromechanical Response

5.1.4.1 Isometric Stress Testing

Similar to the electrothermal results, there was a clear trend between the different diameter stiffness-variable samples regarding their electromechanical responses. Illustrated in Figure 5.2, the 200 μm samples showed a significantly diminished peak contractile response compared to their 100 μm counterparts. In the stiffness-variable samples, this is expressed by an ≈7.26 fold decrease ($t(4) = -23.6986; p = 1.9 \times 10^{-5}$) in the contractile stress, a shift from a mean range of 5.01 to 29.11 MPa in the 100 μm samples to 0.92 to 4.01 MPa in the 200 μm samples. Similarly in the twisted-coiled precursors, there was an ≈4.69 fold decrease ($t(4) = -47.6365; p = 1.2 \times 10^{-6}$) with a mean range of 8.15 to 33.46 MPa and 1.68 to 7.14 MPa in the 100 μm and 200 μm samples respectively. Tables 5.7 and 5.8 show the complete set of isometric data.

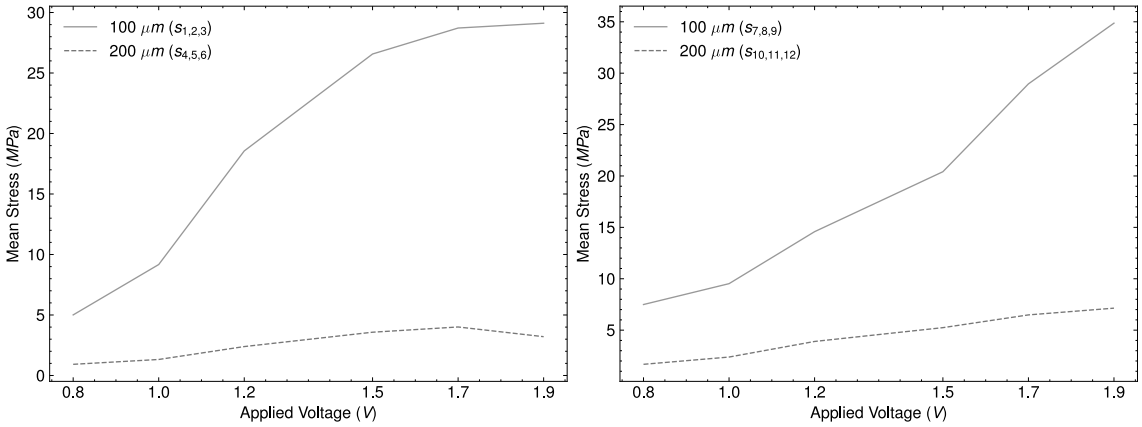

(a) **(b)**

Figure 5.2: Mean contractile engineering stress vs applied voltage for the fabricated (a) stiffness-variable and (b) twisted-coiled samples sets.

Table 5.7: Mean Contractile Engineering Stress vs Applied Voltage of Stiffness-Variable Samples with 20% Pre-stretch using 100 μm and 200 μm Carbon Nanotube Fibre/Yarn

Sample Set ($n = 3$)	Diameter (μm)	Contractile Stress (MPa) [σ]					
		0.8 V	1.0 V	1.2 V	1.5 V	1.7 V	1.9 V
1	100	5.01 [0.90]	9.17 [1.35]	18.56 [0.71]	26.57 [3.35]	28.72 [1.54]	29.11 [1.86]
2	200	0.92 [0.11]	1.32 [0.24]	2.39 [0.16]	3.58 [0.43]	4.01 [0.32]	3.21 [0.37]

These stark differences could be attributed to the balance between the mechanical stiffness of the fibre and the electromagnetic forces driving the actuation. However,

Table 5.8: Mean Contractile Engineering Stress vs Applied Voltage of Twisted-Coiled Samples with 20% Pre-stretch using 100 μm and 200 μm Carbon Nanotube Fibre/Yarn

Sample Set ($n = 3$)	Diameter (μm)	Contractile Stress (MPa) [σ]					
		0.8 V	1.0 V	1.2 V	1.5 V	1.7 V	1.9 V
1	100	7.49 [2.04]	9.52 [2.93]	14.58 [4.65]	20.41 [3.62]	28.96 [6.36]	34.87 [0.88]
2	200	1.68 [0.38]	2.39 [0.11]	3.90 [0.70]	5.24 [0.30]	6.48 [1.03]	7.14 [0.50]

preliminary tests show that the stiffness of the thicker samples, even in their coated forms, remained significantly smaller than the thinner samples. Furthermore, while the reduced thermal responses previously shown in Section 4.1.3 might play a role in the stiffness-variable samples, the contractile stress performance gap remained significant in the twisted-coiled counterparts as well. One key structural difference between these two products is their underlying composition, where the 100 μm material is a single filament fibre without twist, while the 200 μm material is a twisted yarn presumably composed of multiple 100 μm fibres. The manufacturer does not mention how these samples were twisted either, which has been shown to be a crucial parameter in enhancing or depressing the contractile responses in various CNT fibre actuator designs. More information would be needed to determine if this is the underlying cause for the poor responses and how it could be modified to mitigate them.

Beyond their magnitudes, the response rates of the stiffness-variable samples show a consistent activation point around 1-1.2 V where the thermal energy was sufficient to reduce the epoxy stiffness. This is echoed in the thermal response results where the largest temperature-voltage rates occurred between 1-1.7 V. The twisted-coiled samples do not have this resistive property due to the lack of epoxy and thus experienced a traditional exponential increase as the applied voltage increased. Additionally, the reduced stiffness within the twisted-coiled samples, as shown in Section 4.1.1 and Tables 5.3 and 5.4, allowed for larger maximum contractile stresses 33.46 MPa compared to 29.11 MPa in the 100 μm samples and 7.14 MPa compared to 4.01 MPa in the 200 μm samples.

Post-actuation stress relaxation, shown in Figure 5.3, was also affected by the difference in core diameter. Stiffness-variable actuator samples with the 200 μm core experienced a noticeable decrease in stress relaxation occurrences and actually exhibited stress increases throughout the testing cycles. These conflicting shifts acted to balance out within consecutive cycles resulting in an insignificant difference throughout ($t(4) = -1.2468; p = 2.8 \times 10^{-1}$). Without the additional resistance from the epoxy, the same behaviour was significantly ($t(4) = -4.9196; p = 7.9 \times 10^{-3}$) exaggerated within the twisted-coiled samples, emphasizing the reduced loss within the thicker diameter samples.

While the increased contractile stress results paint the twisted-coiled samples as superior actuators, the additional losses during consecutive actuation cycles and the reliance on an external load can be a significant disadvantage depending on the application.

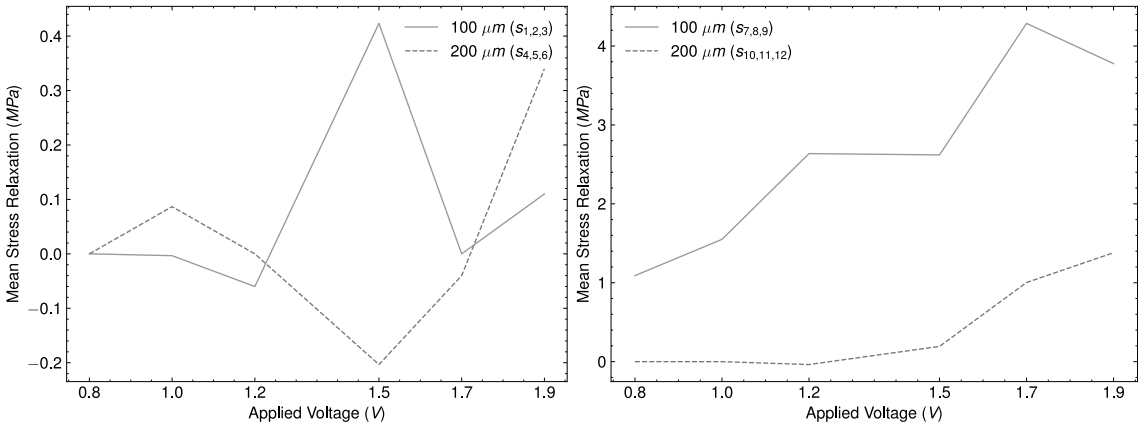

(a) **(b)**

Figure 5.3: Mean stress relaxation after an actuation cycle at consecutive voltage intervals during isometric test cycles for (a) stiffness-variable and (b) twisted-coiled actuator sample sets.

5.1.4.2 Isotonic Strain Testing

The diameter of the fibre/yarn significantly ($t(4) = -29.7143; p = 7.6 \times 10^{-6}$) decreased the resulting contractile strains of the stiffness-variable samples. Those from the 200 μm were 82% smaller at their peaks compared to their 100 μm counterparts, with 0.15 [$\sigma = 0.02$]% and 0.84 [$\sigma = 0.03$]%, respectively as indicated in Table 5.9. Similarly, strain-voltage rates were reduced by 74% at their peaks, with maximum rates of $0.4\% \cdot V$ and $1.55\% \cdot V$, respectively. Conversely, when the fibre was left uncoated in the twisted-coiled samples, the maximum contractile strain and strain rate remained almost equal ($t(4) = 1.3684; p = 2.4 \times 10^{-1}$), regardless of the fibre/yarn diameter when accounting for the standard deviation highlighted in Table 5.10.

Table 5.9: Mean Contractile Engineering Strain vs Applied Voltage of Stiffness-Variable Samples with 20% Pre-stretch using 100 μm and 200 μm Carbon Nanotube Fibre/Yarn

Sample Set ($n = 3$)	Diameter (μm)	Contractile Strain (%) [σ]					
		0.8 V	1.0 V	1.2 V	1.5 V	1.7 V	1.9 V
1	100	0.02 [0.04]	0.08 [0.10]	0.25 [0.08]	0.31 [0.06]	0.53 [0.08]	0.84 [0.03]
2	200	0.01 [0.02]	0.01 [0.02]	0.0 [0.00]	0.02 [0.03]	0.07 [0.02]	0.15 [0.02]

Table 5.10: Mean Contractile Engineering Strain vs Applied Voltage of Twisted-Coiled Samples with 20% Pre-stretch using 100 μm and 200 μm Carbon Nanotube Fibre/Yarn

Sample Set ($n = 3$)	Diameter (μm)	Contractile Strain (%) [σ]					
		0.8 V	1.0 V	1.2 V	1.5 V	1.7 V	1.9 V
1	100	0.00 [0.00]	0.04 [0.07]	0.10 [0.07]	0.13 [0.10]	0.29 [0.11]	0.33 [0.07]
2	200	0.04 [0.04]	0.15 [0.14]	0.17 [0.05]	0.26 [0.03]	0.30 [0.11]	0.42 [0.09]

The addition of the epoxy coating, particularly to samples using a larger fibre/yarn diameter, resulted in significant resistance to movement when stimulated. While higher voltages do reduce this resistance (see Figure 5.4(a) 200 μm 1.5-1.9 V), it is unknown whether this is the determining factor compared to the geometry of the material itself mentioned previously. Further investigations should look into the response of these thicker yarns/fibres at much larger voltages to see if the trend increases, in addition to the effects of their geometry.

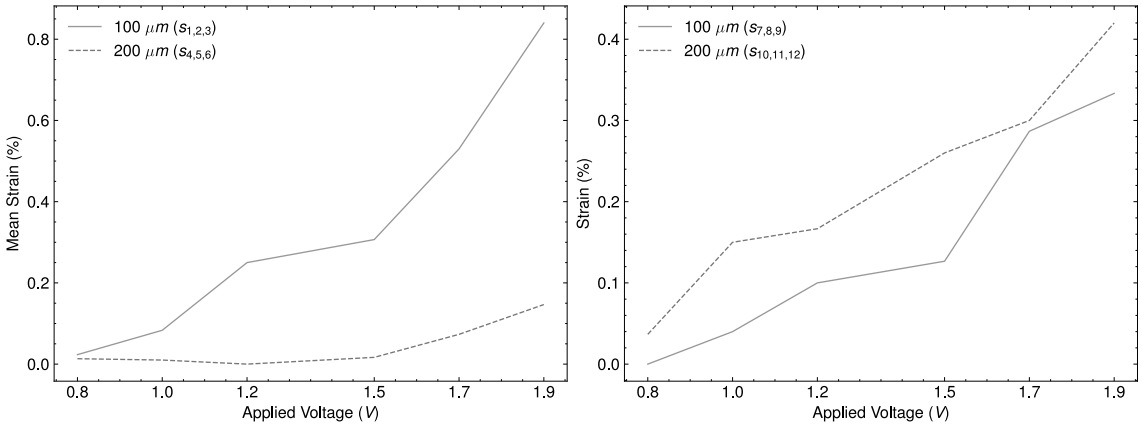

(a) **(b)**

Figure 5.4: Mean contractile engineering strain vs applied voltage for the fabricated (a) stiffness-variable and (b) twisted-coiled sample sets.

5.2 Effects due to Pre-stretch Percentage

5.2.1 Fabrication Procedure and Sample Descriptions

The second parameter investigated was the amount of pre-stretch introduced into the actuator design during the fabrication process. For this parameter, two samples were made for each of the four pre-stretch percentages, 10%, 15%, 20%, and

25%. using the standard fabrication process outlined in Section 3.2.2. For the comparison twisted-coiled samples, three were fabricated using a similar process, with pre-stretches facilitated through the Biotester. These samples' fabrication properties are summarized in tables below.

Table 5.11: Fabrication Properties of 100 μm Carbon Nanotube Stiffness-Variable Samples with Selected Pre-stretch

Sample	Length (cm)		Pre-stretch (%)	MD (μm)	SI	T_{tot}	T_c	$\Omega \cdot cm^{-1}$
	Initial	Final						
s_1	2.25	1.32	8.47	103.36	1.03	36.49	23.14	0.3607
s_2	3.51	1.56	11.14	117.36	1.17	37.35	17.68	0.5978
s_3	2.70	1.08	15.91	116.15	1.16	38.15	20.00	0.3479
s_4	2.53	1.02	15.26	116.15	1.16	39.11	19.36	0.5693
s_5	2.43	1.35	19.64	69.44	0.69	41.20	23.90	0.3195
s_6	2.46	1.06	18.95	92.00	0.92	40.22	20.31	0.3389
s_7	2.74	1.26	24.74	109.03	1.09	30.61	21.13	0.4587
s_8	2.78	1.27	24.74	93.06	0.93	38.11	20.49	0.5058

Table 5.12: Fabrication Properties of 100 μm Carbon Nanotube Twisted-Coiled Samples with Selected Stretch

Sample	Length (cm)		Pre-stretch (%)	MD (μm)	SI	T_{tot}	T_c	$\Omega \cdot cm^{-1}$
	Initial	Final						
s_{9a}	3.25	1.27	10.31	99.31	0.99	40.62	21.85	0.3966
s_{9b}	3.25	1.33	15.70	99.31	0.99	40.62	21.85	0.4080
s_{9c}	3.25	1.39	20.63	99.31	0.99	40.62	21.85	0.4175
s_{9d}	3.25	1.45	25.41	99.31	0.99	40.62	21.85	0.4311
s_{10a}	1.92	0.75	10.31	101.56	1.02	44.39	20.89	0.4841
s_{10b}	1.92	0.78	15.70	101.56	1.02	44.39	20.89	0.4862
s_{10c}	1.92	0.81	20.63	101.56	1.02	44.39	20.89	0.4992
s_{10d}	1.92	0.84	25.41	101.56	1.02	44.39	20.89	0.5070
s_{11a}	2.72	1.05	10.55	115.10	1.15	37.84	18.00	0.5397
s_{11b}	2.72	1.09	14.91	115.10	1.15	37.84	18.00	0.5452
s_{11c}	2.72	1.14	20.00	115.10	1.15	37.84	18.00	0.5500
s_{11d}	2.72	1.19	25.45	115.10	1.15	37.84	18.00	0.5540

5.2.2 Electrical Properties

The resistance measured for the fabricated stiffness-variable actuators showed inconsistent changes in magnitude as the stretch increased, which is misleading. As determined in section 4.1.2, the primary driver for the resistance within a stiffness-variable sample is the variable connection resistance between the CNT and the pa-

perclip. Without ensuring the quality of the connection, this limitation diminishes the ability to determine any small resistance trends between fabricated samples, especially with such minute differences when stretch is introduced.

A better indicator of the resistance trends due to stretching was looking at the stretched twisted-coiled samples s_9, s_{10}, and s_{11}. The values measured consistently increased as the amount of stretch increased, as shown in Figure 5.5. In these three samples, the average rate of increase was 2.82%, 1.56% and 0.88%, respectively, per 5% stretch interval. These results align with the previous trend in Section 4.1.2 where the resistance increased as the stretch rose from 0-15%, however the magnitudes are not statically significant and would require additional samples to validate this observation adequately.

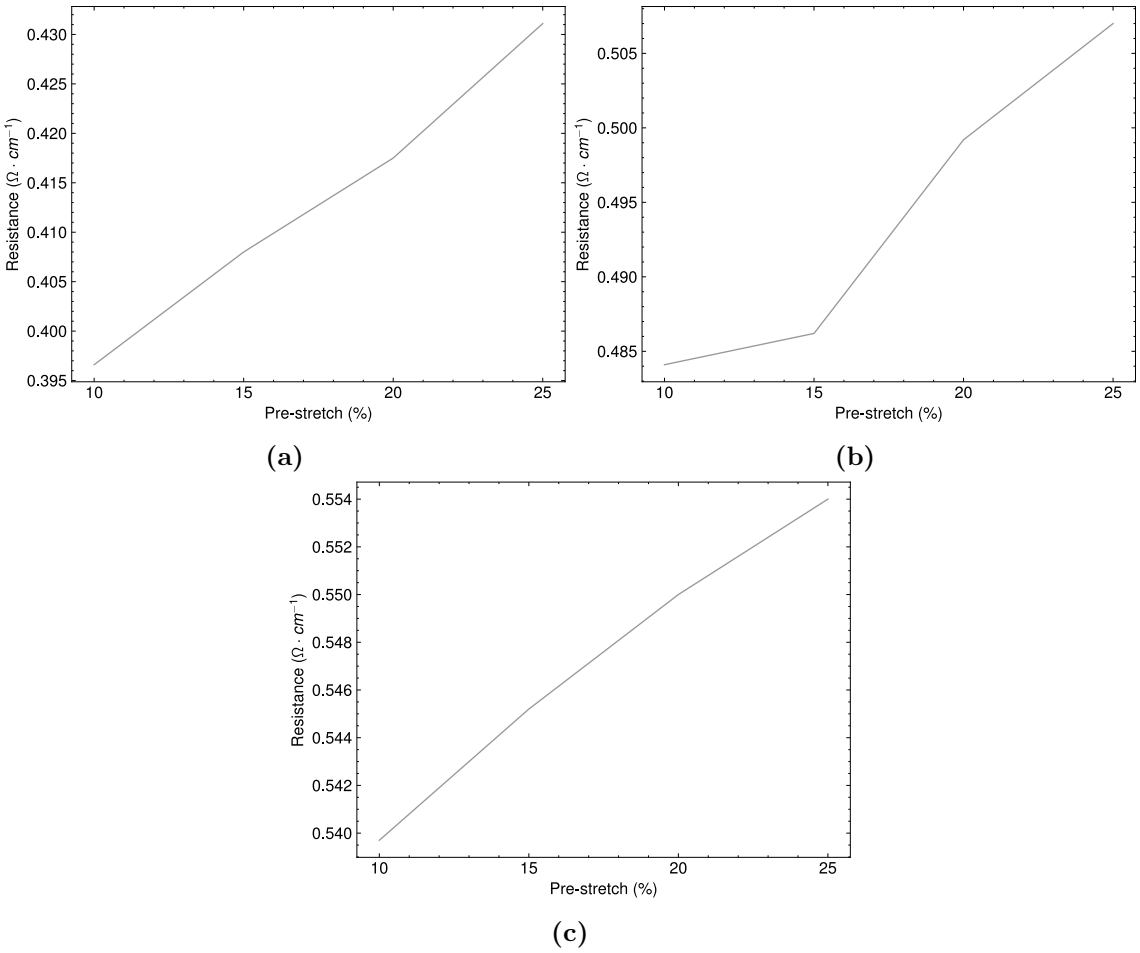

Figure 5.5: Resistance vs pre-stretch percentage for samples (a) s_9, (b) s_{10}, and (c) s_{11}.

5.2.3 Electrothermal Response

When increasing the pre-stretch percentage, the thermal response rate within the stiffness-variable samples marginally increased as seen in Figure 5.6, though only significantly between 15% and 20% ($t(2) = 4.4444; p = 4.7 \times 10^{-2}$). These increases were exponential as a function of voltage and required a sufficient applied voltage step of $\approx$1.2 V to have any significant change. While this increasing shift in the responses appeared for pre-stretches of 10-20%, the 25% samples experienced a slightly lower response than that at 20%, it was largely insignificant with a difference within 2℃ at its peak. As a driving factor for the thermal responses, the epoxy was able to access a greater amount of the fibre's surface area as the space between the fibre coils increased, explaining the increase in response as the pre-stretch percentage rose.

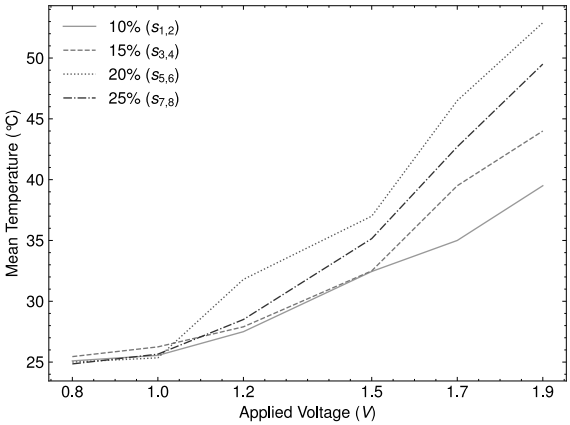

Figure 5.6: Mean temperature vs applied voltage for the fabricated stiffness-variable sample sets with 10%, 15%, 20%, and 25% pre-stretch.

The thermal responses of the twisted-coiled samples, shown in Figure 5.7, appeared to increase with the pre-stretch, though the magnitude of that variation was much less consistent and remained statistically insignificant. Additionally, their peak values were not as affected by the pre-stretch variation, as shown by their convergence to a mean peak of $\approx$30 ℃ at 1.9 V, compared to the stiffness-variable samples whose mean peaks ranged from 39.5 [$\sigma = 7.8$] to 52.9 [$\sigma = 0.1$] ℃.

This difference in overall peak value and their overall range is similar to results obtained previously when looking at the coated and non-coated designs in Section 4.1.3. Here, the twisted-coiled samples has a $\approx$25-31℃ peak range, compared to the $\approx$25-53℃ of the stiffness-variable samples.

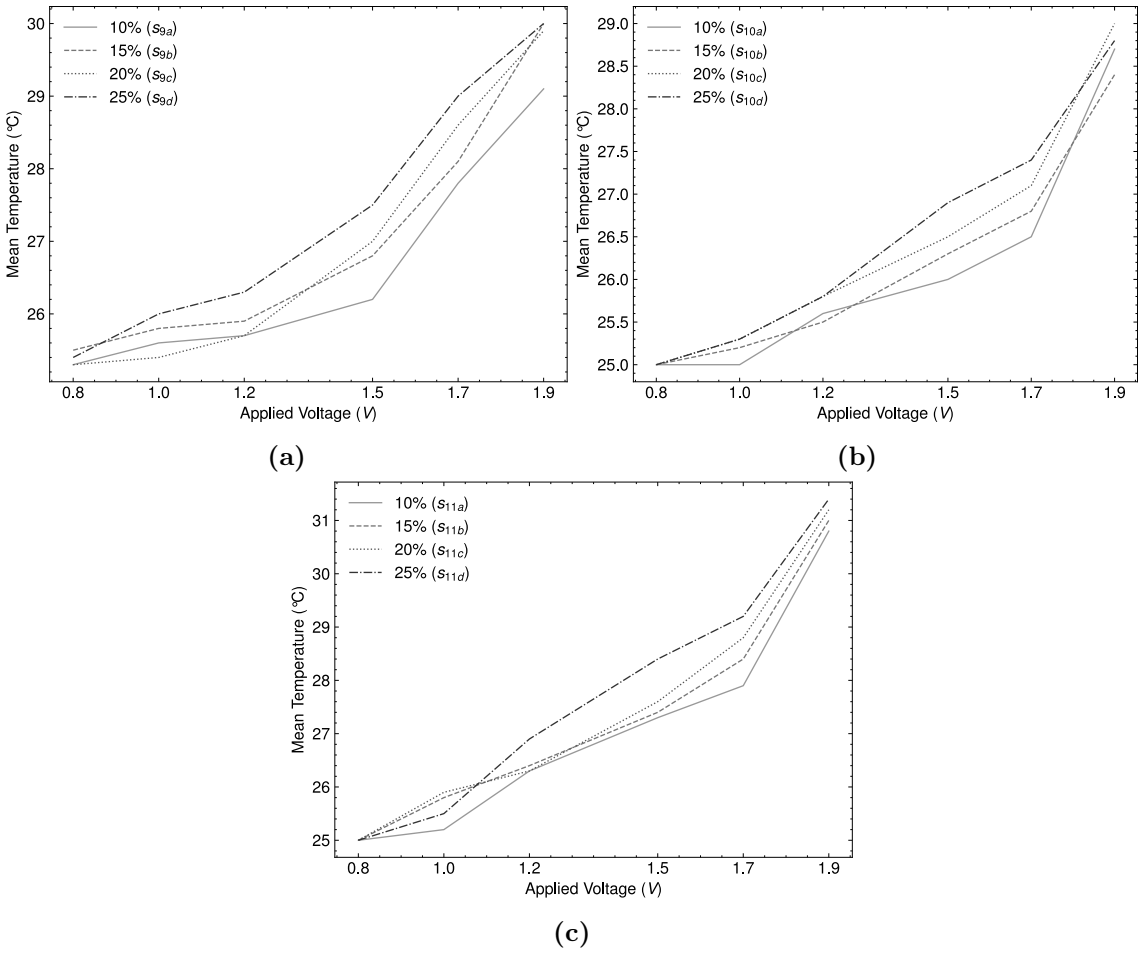

Figure 5.7: Electrothermal responses of twisted-coiled samples (a) s_9, (b) s_{10}, and (c) s_{11} with 10%, 15%, 20% and 25% pre-stretch.

5.2.4 Electromechanical Response

5.2.4.1 Isometric Stress Testing

Increasing the pre-stretch percentages in the stiffness-variable samples resulted in increased activation voltages highlighted in Figure 5.8. This effect was more pronounced with higher pre-stretches seen in the 20% samples where the response from 1-1.7 V had a more logarithmic shape than the exponential shape in the 10% and 15% samples. The diffrentiation was evident particular around 1.5 V, with the 20% sample response reaching 13.22 MPa magnitude larger than the 10% samples ($t(2) = 9.1294; p = 1.2 \times 10^{-2}$), and 6.91 MPa larger than the 15% samples ($t(2) = 5.4906; p = 3.2 \times 10^{-2}$). Generally, the peak contractile stresses tended to

increase along these lines as well, with the 20% samples reaching the highest mean value of 28.46 [$\sigma = 2.07$] *MPa*, followed by 15% at 27.24 [$\sigma = 1.99$] *MPa*, 10% at 20.1 [$\sigma = 2.02$] *MPa* and 25% at 16.01 [$\sigma = 1.57$] *MPa*.

Interestingly, the 25% samples showed a significant ($t(2) = -6.7709; p = 2.1 \times 10^{-2}$) diminished peak response compared to the 20% samples owing to their loss of tension once initially actuated. The initial stimulation of the samples reduced the stiffness of the epoxy enough to allow the internal fibre tension to equalize at a smaller value before cooling, as highlighted in the measured post actuation stress relaxation across testing cycles in Figure 5.9, resulting in smaller contractions when tested. It should also be noted the opposite behaviour affected the lower pre-strech samples, with increasing stress relaxation for the 20%, 15%, and 10% samples sets.

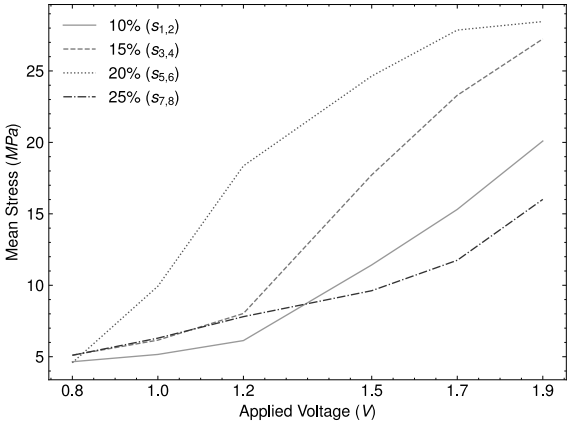

Figure 5.8: Mean contractile engineering stress vs applied voltage for the fabricated stiffness-variable sample sets with 10%, 15%, 20%, and 25% pre-stretch.

Table 5.13: Mean Contractile Engineering Stress vs Applied Voltage of Stiffness-Variable Samples with Selected Pre-stretch

Sample Set ($n = 2$)	Pre-stretch (%)	Contractile Stress (MPa) [σ]					
		0.8 V	1.0 V	1.2 V	1.5 V	1.7 V	1.9 V
1	10	4.65 [0.45]	5.16 [0.27]	6.13 [0.16]	11.42 [2.03]	15.31 [2.66]	20.10 [2.02]
2	15	5.11 [0.51]	6.16 [0.30]	8.02 [1.08]	17.73 [1.76]	23.30 [1.63]	27.24 [1.99]
3	20	4.58 [0.72]	9.93 [0.36]	18.35 [0.87]	24.64 [0.27]	27.86 [0.58]	28.46 [2.07]
4	25	5.10 [0.28]	6.30 [0.59]	7.80 [0.21]	9.62 [0.49]	11.75 [0.21]	16.01 [1.57]

The twisted-coiled samples, shown in Figure 5.10, had a distinct shift in contractile stresses as the pre-stretch increased. Compared to the stiffness-variable samples, the max stresses measured were much larger with a peak mean of 44.34 *MPa* compared to 28.45 *MPa* ($t(3) = 4.1807; p = 2.5 \times 10^{-2}$) owing to the lack of resistance due to the epoxy guest material. Additionally, since these samples were held at their tested pre-stretch percentage, the loss of tension never occurred in the 25% samples,

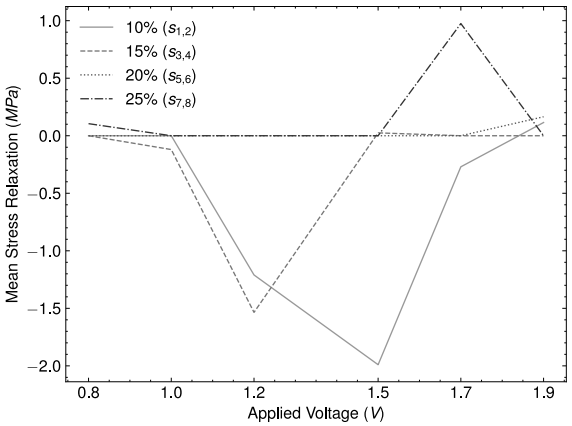

Figure 5.9: Mean stress relaxation after an actuation cycle at consecutive voltage intervals during isometric test cycles for stiffness-variable sample sets with 10%, 15%, 20%, and 25% pre-stretch.

as indicated in Figure 5.11, instead displaying an increasing stress relaxation after each actuation cycle with increasing pre-stretch percentages.

5.2.4.2 Isotonic Strain Testing

Contractile strains for the stiffness-variable samples were also found to increase with pre-stretch percentage and at an increasing rate with the voltage applied. Peak values were measured in the 20% samples at 0.85 [$\sigma = 0.04$], followed by the 15% at 0.65 [$\sigma = 0.16$]%, 25% at 0.56 [$\sigma = 0.01$] and 10% at 0.40 [$\sigma = 0.08$]%. The largest consecutive differences were seen between 10%-15% pre-stretched samples, a jump of ≈63%. The 15% and 25% samples showed similar responses at their peak, though they deviated when stimulated with 1.2-1.5 V. Finally, the 25% samples performed poorly for similar reasons as those outlined in the isometric tests, resulting in contractile strains only larger than their 10% pre-stretched counterparts by 40%, and significantly ($t(2) = -9.1706; p = 1.2 \times 10^{-2}$) lower than the 20% samples. Though these increasing trends are observed and significant for larger pre-stretch changes such as 10% to 20% ($t(2) = -7.2626; p = 1.8 \times 10^{-2}$), the significance of the incremental changes could not be validated through the limited number of samples available.

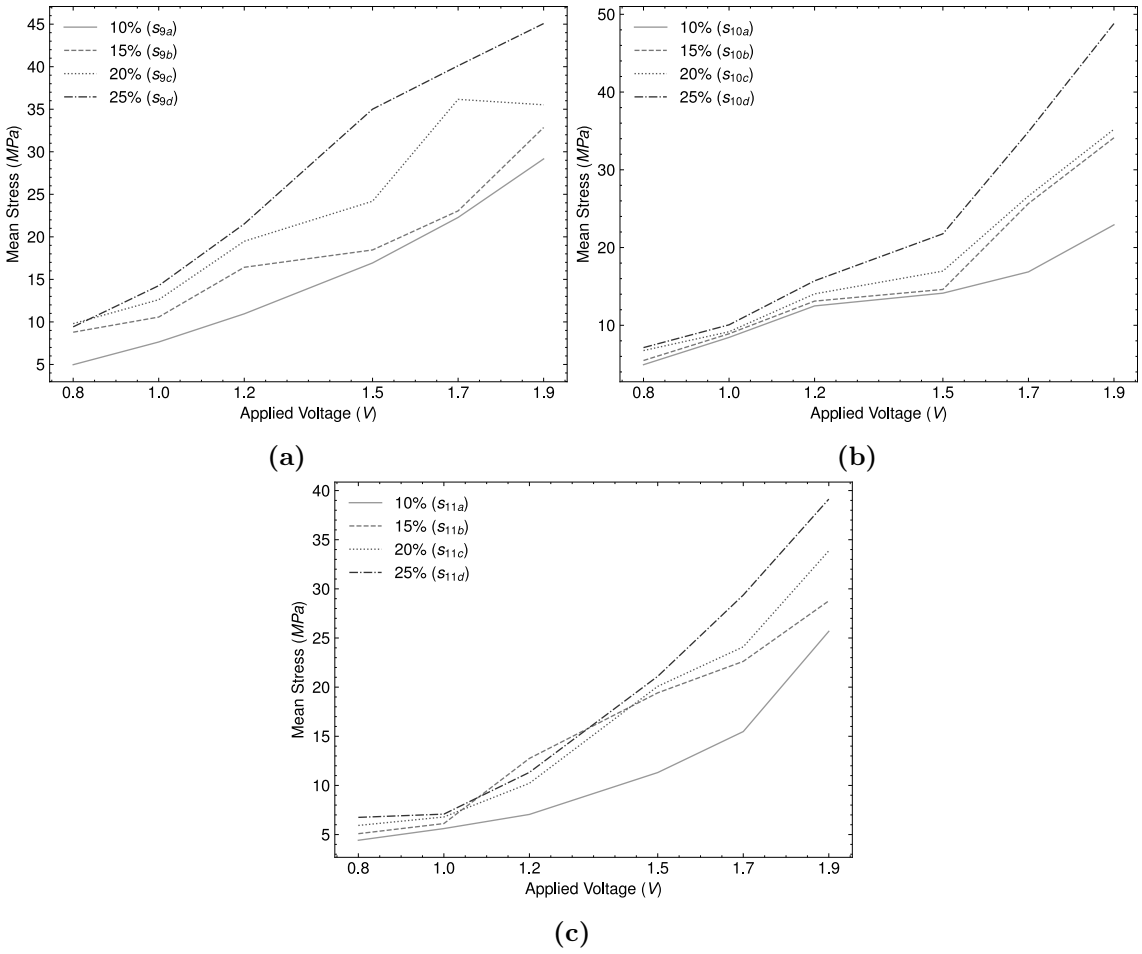

Figure 5.10: Mean contractile engineering stress vs applied voltage of twisted-coiled samples (a) s_9, (b) s_{10} and (c) s_{11} with 10%, 15%, 20% and 25% pre-stretch.

Table 5.14: Mean Contractile Engineering Strain vs Applied Voltage of Stiffness-Variable Samples with Selected Pre-Stretch

Sample Set ($n = 2$)	Pre-stretch (%)	Contractile Strain (%) [σ]					
		0.8 V	1.0 V	1.2 V	1.5 V	1.7 V	1.9 V
1	10	0.00 [0.00]	0.02 [0.03]	0.02 [0.03]	0.09 [0.01]	0.15 [0.03]	0.40 [0.08]
2	15	0.04 [0.01]	0.05 [0.03]	0.19 [0.01]	0.38 [0.19]	0.38 [0.04]	0.60 [0.09]
3	20	0.04 [0.05]	0.12 [0.11]	0.30 [0.01]	0.34 [0.04]	0.52 [0.11]	0.85 [0.04]
4	25	0.00 [0.00]	0.00 [0.00]	0.05 [0.06]	0.18 [0.06]	0.32 [0.13]	0.56 [0.01]

5.3 Effects due to Coating Application Interval

5.3.1 Fabrication Procedure and Sample Descriptions

As an integral part of the stiffness-variable design, determining the extent to which the coating affects the eventual performance is essential. Thus, the third parameter

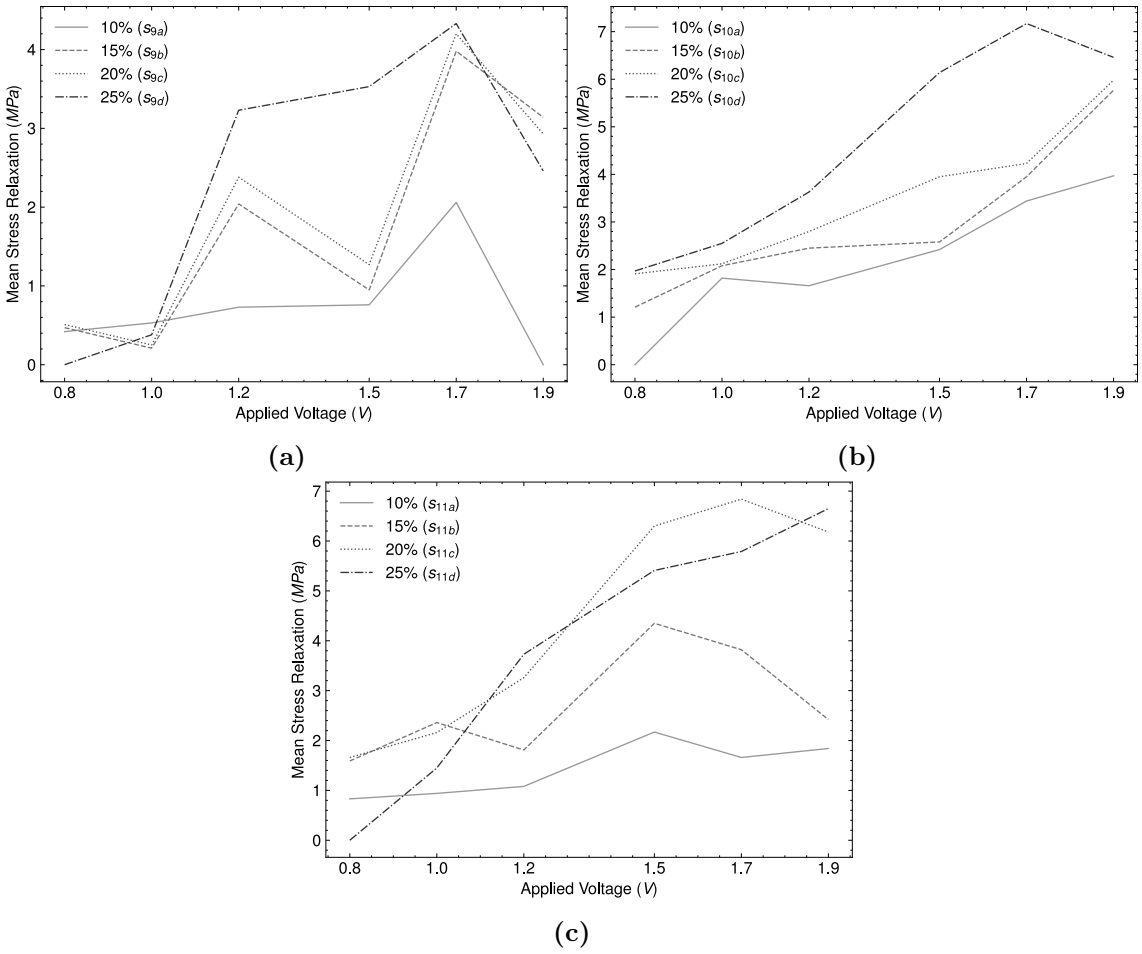

Figure 5.11: Mean stress relaxation after an actuation cycle at consecutive voltage intervals during isometric test cycles for the twisted-coiled samples (a) s_9, (b) s_{10}, and (c) s_{11} with 10%, 15%, 20% and 25% pre-stretch.

evaluated was explicitly how the interval between coating applications affected the resulting actuator. Three samples were fabricated with three coating application intervals, the first using the 10 *min* interval previously described in Table 3.2.2, and the second and third using an application interval of 20 *min* and 30 *min*. These intervals roughly corresponded to coating thicknesses of 60 μm, 125 μm and 110 μm, respectively. The additional time between applications made the epoxy more viscous with each successive application, resulting in a thicker and more even coating on the CNT fibre. This was evident by the reduced occurrence of epoxy globs, which happened when the epoxy settled unevenly on the sample during the curing window. These fabricated samples' base properties are summarized in Tables 5.15 to 5.17. Since this parameter depends on the epoxy coating, uncoated twisted-coiled samples were excluded from the investigation.

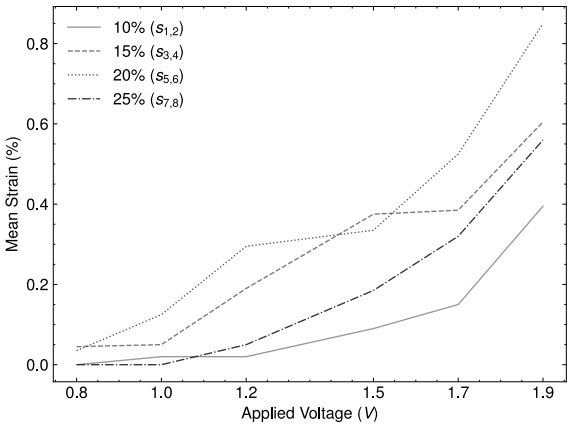

Figure 5.12: Mean contractile engineering strain vs applied voltage for the fabricated stiffness-variable sample sets s_1 and s_2 (10%), s_3 and s_4 (15%), s_5 and s_6 (20%), and s_7 and s_8 (25%)

Table 5.15: Fabrication Properties of 100 μm Carbon Nanotube Stiffness-Variable Samples with a 10 *min* Coating Application Interval

Sample	Length (cm)		Pre-stretch (%)	MD (μm)	SI	T_{tot}	T_c	$\Omega \cdot cm^{-1}$
	Initial	Final						
s_1	2.68	1.15	15.25	99.23	0.99	34.02	18.69	0.3884
s_2	2.70	1.08	15.91	116.15	1.16	38.15	20.00	0.3479
s_3	2.53	1.02	15.26	116.15	1.16	39.11	19.36	0.5693

Table 5.16: Fabrication Properties of 100 μm Carbon Nanotube Stiffness-Variable Samples with 20 *min* Coating Application Interval

Sample	Length (cm)		Pre-stretch (%)	MD (μm)	SI	T_{tot}	T_c	$\Omega \cdot cm^{-1}$
	Initial	Final						
s_4	2.50	1.04	14.69	73.64	0.74	39.65	21.23	0.3364
s_5	2.43	1.08	14.84	87.04	0.87	39.94	20.18	0.3309
s_6	1.86	0.65	14.88	92.78	0.93	41.89	20.41	0.4070

Table 5.17: Fabrication Properties of 100 μm Carbon Nanotube Stiffness-Variable Samples with 30 *min* Coating Application Interval

Sample	Length (cm)		Pre-stretch (%)	MD (μm)	SI	T_{tot}	T_c	$\Omega \cdot cm^{-1}$
	Initial	Final						
s_7	3.45	1.42	15.36	106.60	1.07	37.73	20.32	0.4156
s_8	2.64	1.09	16.30	99.65	1.00	39.07	21.62	0.3420
s_9	3.13	1.30	15.56	109.20	1.09	36.69	20.74	0.2745

5.3.2 Electrical Properties

The increase in application interval had no discernible effect on the resistances of the three sample sets. The 10 *min*, 20 *min* and 30 *min* coating interval sample sets reported mean resistances of 0.3682 $\Omega \cdot cm^{-1}$, 0.3581 $\Omega \cdot cm^{-1}$ and 0.3440 $\Omega \cdot cm^{-1}$ respectively, a relatively insignificant ($t(4) = -1.1493; p = 3.1 \times 10^{-1}$) difference among the range of coating intervals. This relationship reaffirms the results previously observed in Section 4.1.2, where the presence of the coating did not increase the sample's electrical resistance due to the primary path of electron travel, the fibre, not being interrupted by the epoxy guest material.

5.3.3 Electrothermal Response

Illustrated in Table 5.18, the 20 *min* coating application interval appeared to increase the sample's thermal retention, resulting in an increased surface temperature over successive actuation cycles. These samples expressed peak response rates of 43.4 compared to the 33.4 ℃$\cdot V^{-1}$ of the 10 *min* samples at the 1.5-1.7 *V* interval. Additionally, while the activation voltages remained around ≈1.2 *V*, the samples with the 20 *min* coating application interval also displayed a significant, ($t(4) = 4.5227; p = 1.1 \times 10^{-2}$), 10 ℃ increase in their peak thermal responses, reaching 55.7 [$\sigma = 1.5$] ℃ as shown in Figure 5.13. Interestingly, the 30 *min* samples showed a comparatively significant ($t(4) = -3.4066; p = 2.7 \times 10^{-2}$) depressed response, with a peak thermal response of 38.7 [$\sigma = 0.6$] ℃ and a peak response rate of 20.0 ℃$\cdot V^{-1}$ at the 1.7-1.9 *V* interval. This shift could be caused by several factors, such as the reduced absorption of the more viscous epoxy, which would reduce the contact surface area between the CNT fibre and the epoxy, however further tests would be required to validate this interaction.

Table 5.18: Mean Temperature-Voltage Rates of Selected Coating Application Intervals

Sample Set ($n = 3$)	Interval (min)	Response Rate (℃$\cdot V^{-1}$)				
		0.8-1.0 *V*	1.0-1.2 *V*	1.2-1.5 *V*	1.5-1.7 *V*	1.7-1.9 *V*
1	10	3.5	9.7	20.2	33.4	25.0
2	20	2.9	13.3	35.6	43.4	40.0
3	30	6.4	8.0	8.1	18.6	20.0

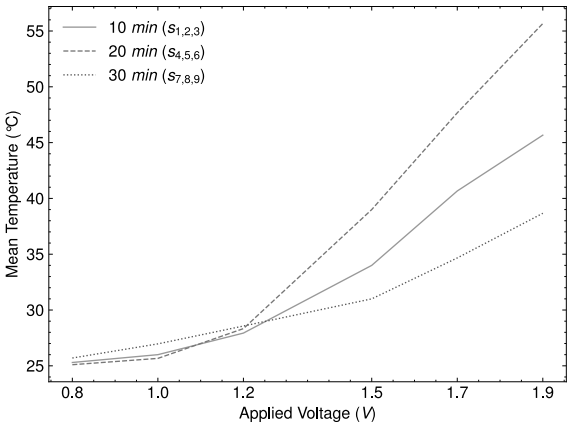

Figure 5.13: Mean temperature vs applied voltage for the fabricated stiffness-variable samples using the 10 *min*, 20 *min* and 30 *min* coating application intervals.

5.3.4 Electromechanical Response

5.3.4.1 Isometric Stress Testing

The extended application intervals reduced the peak contractile engineering stress of the actuator significantly, as illustrated in Figure 5.14. For the 20 and 30 *min* samples, this was a drop of 23% ($t(4) = -5.6129; p = 4.9 \times 10^{-3}$) to 20.63 [$\sigma = 1.13$] MPa and 54.3% ($t(4) = -6.4965; p = 2.9 \times 10^{-3}$) to 12.27 [$\sigma = 3.57$] MPa respectively, compared to the 26.86 MPa peak of the 10 *min* samples. Similarly, stress-voltage rates shown in Table 5.20, particularly at higher voltages, dropped from a peak of 29.90 $MPa \cdot V^{-1}$ seen in the 10 *min* samples to 23.63 and 21.2 $MPa \cdot V^{-1}$ in the 20 and 30 *min* sample sets. This can be seen as an exaggerated effect previously seen when comparing the differences between coated and uncoated samples. These samples would have an increase in stiffness compared to their less coated counterparts which acts to reduce the effective actuation when stimulated.

Table 5.19: Mean Contractile Engineering Stress vs Voltage of 100 μm Carbon Nanotube Stiffness-Variable Samples with Selected Coating Application Intervals

Sample Set ($n = 3$)	Interval (min)	Contractile Stress (MPa)					
		0.8 V	1.0 V	1.2 V	1.5 V	1.7 V	1.9 V
1	10	5.10 [0.36]	6.02 [0.33]	7.73 [0.92]	16.70 [2.17]	22.36 [1.98]	26.86 [1.56]
2	20	4.42 [0.45]	5.18 [0.15]	7.60 [1.08]	14.69 [1.04]	16.98 [1.59]	20.63 [1.13]
3	30	0.00 [0.00]	1.27 [1.28]	3.31 [1.29]	5.21 [2.23]	8.03 [3.85]	12.27 [3.57]

On the other hand, the stress relaxation trend was less clear, as seen in Figure 5.15. The relaxations remained below zero in all samples tested, indicating

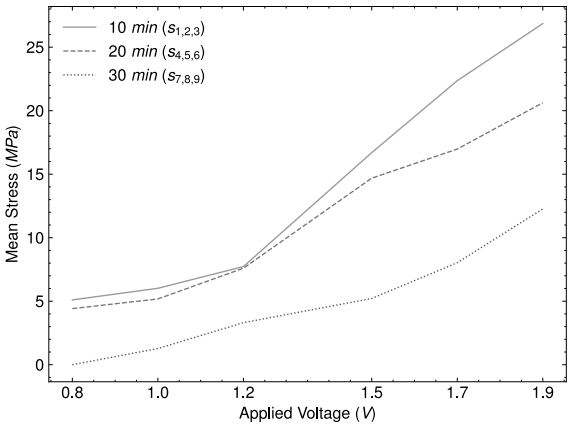

Figure 5.14: Mean contractile engineering stress vs applied voltage for the fabricated stiffness-variable samples using the 10 *min*, 20 *min* and 30 *min* coating application intervals.

Table 5.20: Mean Contractile Engineering Stress-Voltage Rates of 100 μm Carbon Nanotube Stiffness-Variable Samples with Selected Coating Application Intervals

Sample Set ($n = 3$)	Interval (min)	Response Rate ($MPa \cdot V^{-1}$)				
		0.8-1.0 V	1.0-1.2 V	1.2-1.5 V	1.5-1.7 V	1.7-1.9 V
1	10	4.60	8.55	29.90	28.30	22.50
2	20	3.80	12.10	23.63	11.45	18.25
3	30	6.35	10.20	6.33	14.10	21.20

increased tension throughout the tests. Furthermore, though this tension increased most drastically with the lowest interval samples, the 30 *min* samples showed a moderate though not significant ($t(4) = 1.0558; p = 3.5 \times 10^{-1}$) relaxation decrease of -0.52 *MPa* compared to only -0.19 *MPa* of the 20 *min* samples, at the activation voltage of $1.2\,V$. The decreased relaxation in 30 *min* samples was also partially present in higher applied voltages, not seen in the other two sample sets.

Additionally, while the 20 *min* samples reached higher temperatures due to the thermal retention of the epoxy, it appeared to have a minimal effect on their actuating response, either due to this increased stiffness or an uneven temperature distribution throughout the sample.

The difference in these behaviours could point to a change in the relationship at the boundary layer of the epoxy and the underlying CNT fibre. This shift would lean more towards a "sheathed" design with a smaller volume of the infiltration layer th_{gi} described in Figure 2.6. Such a change could result in differences in the mechanical properties and thermal distribution, reducing the contractile responses. Further material tests would be required to confirm this hypothesis.

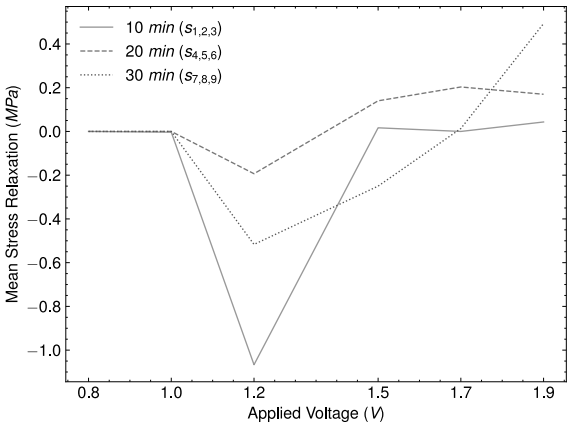

Figure 5.15: Mean stress relaxation after an actuation cycle at consecutive voltage intervals during isometric test cycles for the stiffness-variable samples using the 10 *min*, 20 *min* and 30 *min* coating application intervals.

5.3.4.2 Isotonic Strain Testing

The contractile strains also showed optimal behaviour at the 20 *min* interval, having the largest peak of 0.72 $[\sigma = 0.02]\%$ compared to 0.54 $[\sigma = 0.11]\%$ ($t(4) = -2.623; p = 5.9 \times 10^{-2}$) and 0.41 $[\sigma = 0.03]\%$ ($t(4) = -6.0399; p = 3.7 \times 10^{-3}$) in the 10 and 30 *min* sample sets. The differences within these responses occurred most significantly around the 1.5 V applied voltage, with a slight depression seen in the 30 *min* samples at 1.2 V, as outlined in Table 5.21.

Table 5.21: Mean Contractile Engineering Strain vs Voltage of 100 μm Carbon Nanotube Stiffness-Variable Samples with Selected Coating Application Intervals

Sample Set ($n = 3$)	Interval (min)	Contractile Strain (%)					
		0.8 V	1.0 V	1.2 V	1.5 V	1.7 V	1.9 V
1	10	0.01 [0.01]	0.03 [0.04]	0.18 [0.06]	0.31 [0.10]	0.37 [0.04]	0.54 [0.12]
2	20	0.02 [0.01]	0.04 [0.04]	0.17 [0.06]	0.42 [0.16]	0.67 [0.19]	0.72 [0.02]
3	30	0.01 [0.05]	0.01 [0.03]	0.07 [0.08]	0.35 [0.07]	0.30 [0.13]	0.41 [0.03]

The most significant strain-voltage rates occurred at various points for these different sample sets, as highlighted by Table 5.22. For the 10 *min* samples, the peak rate of $0.75\% \cdot V^{-1}$ occurred at the 1.0-1.2 V interval, where as for the 30 *min*, the peak rate of $0.93\ \% \cdot V^{-1}$ occurred at the 1.2-1.5 V interval. The 20 *min* samples showed the greatest change in their rates with $1.25\ \% \cdot V^{-1}$ at the 1.5-1.7 V interval.

Like the contractile stress response, the 20 *min* interval resulted in the best performance, while the lesser and greater coating application intervals produced dimin-

Table 5.22: Mean Contractile Engineering Strain-Voltage Rates of 100 μm Carbon Nanotube Stiffness-Variable Samples with Selected Coating Application Intervals

Sample Set ($n = 3$)	Interval (min)	Response Rate (% $\cdot V^{-1}$)				
		0.8-1.0 V	1.0-1.2 V	1.2-1.5 V	1.5-1.7 V	1.7-1.9 V
1	10	0.10	0.75	0.43	0.30	0.85
2	20	0.10	0.65	0.83	1.25	0.25
3	30	0.00	0.30	0.93	-0.25	0.55

ished strains. While the greater interval reduced the tension loss during actuation, as seen in Figure 5.15, and provided a greater returning force as the epoxy cooled after each stimulation cycle, the interactions within the fibre-epoxy boundary layer seem to play a part in modulating this response. Investigating this interaction in greater depth would provide a better understanding of these apparent differences.

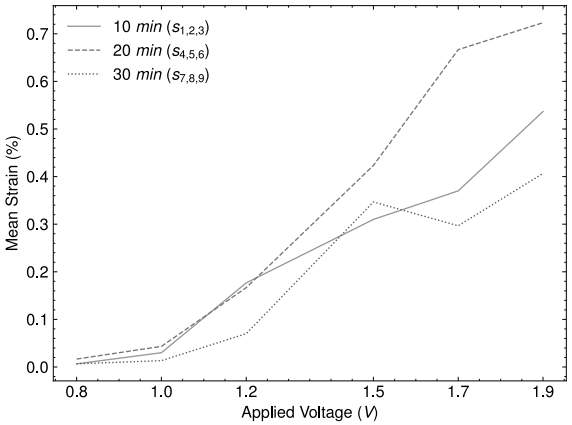

Figure 5.16: Mean contractile engineering strain vs applied voltage for the fabricated stiffness-variable samples using the 10 *min*, 20 *min* and 30 *min* coating application intervals.

5.4 Summary

Understanding the effects of design and operational parameters on the performance of the stiffness-variable actuator, and to a lesser extent, the twisted-coiled actuators, are integral to their adoption in future applications, particularly those that aim to build off of their textile ready form-factor. In this chapter, three design parameters were evaluated, those being the fibre diameter, the percentage of fibre pre-stretch and coating interval time, to observe whether they enhanced or diminished the various actuating properties such as the contractile stress and strain, as well as material properties such as their resistance, and surface temperatures. The results of such

an evaluation are summarized in Table 5.23 for the stiffness-variable actuator and Table 5.24 for the twisted-coiled samples.

Due to the size of the samples and, consequently, the reduced scale of the changes due to these varied parameters, the evaluation presented aims to provide descriptive trends instead of precise quantitative values. While these results are repeatable and consistent, they are particular to the outlined fabrication processes and testing procedures and thus could vary from analyses focused on different commercial products or testing and fabrication procedures.

Table 5.23: Design and Operational Parameter Evaluation in Stiffness-Variable Actuator Summary

Parameter	Δ	Effect on Quality			
		Resistance ($\Omega \cdot cm^{-1}$)	Surface Temperature (℃)	Contractile*	
				Stress (MPa)	Strain (%)
Fibre Diameter (μm)	↑ 100→200	↓ (62.4%) ⟨0.3281→0.1235⟩	↓ (22.1%) ⟨54.3→42.3⟩	↓ (862%) ⟨29.11→4.01⟩	↓ (82%) ⟨0.84→0.15⟩
Pre-stretch (%)	↑ 10,15,20,25	UD‡	↑ ⟨39.5,44.0,52.9,49.5⟩	↑ ⟨20.1,27.24,28.46,16.01⟩	↑ ⟨0.40,0.60,0.85,0.56⟩
Coating Application Interval (min)	↑ 10,20,30	NC†	↗↘ ⟨45.7,55.7,38.7⟩	↓ ⟨26.86,20.63,12.27⟩	↗↘ ⟨0.54,0.72,0.41⟩
Voltage (V)	↑ 0.8→1.9	N/A	↑ (117.2%) ⟨25.0→54.3⟩	↑ (406%) ⟨5.32→26.92⟩	↑ ⟨0.0→0.64⟩

† No change
‡ Undetermined
* Presented stresses and strains are engineering stresses and strains.

Table 5.24: Design and Operational Parameter Evaluation in the Twisted-Coiled Carbon Nanotube Actuator Summary

Parameter	Δ	Effect on Quality			
		Resistance ($\Omega \cdot cm^{-1}$)	Surface Temperature (℃)	Contractile*	
				Stress (MPa)	Strain (%)
Fibre Diameter (μm)	↑ 100→200	↓ (63.2%) ⟨0.4890→0.1799⟩	↓ (2.4%) ⟨29.4→28.7⟩	↓ (787%) ⟨33.46→7.14⟩	NC†
Pre-stretch (%)	↑ 10,15,20,25	↑ (1.75%)	↑ ⟨29.5,29.8,30,30.1⟩	↑ ⟨25.9,31.9,34.9,44.3⟩	N/A
Voltage (V)	↑ 0.8→1,9	N/A	↑§ (17.5%) ⟨25.0→29.4⟩	↑§ (414%) ⟨6.11→31.38⟩	↑ ⟨0.00→0.35⟩

† No change
* Presented stresses and strains are engineering stresses and strains.
§ With 15% Pre-stretch

Chapter 6

Conclusions and Future Work Recommendations

6.1 Conclusions

This thesis aimed to provide the characterization of key actuator properties to determine the viability of a commercial CNT fibre product within a stiffness-variable electrothermal actuator design. A review of the literature was first conducted to gain an understanding of the material properties of CNT based structures, their transition into the commercial space and their role within the context of actuator designs, particularity their various working mechanisms supporting actuation of each design. This also aided in identifying fabrication and design constraints within currently reported actuators. The investigation highlighted critical areas needing improvement that have been instrumental in reducing these materials' uptake within actuator designs. Specifically, the high cost and complexity of the underlying material fabrication, the lack of actuator fabrication standardization and the inconsistent property reporting within the literature are the limiting factors of current CNT actuator designs.

One of the more promising designs, referred to as the stiffness-variable actuator, emphasized these shortcomings, offering an opportunity to reduce the fabrication cost and complexity and improve its fabrication standardization. Additionally, it would allow for an investigation of how specific fabrication parameters endemic to its design affected the resulting actuator's electromechanical performance, expanding on this body of research. The most direct way to reduce these fabrication hurdles was

to use a commercial product, leading to the identification of the DexMat Galvron™ CNT-HS fibre. This material had been proven to be of high quality, low relative cost and had yet to be leveraged within an actuator design, making it ideal for this investigation.

With the selection of an actuator design and the commercial components for its fabrication, a custom fabrication setup was built to create repeatably consistent actuators though the manufacturing process and support adjustable control over the fabrication parameters of interest. Such a setup supported the manufacturing of three samples over a 24-hour time period at a cost of ≈ $2.4 USD per 3 cm sample and was complemented by a selection of testing protocols to measure the various parameters in an isolated manner. The parameters included: resistivity, mechanical strength and stiffness, thermal response and electromechanical responses. These testing procedures first evaluated the properties of the individual actuator components, the CNT fibres as they underwent the various stages of the fabrication process, and the epoxy under various operating conditions, identifying trends that occurred throughout.

It was observed that the twisting and coiling of the plain CNT fibres reduced their tensile strengths and conductance but increased their electromechanical responses due to greater electromagnetic interactions between coils, agreeing with previous findings in the literature. Peak thermal responses increased dramatically after applying the epoxy coating and acted to delay the actuation until 1.2 V was applied, which corresponded to ≈30℃. Furthermore, though the cooling epoxy drove the restoring force to reset the actuator into a loaded state as designed, its presence diminished the contractile stress and strain responses by impeding the inner coil movements. The illustrated temperature-dependant properties of the epoxy were subsequently isolated and found to decrease stiffness by 95% between 22 and 50 ℃ and decrease its volume resistivity though this remained high enough to be negligible for any substantial conductive effects.

The characterization of these stiffness-variable actuator components provided insight into their emergent properties once incorporated into the various stiffness-variable actuator prototypes designed with specific fabrication parameters, aiding in the further identification of relationships that affected the performance of the resulting actuator. In this subsequent actuator evaluation, it was observed that using a CNT material with a larger diameter within the actuator resulted in diminished electrothermal and, consequently, electromechanical responses. The variation in these properties differed substantially compared to the twisted-coiled actuators utilizing these larger diameter materials. This was most apparent by their contractile strain, which experienced no change in this format, and their contractile stress, which decreased by a factor of 36 times more than in the stiffness-variable counterpart.

On the other hand, the variation of the introduced pre-stretch was shown to be effective at increasing the electrothermal and electromechanical responses until around 20%, after which the gains decreased. This was due to the relaxation of the higher tension fibre as a consequence of the epoxy's initial heating and cooling cycles during actuation. However, such behaviour was not seen in the plain twisted-coiled actuators, as they did not depend on the tension balance between the epoxy and the internal CNT fibre spring, resulting in a continuous increase in their contractile stress in the final 25% pre-stretch evaluated. Moreover, while the pre-stretch increase was shown to partially increase the resistance, the values remained very small and inconclusive within the stiffness-variable actuators due to fabrication variability.

Conversely, the increase in the coating application interval time had a mixed effect on the electrothermal response and contractile strain but not on the contractile stress expressed by the actuator. In the case of the electrothermal responses and the contractile strain, the 20 *min* interval produced the highest surface temperatures and strains compared to both the 10 and 30 *min* interval actuators. Since the 20 *min* and 30 *min* interval actuators have comparable diameters with their coating, it alludes to an underlying difference in the interaction between the epoxy and the fibre, most likely due to the epoxy's viscosity during the application, changing the depth of the infiltration that occurred. The contractile stress, however, showed a diminishing trend with increasing interval times due to the greater stiffness of the actuators. In contrast, the resistances showed no discernible differences regardless of interval time.

6.2 Future Work Recommendations

The primary focus of this thesis was the characterization of a commercially available CNT fibre and how its presence within a stiffness-variable actuator design, in conjunction with various design parameters, influenced its performance. While the scope of this work also included additional analyses such as the investigation into the epoxy, additional performance metric analyses are necessary to obtain a more in depth analysis of this design's capabilities and how well it could be adapted into larger applications such as actuating textiles.

As an electrothermally driven actuator, one of these additional metrics would be the rate of temperature increase during actuation. This work limited thermal measurements to fixed-time snapshots due to equipment limitations. Obtaining this temporal information could highlight the rate change that occurs with the varying voltage and the selected design parameters, such as the amount pre-stretch, both

shown to affect the maximum temperatures reached during actuation. Investigating how the actuator's stiffness changed while active would also be beneficial and would complement the passive analysis accomplished in this work. Such an investigation would be difficult, particularly when selecting a strain rate, due to the quick activation time of the actuator and its inability to maintain activity for long periods to avoid damage.

Due to the actuator's spring design, a better understanding of the coiling diameter role could provide better insights into its performance. This work did attempt to manufacture such samples, however, coiling the loose fibre without the support of a substrate while having it remain in that state during the coating and curing procedure remained difficult. Coil diameter increases would proportionally increase the stiffness of the spring, resulting in greater forces and strains at lower applied voltages as they would not require as much stiffness reduction within the epoxy to facilitate movements. Similarly, modifications to the curing process could also present performance changes through a combination of curing time and temperature, known to result in changes to the stiffness of the cured epoxy.

Beyond additional metrics to be tested, another area keen for improvement is the fabrication process. Though the apparatus designed and built aimed to mitigate the variability that could occur during the actuator fabrication process, it was not perfect. For starters, one of the greatest points of variability with the samples was a result of the manual soldering methods required to adhere the CNT fibre to the paper clips. In the literature, authors managed to adhere their CNT sample to silver wires, however, attempts to repeat this method failed due to poor bonding of the solder with the CNT fibre. The solution in this thesis, the pre-wrapping of copper wire around the CNT fibre, provided a better bond for the solder and the paperclip but resulted in a variable amount of resistance between these two conductive surfaces. Finding a better method for bonding these materials could reduce this higher resistance, resulting in more accurate readings for a sample's resistance and, thus, the power across the actuating portion of the sample.

In the same way, the stretching of the twisted-coiled samples was also limited to the manual iterative loading methods to achieve the desired value. A better method could use a screw apparatus with sub-millimetre control to stretch the sample. Such a process could be automated by setting up an additional servo motor that could programmatically adjust the tension while measuring the length extended accurately through optical methods, resulting in more precise values. Lastly, the coating procedure used did not adequately address epoxy movements after the final coating application, particularly the tendency of the epoxy to settle into globs when it was less viscous, even though these globs were mitigated during the procedure. Changing the procedure to use a greater application interval did result in a greater viscosity

and a lesser tendency to glob, though not mitigated entirely. Using a surfactant to reduce the surface tension in the epoxy could reduce this effect and result in more evenly coated samples.

Many of these fabrication errors were amplified due to the relatively small size of the fabricated samples. As such, future investigations should utilize larger samples, between 5-10cm in their initial length which would generate actuators that are 3-7cm long, making 1 mm errors within the stretching process or in the measured strains less than 2%. The limiting factor for this solution is primarily the cost of the materials, while cheaper than they have ever been, still remain expensive.

Finally, with an improved fabrication setup, and broader metric analyses, future investigations should incorporate additional commercial products to see how they alter the resulting actuator's performance due to their intrinsic manufacturer properties. For the epoxy, this could be selecting various epoxies with different thermal resistance, stiffness, viscosity conductivity or curing times, all of which could contribute to different interactions with the fibrous CNT material passively and actively during actuation. In the case of the CNT material, this could be mildly more difficult due to the scarcity of commercial options and the high cost of those that do exist. Nevertheless, these expanded analyses would be instrumental in offering the most rounded characterization of this actuator design and the cost and complexity required to fabricate them.

Bibliography

[1] D. P. Ferris, G. S. Sawicki, and M. A. Daley, "A physiologist's perspective on robotic exoskeletons for human locomotion," *International Journal of Humanoid Robotics*, vol. 4, no. 03, pp. 507–528, 2007.

[2] H. Herr, "Exoskeletons and orthoses: classification, design challenges and future directions," *Journal of neuroengineering and rehabilitation*, vol. 6, no. 1, pp. 1–9, 2009.

[3] M. Xiloyannis, R. Alicea, A.-M. Georgarakis, F. L. Haufe, P. Wolf, L. Masia, and R. Riener, "Soft robotic suits: State of the art, core technologies, and open challenges," *IEEE Transactions on Robotics*, 2021.

[4] C. S. Haines, N. Li, G. M. Spinks, A. E. Aliev, J. Di, and R. H. Baughman, "New twist on artificial muscles," *Proceedings of the National Academy of Sciences*, vol. 113, no. 42, pp. 11 709–11 716, 2016.

[5] S. Y. Yang, K. H. Cho, Y. Kim, K. Kim, J. H. Park, H. S. Jung, J. U. Ko, H. Moon, J. C. Koo, H. Rodrigue *et al.*, "Soft fabric actuator for robotic applications," in *2018 IEEE/RSJ International Conference on Intelligent Robots and Systems (IROS)*. IEEE, 2018, pp. 5451–5456.

[6] J. R. Steele, S. A. Gho, T. E. Campbell, C. J. Richards, S. Beirne, G. M. Spinks, and G. G. Wallace, "The bionic bra: Using electromaterials to sense and modify breast support to enhance active living," *Journal of rehabilitation and assistive technologies engineering*, vol. 5, p. 2055668318775905, 2018.

[7] T. Jia, Y. Wang, Y. Dou, Y. Li, M. Jung de Andrade, R. Wang, S. Fang, J. Li, Z. Yu, R. Qiao *et al.*, "Moisture sensitive smart yarns and textiles from self-balanced silk fiber muscles," *Advanced Functional Materials*, vol. 29, no. 18, p. 1808241, 2019.

[8] B. Holschuh and D. Newman, "Two-spring model for active compression textiles with integrated niti coil actuators," *Smart Materials and Structures*, vol. 24, no. 3, p. 035011, 2015.

[9] S. Güney, İ. Üçgül, and A. Koyun, "Designing the medical textile material providing peristaltic motion and its computerized control," *The Journal of The Textile Institute*, vol. 107, no. 5, pp. 547–552, 2016.

[10] T. L. Buckner and R. Kramer-Bottiglio, "Functional fibers for robotic fabrics," *Multifunctional Materials*, vol. 1, no. 1, p. 012001, 2018.

[11] J. Xiong, J. Chen, and P. S. Lee, "Functional fibers and fabrics for soft robotics, wearables, and human–robot interface," *Advanced Materials*, p. 2002640, 2020.

[12] D. Kongahage and J. Foroughi, "Actuator materials: review on recent advances and future outlook for smart textiles," *Fibers*, vol. 7, no. 3, p. 21, 2019.

[13] D. E. Hodgson, W. Ming, and R. J. Biermann, "Shape memory alloys," *ASM International, Metals Handbook, Tenth Edition.*, vol. 2, pp. 897–902, 1990.

[14] N. Ma, G. Song, and H. Lee, "Position control of shape memory alloy actuators with internal electrical resistance feedback using neural networks," *Smart materials and structures*, vol. 13, no. 4, p. 777, 2004.

[15] Y. He and Q. Sun, "Scaling relationship on macroscopic helical domains in niti tubes," *International Journal of Solids and Structures*, vol. 46, no. 24, pp. 4242–4251, 2009.

[16] J. K. Paik and R. J. Wood, "A bidirectional shape memory alloy folding actuator," *Smart materials and structures*, vol. 21, no. 6, p. 065013, 2012.

[17] P. Boyraz, G. Runge, and A. Raatz, "An overview of novel actuators for soft robotics," in *Actuators*, vol. 7, no. 3. MDPI, 2018, p. 48.

[18] A. M. Nizamani, J. Daudpoto, and M. A. Nizamani, "Development of faster sma actuators," *Shape memory alloys-fundamentals and applications*, pp. 106–126, 2017.

[19] C. S. Haines, M. D. Lima, N. Li, G. M. Spinks, J. Foroughi, J. D. Madden, S. H. Kim, S. Fang, M. J. De Andrade, F. Göktepe *et al.*, "Artificial muscles from fishing line and sewing thread," *science*, vol. 343, no. 6173, pp. 868–872, 2014.

[20] W. Guo, C. Liu, F. Zhao, X. Sun, Z. Yang, T. Chen, X. Chen, L. Qiu, X. Hu, and H. Peng, "A novel electromechanical actuation mechanism of a carbon nanotube fiber," *Advanced Materials*, vol. 24, no. 39, pp. 5379–5384, 2012.

[21] J. A. Isaacs, A. Tanwani, M. Healy, and L. Dahlben, "Economic assessment of single-walled carbon nanotube processes," *Journal of Nanoparticle Research*, vol. 12, no. 2, pp. 551–562, 2010.

[22] I. Rahatwan, P. P. Wulan, and M. Solahudin, "Techno-economic analysis of pilot scale carbon nanotube production from lpg with fe-co-mo/mgo catalyst in indonesia," in *AIP Conference Proceedings*, vol. 2230, no. 1. AIP Publishing LLC, 2020, p. 030013.

[23] S. Temizel-Sekeryan, F. Wu, and A. L. Hicks, "Global scale life cycle environmental impacts of single-and multi-walled carbon nanotube synthesis processes," *The International Journal of Life Cycle Assessment*, vol. 26, no. 4, pp. 656–672, 2021.

[24] H. Qian, E. S. Greenhalgh, M. S. Shaffer, and A. Bismarck, "Carbon nanotube-based hierarchical composites: a review," *Journal of Materials Chemistry*, vol. 20, no. 23, pp. 4751–4762, 2010.

[25] Y. Bai, R. Zhang, X. Ye, Z. Zhu, H. Xie, B. Shen, D. Cai, B. Liu, C. Zhang, Z. Jia *et al.*, "Carbon nanotube bundles with tensile strength over 80 gpa," *Nature nanotechnology*, vol. 13, no. 7, pp. 589–595, 2018.

[26] Y. Dini, D. Rouchon, J. Faure-Vincent, and J. Dijon, "Large improvement of cnt yarn electrical conductivity by varying chemical doping and annealing treatment," *Carbon*, vol. 156, pp. 38–48, 2020.

[27] Y. Dini, J. Faure-Vincent, and J. Dijon, "How to overcome the electrical conductivity limitation of carbon nanotube yarns drawn from carbon nanotube arrays," *Carbon*, vol. 144, pp. 301–311, 2019.

[28] D. S. Lashmore, "Conductivity mechanisms in cnt yarn," in *Nanotube Superfiber Materials*. Elsevier, 2019, pp. 447–464.

[29] J.-G. Kim, D. Suh, and H. Kang, "Large variation in young's modulus of carbon nanotube yarns with different diameters," *Current applied physics*, vol. 21, pp. 96–100, 2021.

[30] B. G. Demczyk, Y. M. Wang, J. Cumings, M. Hetman, W. Han, A. Zettl, and R. Ritchie, "Direct mechanical measurement of the tensile strength and elastic modulus of multiwalled carbon nanotubes," *Materials Science and Engineering: A*, vol. 334, no. 1-2, pp. 173–178, 2002.

[31] L. Zhigilei, R. Salaway, B. Wittmaack, and A. Volkov, "Carbon nanotubes for interconnects: Process, design and applications," 2017.

[32] M. J. Treacy, T. W. Ebbesen, and J. M. Gibson, "Exceptionally high young's modulus observed for individual carbon nanotubes," *nature*, vol. 381, no. 6584, pp. 678–680, 1996.

[33] A. Ghemes, Y. Minami, J. Muramatsu, M. Okada, H. Mimura, and Y. Inoue, "Fabrication and mechanical properties of carbon nanotube yarns spun from ultra-long multi-walled carbon nanotube arrays," *Carbon*, vol. 50, no. 12, pp. 4579–4587, 2012.

[34] Y. Sugimoto, M. Shioya, H. Matsumoto, M. Minagawa, and A. Tanioka, "Structure changes during tensile deformation and mechanical properties of a twisted carbon nanotube yarn," *Carbon*, vol. 60, pp. 193–201, 2013.

[35] Y.-L. Li, I. A. Kinloch, and A. H. Windle, "Direct spinning of carbon nanotube fibers from chemical vapor deposition synthesis," *Science*, vol. 304, no. 5668, pp. 276–278, 2004.

[36] X.-H. Zhong, Y.-L. Li, Y.-K. Liu, X.-H. Qiao, Y. Feng, J. Liang, J. Jin, L. Zhu, F. Hou, and J.-Y. Li, "Continuous multilayered carbon nanotube yarns," *Advanced materials*, vol. 22, no. 6, pp. 692–696, 2010.

[37] L. M. Ericson, H. Fan, H. Peng, V. A. Davis, W. Zhou, J. Sulpizio, Y. Wang, R. Booker, J. Vavro, C. Guthy *et al.*, "Macroscopic, neat, single-walled carbon nanotube fibers," *Science*, vol. 305, no. 5689, pp. 1447–1450, 2004.

[38] S. Zhang, K. K. Koziol, I. A. Kinloch, and A. H. Windle, "Macroscopic fibers of well-aligned carbon nanotubes by wet spinning," *Small*, vol. 4, no. 8, pp. 1217–1222, 2008.

[39] M. Zhang, K. R. Atkinson, and R. H. Baughman, "Multifunctional carbon nanotube yarns by downsizing an ancient technology," *Science*, vol. 306, no. 5700, pp. 1358–1361, 2004.

[40] K. Liu, Y. Sun, R. Zhou, H. Zhu, J. Wang, L. Liu, S. Fan, and K. Jiang, "Carbon nanotube yarns with high tensile strength made by a twisting and shrinking method," *Nanotechnology*, vol. 21, no. 4, p. 045708, 2009.

[41] H. Choo, Y. Jung, Y. Jeong, H. C. Kim, and B.-C. Ku, "Fabrication and applications of carbon nanotube fibers," *Carbon letters*, vol. 13, no. 4, pp. 191–204, 2012.

[42] P. Liu, D. C. Hu, T. Q. Tran, D. Jewell, and H. M. Duong, "Electrical property enhancement of carbon nanotube fibers from post treatments," *Colloids and Surfaces A: Physicochemical and Engineering Aspects*, vol. 509, pp. 384–389, 2016.

[43] O. Weizman, J. Mead, H. Dodiuk, and S. Kenig, "Electrical properties enhancement of carbon nanotube yarns by cyclic loading," *Molecules*, vol. 25, no. 20, p. 4824, 2020.

[44] J. Zhou, G. Sun, Z. Zhan, L. Zheng, and E. Xie, "Twisting dependent properties of twisted carbon nanotube fibers: microstructure and strain transfer factors," *Materials Research Express*, vol. 1, no. 3, p. 035025, 2014.

[45] J. C. Anike, K. Belay, and J. L. Abot, "Effect of twist on the electromechanical properties of carbon nanotube yarns," *Carbon*, vol. 142, pp. 491–503, 2019.

[46] M. Miao, J. McDonnell, L. Vuckovic, and S. C. Hawkins, "Poisson's ratio and porosity of carbon nanotube dry-spun yarns," *Carbon*, vol. 48, no. 10, pp. 2802–2811, 2010.

[47] N. T. Alvarez, P. Miller, M. R. Haase, R. Lobo, R. Malik, and V. Shanov, "Tailoring physical properties of carbon nanotube threads during assembly," *Carbon*, vol. 144, pp. 55–62, 2019.

[48] M. D. Lima, N. Li, M. J. De Andrade, S. Fang, J. Oh, G. M. Spinks, M. E. Kozlov, C. S. Haines, D. Suh, J. Foroughi *et al.*, "Electrically, chemically, and photonically powered torsional and tensile actuation of hybrid carbon nanotube yarn muscles," *science*, vol. 338, no. 6109, pp. 928–932, 2012.

[49] P. Chen, S. He, Y. Xu, X. Sun, and H. Peng, "Electromechanical actuator ribbons driven by electrically conducting spring-like fibers," *Advanced Materials*, vol. 27, no. 34, pp. 4982–4988, 2015.

[50] J. W. Hearle, P. Grosberg, and S. Backer, "Structural mechanics of fibers, yarns, and fabrics," 1969.

[51] Y. Jung, Y. S. Cho, J. W. Lee, J. Y. Oh, and C. R. Park, "How can we make carbon nanotube yarn stronger?" *Composites Science and Technology*, vol. 166, pp. 95–108, 2018.

[52] D. W. Lee, S. H. Kim, M. E. Kozlov, X. Lepró, R. H. Baughman, and S. J. Kim, "Magnetic torsional actuation of carbon nanotube yarn artificial muscle," *RSC advances*, vol. 8, no. 31, pp. 17 421–17 425, 2018.

[53] J.-W. Jiang, J.-S. Wang, and B. Li, "Thermal expansion in single-walled carbon nanotubes and graphene: Nonequilibrium green's function approach," *Physical Review B*, vol. 80, no. 20, p. 205429, 2009.

[54] J. Foroughi, G. M. Spinks, S. Aziz, A. Mirabedini, A. Jeiranikhameneh, G. G. Wallace, M. E. Kozlov, and R. H. Baughman, "Knitted carbon-nanotube-sheath/spandex-core elastomeric yarns for artificial muscles and strain sensing," *ACS nano*, vol. 10, no. 10, pp. 9129–9135, 2016.

[55] J. Mu, M. Jung de Andrade, S. Fang, X. Wang, E. Gao, N. Li, S. H. Kim, H. Wang, C. Hou, Q. Zhang *et al.*, "Sheath-run artificial muscles," *Science*, vol. 365, no. 6449, pp. 150–155, 2019.

[56] L. Xu, Q. Peng, Y. Zhu, X. Zhao, M. Yang, S. Wang, F. Xue, Y. Yuan, Z. Lin, F. Xu *et al.*, "Artificial muscle with reversible and controllable deformation based on stiffness-variable carbon nanotube spring-like nanocomposite yarn," *Nanoscale*, vol. 11, no. 17, pp. 8124–8132, 2019.

[57] J.-H. Jeong, T. J. Mun, H. Kim, J. H. Moon, D. W. Lee, R. H. Baughman, and S. J. Kim, "Carbon nanotubes–elastomer actuator driven electrothermally by low-voltage," *Nanoscale Advances*, vol. 1, no. 3, pp. 965–968, 2019.

[58] T. Mirfakhrai, J. Y. Oh, M. Kozlov, S. L. Fang, M. Zhang, R. H. Baughman, and J. D. Madden, "Carbon nanotube yarns as high load actuators and sensors," in *Advances in Science and Technology*, vol. 61. Trans Tech Publ, 2008, pp. 65–74.

[59] D. Li, W. F. Paxton, R. H. Baughman, T. J. Huang, J. F. Stoddart, and P. S. Weiss, "Molecular, supramolecular, and macromolecular motors and artificial muscles," *MRS bulletin*, vol. 34, no. 9, pp. 671–681, 2009.

[60] J. Foroughi, G. M. Spinks, G. G. Wallace, J. Oh, M. E. Kozlov, S. Fang, T. Mirfakhrai, J. D. Madden, M. K. Shin, S. J. Kim *et al.*, "Torsional carbon nanotube artificial muscles," *Science*, vol. 334, no. 6055, pp. 494–497, 2011.

[61] Q. Pei and O. Inganäs, "Electrochemical muscles: bending strips built from conjugated polymers," *Synthetic metals*, vol. 57, no. 1, pp. 3718–3723, 1993.

[62] P. Chen, Y. Xu, S. He, X. Sun, S. Pan, J. Deng, D. Chen, and H. Peng, "Hierarchically arranged helical fibre actuators driven by solvents and vapours," *Nature nanotechnology*, vol. 10, no. 12, pp. 1077–1083, 2015.

[63] J. A. Lee, N. Li, C. S. Haines, K. J. Kim, X. Lepró, R. Ovalle-Robles, S. J. Kim, and R. H. Baughman, "Electrochemically powered, energy-conserving carbon nanotube artificial muscles," *Advanced Materials*, vol. 29, no. 31, p. 1700870, 2017.

[64] J. Gong, H. Lin, J. W. Dunlop, and J. Yuan, "Hierarchically arranged helical fiber actuators derived from commercial cloth," *Advanced Materials*, vol. 29, no. 16, p. 1605103, 2017.

[65] S. Aziz, J. G. Martinez, J. Foroughi, G. M. Spinks, and E. W. Jager, "Artificial muscles from hybrid carbon nanotube-polypyrrole-coated twisted and coiled yarns," *Macromolecular Materials and Engineering*, vol. 305, no. 11, p. 2000421, 2020.

[66] T. Watanabe, S. Yamazaki, S. Yamashita, T. Inaba, S. Muroga, T. Morimoto, K. Kobashi, and T. Okazaki, "Comprehensive characterization of structural, electrical, and mechanical properties of carbon nanotube yarns produced by various spinning methods," *Nanomaterials*, vol. 12, no. 4, p. 593, 2022.

[67] *Galvron CNT-HS Fiber - 40 μm Diameter*, DexMat, 2023. [Online]. Available: https://store.dexmat.com/galvorn-cnt-hs-fiber-40-microns

[68] *Galvron CNT-HS Fiber - 100 μm Diameter*, DexMat, 2023. [Online]. Available: https://store.dexmat.com/galvorn-cnt-hs-fiber-100-microns

[69] *Galvorn CNT-HS Twisted Yarn - 200 μm Diameter*, DexMat, 2023. [Online]. Available: https://store.dexmat.com/galvorn-cnt-hs-twisted-yarn-200-microns

[70] K. J. Kim, J. S. Hyeon, H. Kim, T. J. Mun, C. S. Haines, N. Li, R. H. Baughman, and S. J. Kim, "Enhancing the work capacity of electrochemical artificial muscles by coiling plies of twist-released carbon nanotube yarns," *ACS applied materials & interfaces*, vol. 11, no. 14, pp. 13 533–13 537, 2019.

[71] C. H. Kwon, K.-Y. Chun, S. H. Kim, J.-H. Lee, J.-H. Kim, M. D. Lima, R. H. Baughman, and S. J. Kim, "Torsional behaviors of polymer-infiltrated carbon nanotube yarn muscles studied with atomic force microscopy," *Nanoscale*, vol. 7, no. 6, pp. 2489–2496, 2015.

[72] L. Xu, Q. Peng, X. Zhao, P. Li, J. Xu, and X. He, "A photoactuator based on stiffness-variable carbon nanotube nanocomposite yarn," *ACS Applied Materials & Interfaces*, vol. 12, no. 36, pp. 40 711–40 718, 2020.

[73] A. Dalla Colletta, M. Pelin, S. Sosa, L. Fusco, M. Prato, and A. Tubaro, "Carbon-based nanomaterials and skin: An overview," *Carbon*, 2022.

[74] H. Zhao, Y. Zhang, P. D. Bradford, Q. Zhou, Q. Jia, F.-G. Yuan, and Y. Zhu, "Carbon nanotube yarn strain sensors," *Nanotechnology*, vol. 21, no. 30, p. 305502, 2010.

[75] T. Guinovart, M. Parrilla, G. A. Crespo, F. X. Rius, and F. J. Andrade, "Potentiometric sensors using cotton yarns, carbon nanotubes and polymeric membranes," *Analyst*, vol. 138, no. 18, pp. 5208–5215, 2013.

[76] C. B. Jacobs, I. N. Ivanov, M. D. Nguyen, A. G. Zestos, and B. J. Venton, "High temporal resolution measurements of dopamine with carbon nanotube yarn microelectrodes," *Analytical chemistry*, vol. 86, no. 12, pp. 5721–5727, 2014.

[77] H. Kim, J. A. Lee, H. J. Sim, M. D. Lima, R. H. Baughman, and S. J. Kim, "Temperature-responsive tensile actuator based on multi-walled carbon nanotube yarn," *Nano-Micro Letters*, vol. 8, no. 3, pp. 254–259, 2016.

[78] J. A. Lee, M. K. Shin, S. H. Kim, S. J. Kim, G. M. Spinks, G. G. Wallace, R. Ovalle-Robles, M. D. Lima, M. E. Kozlov, and R. H. Baughman, "Hybrid nanomembranes for high power and high energy density supercapacitors and their yarn application," *ACS nano*, vol. 6, no. 1, pp. 327–334, 2012.

[79] S. H. Kim, C. S. Haines, N. Li, K. J. Kim, T. J. Mun, C. Choi, J. Di, Y. J. Oh, J. P. Oviedo, J. Bykova *et al.*, "Harvesting electrical energy from carbon nanotube yarn twist," *Science*, vol. 357, no. 6353, pp. 773–778, 2017.

[80] H. Inoue, T. Yoshiyama, M. Hada, D. Chujo, Y. Saito, T. Nishikawa, Y. Yamashita, W. Takarada, H. Matsumoto, and Y. Hayashi, "High-performance structure of a coil-shaped soft-actuator consisting of polymer threads and carbon nanotube yarns," *AIP Advances*, vol. 8, no. 7, p. 075316, 2018.

[81] Y. Song, S. Zhou, K. Jin, J. Qiao, D. Li, C. Xu, D. Hu, J. Di, M. Li, Z. Zhang *et al.*, "Hierarchical carbon nanotube composite yarn muscles," *Nanoscale*, vol. 10, no. 8, pp. 4077–4084, 2018.

[82] *Model 2010 7-1/2 Digit Low Noise Autoranging Multimeter*, Keithley, 2013. [Online]. Available: https://download.tek.com/datasheet/2010.pdf

[83] *BioTester 5000 User Manual - BioTester 5000 Biaxial Test System*, CellScale, 2021. [Online]. Available: https://www.cellscale.com/downloads2/BioTester%20User%20Manual.pdf

[84] *Infrared Camera with MSX & WIFI - FLIR EX-Series*, TELEDYNE FlIR, 2019. [Online]. Available: https://flir.netx.net/file/asset/17975/original/attachment

[85] *DC Power Supply - PS-3010F User Manual*, Kaiweets, 2020. [Online]. Available: https://drive.google.com/file/d/1RE3V8UlGtVNIDANAgmC8R13rNH8NVZqE/view

[86] A. Lekawa-Raus, J. Patmore, L. Kurzepa, J. Bulmer, and K. Koziol, "Electrical properties of carbon nanotube based fibers and their future use in electrical wiring," *Advanced Functional Materials*, vol. 24, no. 24, pp. 3661–3682, 2014.

[87] C. Young, "Temperature dependence and temperature limits of galvorn cnt products," Feb 2021. [Online]. Available: https://blog.dexmat.com/temperature-dependence-and-temperature-limits-of-galvorn-cnt-products

Appendices

Appendix A

Fabrication Apparatus

A.1 Apparatus User Interface and Flow Diagram

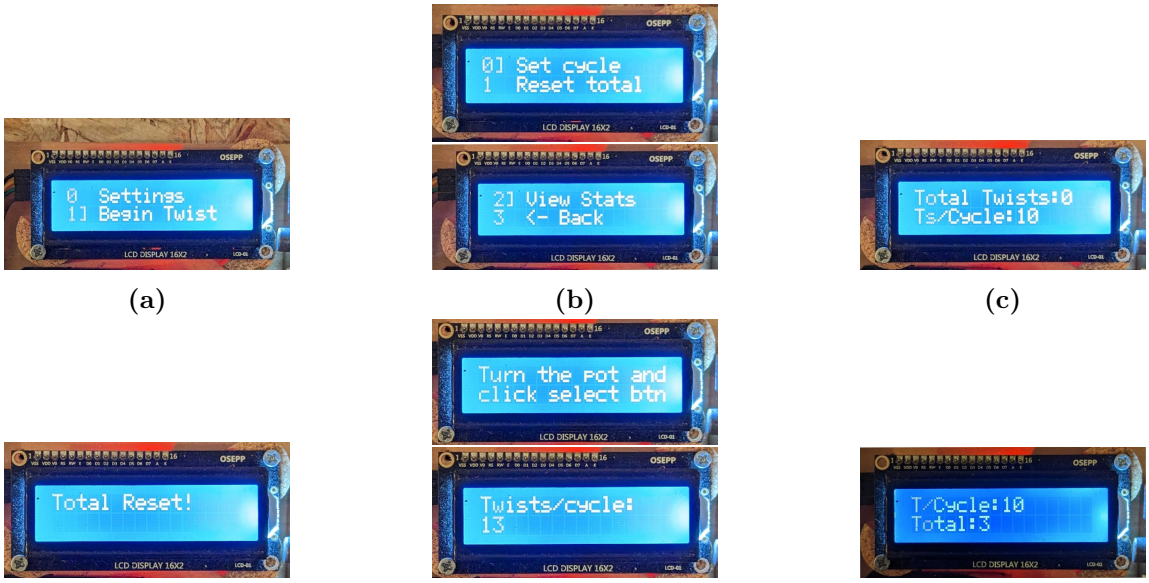

(a) **(b)** **(c)**

(d) **(e)** **(f)**

Figure A.1: Selected screenshots of the fabrication apparatus GUI with the main screen (a), the settings screen (b), the show status screen (c), the reset cycle screen (d), the set twists per cycle screen (e) and the twisting screen (f).

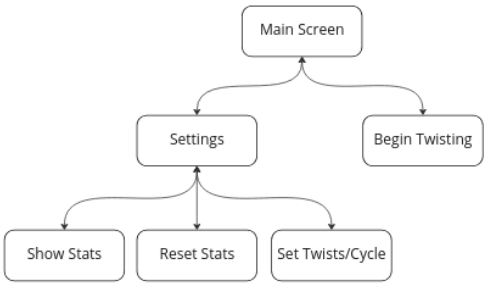

Figure A.2: Flow diagram of the fabrication apparatus GUI.

A.2 Apparatus Electrical Schematic

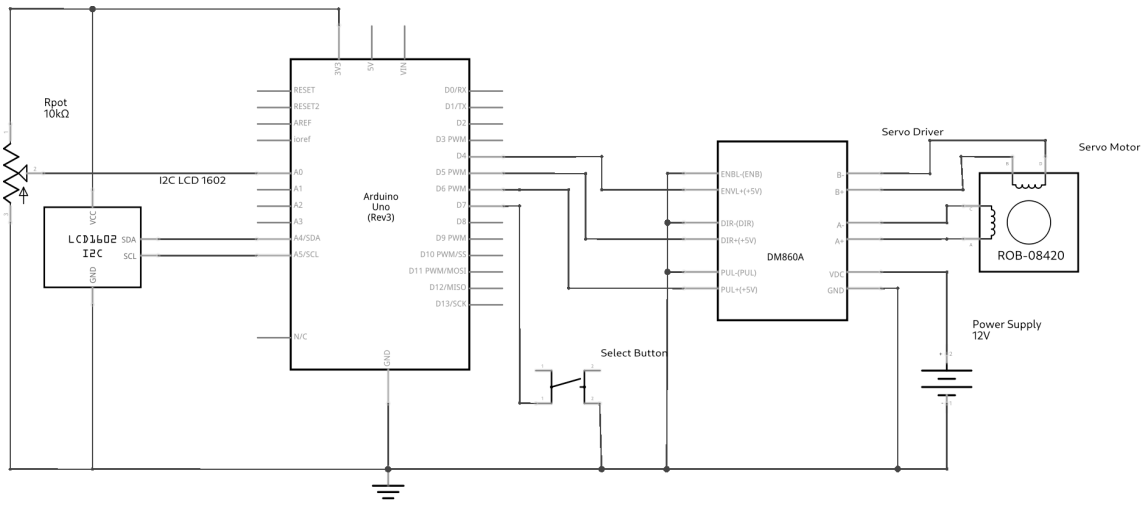

Figure A.3: Fabrication apparatus schematic

A.3 Apparatus Software

```
#include <Wire.h>
#include <LiquidCrystal_I2C.h>
#include <AccelStepper.h>

// Constants
#define STEPPER_ENABLE_PIN 4
#define STEPPER_DIRECTION_PIN 5
#define STEPPER_STEP_PIN 6

#define SELECT_BUTTON_PIN 2
#define POTENTIOMETER_PIN A0

#define LCD_ROWS 2
#define LCD_COLS 16
```

```
// Globals
AccelStepper stepper = AccelStepper(1, STEPPER_STEP_PIN, STEPPER_DIRECTION_PIN);
LiquidCrystal_I2C lcd(0x27, LCD_COLS, LCD_ROWS);
int twistsPerCycle = 10; // Set this as a default, but can be modified through configuration
int totalSessionTwists = 0;

// Helpers
void waitForButtonLow() {
  while (digitalRead(SELECT_BUTTON_PIN) == HIGH) {
    delay(250);
  }
}

int getMenuSelection(int numberOfOptions) {
  int rawReading = analogRead(POTENTIOMETER_PIN);
  int mapped = map(rawReading, 0, 1023, 0, 9);

  if (mapped > numberOfOptions - 1) {
    return numberOfOptions - 1;
  } else {
    return mapped;
  }
}

void updateLCDSelector(int selection, const char * options[], int numberOfOptions) {
  int start;

  if (selection > numberOfOptions - LCD_ROWS) {
    start = numberOfOptions - LCD_ROWS;
  } else if (selection < LCD_ROWS) {
    start = 0;
  } else {
    start = selection;
  }

  // Show options on the screen
  for (int i = start, j = 0; j < LCD_ROWS; j++, i++) {
    char text[17];
    char num[2];

    itoa(i, num, 10);

    if (selection == i) {
      snprintf(text, sizeof(text), "%s%s%s", num, "]-", options[i]);
    } else {
      snprintf(text, sizeof(text), "%s%s%s", num, "--", options[i]);
    }

    lcd.setCursor(0, j);

    lcd.print("----------------");

    lcd.setCursor(0, j);

    lcd.print(text);
  }
}

int waitForUserInput(const char * options[], int numberOfOptions) {
  int selection = -1;
  int newSelection;

  while (digitalRead(SELECT_BUTTON_PIN) == LOW) {
    newSelection = getMenuSelection(numberOfOptions);

    if (newSelection != selection) {
      updateLCDSelector(newSelection, options, numberOfOptions);
      selection = newSelection;
    }
  }

  delay(500);

  return selection;
}

// Menus
void setDefaultTwistCycle() {
  int rawReading;

  lcd.clear();
  lcd.setCursor(0, 0);
  lcd.print("Turn the pot and");
  lcd.setCursor(0, 1);
  lcd.print("click select btn");
```

```
  delay(3000);

  lcd.clear();
  lcd.print("Twists/cycle:");

  //Need to press button to exit loop
  while (digitalRead(SELECT_BUTTON_PIN) == LOW) {
    lcd.setCursor(0, 1);

    rawReading = analogRead(POTENTIOMETER_PIN);
    twistsPerCycle = map(rawReading, 0, 1023, 0, 50);

    lcd.print(twistsPerCycle);

    delay(250);
  }

  delay(1000);

  // Wait until button is low once again
  waitForButtonLow();
}

void resetTotalSessionTwists() {
  lcd.clear();
  lcd.setCursor(0, 0);
  lcd.print("Total Reset!");

  totalSessionTwists = 0;

  delay(2000);
}

void viewStats() {
  lcd.clear();
  lcd.setCursor(0, 0);
  lcd.print("Total Twists:");
  lcd.print(totalSessionTwists);

  lcd.setCursor(0, 1);
  lcd.print("Ts/Cycle:");
  lcd.print(twistsPerCycle);

  delay(2000);
}

void configure() {
  lcd.clear();

  // Show options on the screen
  const char * options[] {
    "Set cycle",
    "Reset total",
    "View Stats",
    "<- Back"
  };

  int selection = waitForUserInput(options, 4);

  switch (selection) {
    case 0:
      setDefaultTwistCycle();
      configure();
      break;
    case 1:
      resetTotalSessionTwists();
      configure();
      break;
    case 2:
      viewStats();
      configure();
      break;
    case 3:
      break;
  }
}

void performTwistCycle() {
  lcd.clear();

  lcd.setCursor(0, 0);

  char twistCycleOption[16] = "T/Cycle:";
  char twistsPerCycleChar[4];
```

```
  itoa(twistsPerCycle, twistsPerCycleChar, 10);

  strcat(twistCycleOption, twistsPerCycleChar);

  lcd.print(twistCycleOption);


  lcd.setCursor(0, 1);

  char twistTotal[16] = "Total:";

  char totalSessionTwistsChar[4];

  itoa(totalSessionTwists, totalSessionTwistsChar, 10);

  strcat(twistTotal, totalSessionTwistsChar);

  lcd.print(twistTotal);

  // Perform x many twists through the stepper motor and return to main screen
  const int STEPPER_STEPS_PER_ROTATIONS = 200;
  const int STEPPER_SPEED = 100;

  long steps = long(twistsPerCycle) * STEPPER_STEPS_PER_ROTATIONS;
  boolean counted = false;

  stepper.enableOutputs();
  stepper.move(steps);

  while (stepper.distanceToGo() != 0) {
    stepper.setSpeed(STEPPER_SPEED);
    stepper.runSpeedToPosition();

    Serial.println(stepper.currentPosition());
    Serial.println(stepper.currentPosition() % STEPPER_STEPS_PER_ROTATIONS == 0);

    if (stepper.currentPosition() % STEPPER_STEPS_PER_ROTATIONS == 0 && !counted) {
      totalSessionTwists += 1;

      itoa(totalSessionTwists, totalSessionTwistsChar, 10);

      lcd.setCursor(6, 1);
      lcd.print(totalSessionTwists);
      counted = true;
    } else {
      counted = false;
    }
  }

  stepper.disableOutputs();

  delay(2000);
}

void setup() {
  Serial.begin(9600); // send and receive at 9600 baud

  // Set enable pin and pin orientation
  stepper.setEnablePin(STEPPER_ENABLE_PIN);
  stepper.setPinsInverted(false, false, true);
  stepper.setMaxSpeed(5000);

  // Setup LCD
  lcd.init();
  lcd.backlight();
  lcd.clear();

  // Setup Pot
  pinMode(POTENTIOMETER_PIN, INPUT);
}

void loop() {
  Serial.println("Initialize");

  // Show options on the screen
  const char * options[] {
    "Settings",
    "Begin Twist"
  };

  int selection = waitForUserInput(options, 2);

  // Await input from the buttons
  switch (selection) {
    case 0:
      configure();
```

```
      break;
    case 1:
      performTwistCycle();
      break;
    default:
      break;
  }
}
```

A.4 Electromechanical Response of Validation Samples

Table A.1: Isometric Test Summary of Fabricated Validation Stiffness-Variable Actuator Samples

Sample	Contractile Stress (MPa) [σ]					
	0.8 V	1.0 V	1.2 V	1.5 V	1.7 V	1.9 V
s_1	5.09 [0.00]	7.08 [0.65]	18.41 [0.65] 28.73	[1.95]	29.87 [0.65]	29.16 [1.28]
s_2	3.74 [0.27]	10.01 [0.29]	16.76 [1.09]	22.72 [2.49]	27.54 [0.88]	25.84 [1.57]
s_3	5.94 [0.90]	9.55 [0.33]	18.38 [1.14]	24.06 [0.84]	26.83 [0.66]	29.16 [0.83]

Table A.2: Isotonic Test Summary With 4 g Load of Fabricated Validation Stiffness-Variable Actuator Samples

Sample	Contractile Strain (%) [σ]					
	0.8 V	1.0 V	1.2 V	1.5 V	1.7 V	1.9 V
s_1	0.00 [0.00]	0.04 [0.04]	0.13 [0.03]	0.25 [0.03]	0.49 [0.05]	0.77 [0.05]
s_2	0.03 [0.04]	0.22 [0.08]	0.35 [0.09]	0.41 [0.14]	0.71 [0.13]	0.94 [0.07]
s_3	0.02 [0.03]	0.08 [0.03]	0.22 [0.07]	0.34 [0.03]	0.52 [0.08]	0.84 [0.13]

Appendix B

DetMat Fibre Characterization

B.1 Electromechanical Response

Table B.1: Isometric Test Summary of 100 μm Carbon Nanotube Pre-twisted Samples

Sample	Contractile Stress (MPa)					
	0.8 V	1.0 V	1.2 V	1.5 V	1.7 V	1.9 V
s_1	0.00	0.00	3.72	5.67	4.76	5.22
s_2	0.00	0.00	2.80	4.20	4.30	5.87
s_3	0.00	0.00	1.91	6.06	5.60	4.74
s_4	0.00	0.00	2.16	5.11	4.30	4.87

Table B.2: Isometric Test Summary of 100 μm Carbon Nanotube Twisted-Coiled Samples

Sample	Contractile Stress (MPa)					
	0.8 V	1.0 V	1.2 V	1.5 V	1.7 V	1.9 V
s_1	6.24	6.88	9.37	10.57	11.33	12.35
s_2	5.96	6.49	6.80	7.29	10.06	9.88
s_3	3.57	4.58	5.73	6.25	8.31	10.31
s_4	4.07	5.36	7.00	7.32	10.02	14.01

Table B.3: Isometric Test Summary of 100 μm Carbon Nanotube Stretched Samples

Sample	Contractile Stress (MPa)					
	0.8 V	1.0 V	1.2 V	1.5 V	1.7 V	1.9 V
s_1	8.79	10.57	16.42	18.46	23.05	32.85
s_2	5.09	5.73	6.37	12.26	21.34	29.79
s_3	5.09	6.12	12.75	19.42	22.62	28.78
s_4	5.47	8.91	13.11	14.61	25.66	34.12

Table B.4: Isometric Test Summary of 100 μm Carbon Nanotube Coated Samples

Sample	Contractile Stress (MPa)					
	0.8 V	1.0 V	1.2 V	1.5 V	1.7 V	1.9 V
s_1	5.09	5.73	7.13	14.64	20.50	26.1
s_2	5.47	6.37	8.79	18.97	24.45	28.6
s_3	4.75	5.95	7.26	16.48	22.14	25.8
s_4	5.98	6.75	8.28	17.44	22.03	27.1

Table B.5: Mean Contractile Engineering Stress vs Voltage for Selected Fabrication Stages of 100 μm Carbon Nanotube Samples

Fabrication Stage ($n = 4$)	Contractile Stress (MPa) [σ]					
	0.8 V	1.0 V	1.2 V	1.5 V	1.7 V	1.9 V
Pre-twisted	0.00 [0.00]	0.00 [0.00]	2.65 [0.81]	5.26 [0.81]	4.74 [0.61]	5.18 [0.51]
Twisted-Coiled	4.96 [1.34]	5.83 [1.05]	7.22 [1.53]	7.86 [1.88]	9.93 [1.24]	11.64 [1.91]
Stretched	6.11 [1.80]	7.83 [2.31]	12.16 [4.20]	16.19 [3.34]	23.17 [1.81]	31.38 [2.51]
Coated	5.32 [0.53]	6.2 [0.45]	7.86 [0.80]	16.88 [1.81]	22.28 [1.63]	26.92 [1.28]

Table B.6: Mean Contractile Engineering Stress-Voltage Rates for Selected Fabrication Stages of 100 μm Carbon Nanotube Samples

Fabrication Stage ($n = 4$)	Contractile Stress-Voltage Rate ($MPa \cdot V^{-1}$) [σ]				
	0.8-1.0 V	1.0-1.2 V	1.2-1.5 V	1.5-1.7 V	1.7-1.9 V
Pre-twisted	0.0	13.25	8.7	-2.6	2.2
Twisted-Coiled	4.35	6.95	2.13	10.35	8.55
Stretched	8.6	21.65	13.43	34.9	41.05
Coated	4.4	8.3	30.07	27.0	23.2

Table B.7: Isotonic Test Summary of 100 μm Carbon Nanotube Pre-twisted Samples

Sample	Contractile Strain (%)					
	0.8 V	1.0 V	1.2 V	1.5 V	1.7 V	1.9 V
s_1	0.00	0.00	0.00	0.00	0.00	0.00
s_2	0.00	0.00	0.00	0.00	0.00	0.00
s_3	0.00	0.00	0.00	0.00	0.00	0.00
s_4	0.00	0.00	0.00	0.00	0.00	0.00

Table B.8: Isotonic Test Summary of 100 μm Carbon Nanotube Twisted-Coiled Samples

Sample	Contractile Strain (%)					
	0.8 V	1.0 V	1.2 V	1.5 V	1.7 V	1.9 V
s_1	0.00	0.00	0.10	0.16	0.26	0.33
s_2	0.00	0.00	0.07	0.13	0.24	0.38
s_3	0.00	0.06	0.11	0.17	0.22	0.28
s_4	0.00	0.06	0.13	0.15	0.24	0.41

Table B.9: Isotonic Test Summary of 100 μm Carbon Nanotube Coated Samples

Sample	Contractile Strain (%)					
	0.8 V	1.0 V	1.2 V	1.5 V	1.7 V	1.9 V
s_1	0.00	0.00	0.04	0.13	0.26	0.44
s_2	0.00	0.07	0.20	0.51	0.41	0.76
s_3	0.00	0.03	0.18	0.24	0.36	0.54
s_4	0.00	0.05	0.18	0.36	0.41	0.81

Table B.10: Mean Contractile Engineering Strain vs Voltage for Selected Fabrication Stages of 100 μm Carbon Nanotube Samples

Fabrication Stage ($n = 4$)	Contractile Strain (%) [σ]					
	0.8 V	1.0 V	1.2 V	1.5 V	1.7 V	1.9 V
Pre-twisted	0.00 [0.00]	0.00 [0.00]	0.00 [0.00]	0.00 [0.00]	0.00 [0.00]	0.00 [0.00]
Twisted-Coiled	0.00 [0.00]	0.03 [0.03]	0.1 [0.02]	0.15 [0.02]	0.24 [0.02]	0.35 [0.06]
Coated	0.00 [0.00]	0.04 [0.03]	0.15 [0.07]	0.31 [0.16]	0.36 [0.07]	0.64 [0.18]

Table B.11: Mean Contractile Engineering Strain-Voltage Rates for Selected Fabrication Stages of 100 μm Carbon Nanotube Samples

Fabrication Stage ($n = 4$)	Contractile Strain-Voltage Rate (% $\cdot V^{-1}$) [σ]				
	0.8-1.0 V	1.0-1.2 V	1.2-1.5 V	1.5-1.7 V	1.7-1.9 V
Pre-twisted	0.00	0.00	0.00	0.00	0.00
Twisted-Coiled	0.15	0.35	0.17	0.45	0.55
Coated	0.20	0.55	0.53	0.25	1.4

Appendix C

Epoxy Characterization

C.1 Fabrication Apparatus

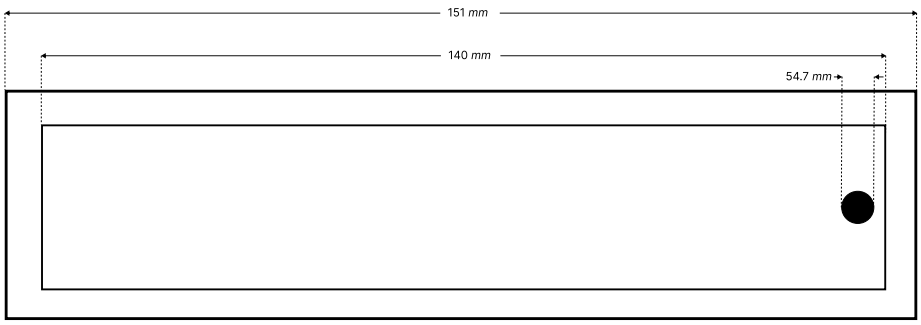

Figure C.1: Schematic of epoxy sample fabrication mold.

C.2 Mechanical Properties

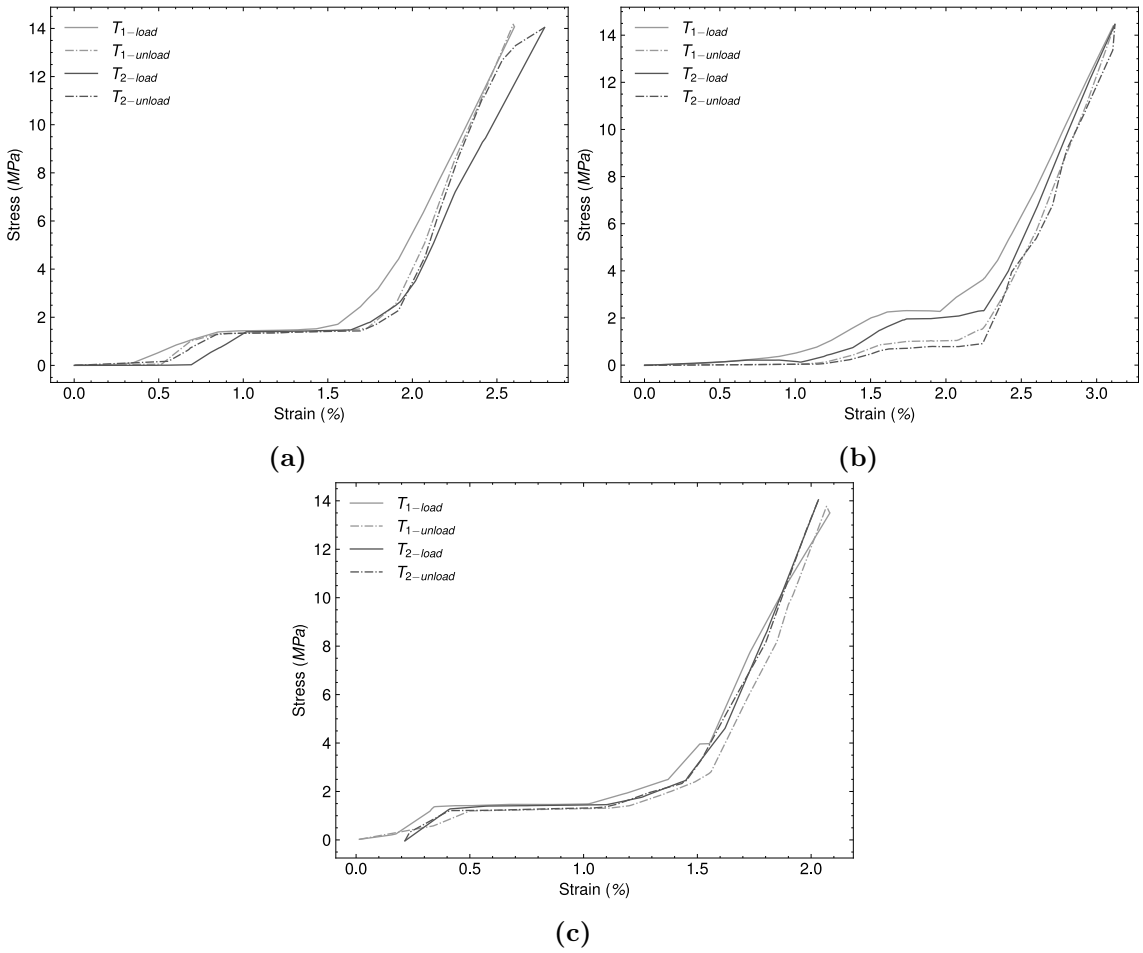

Figure C.2: Two successive cycles load-unload tensile test samples at a strain rate of 5 $mm \cdot s^{-1}$ and initial temperature of 20 ℃.

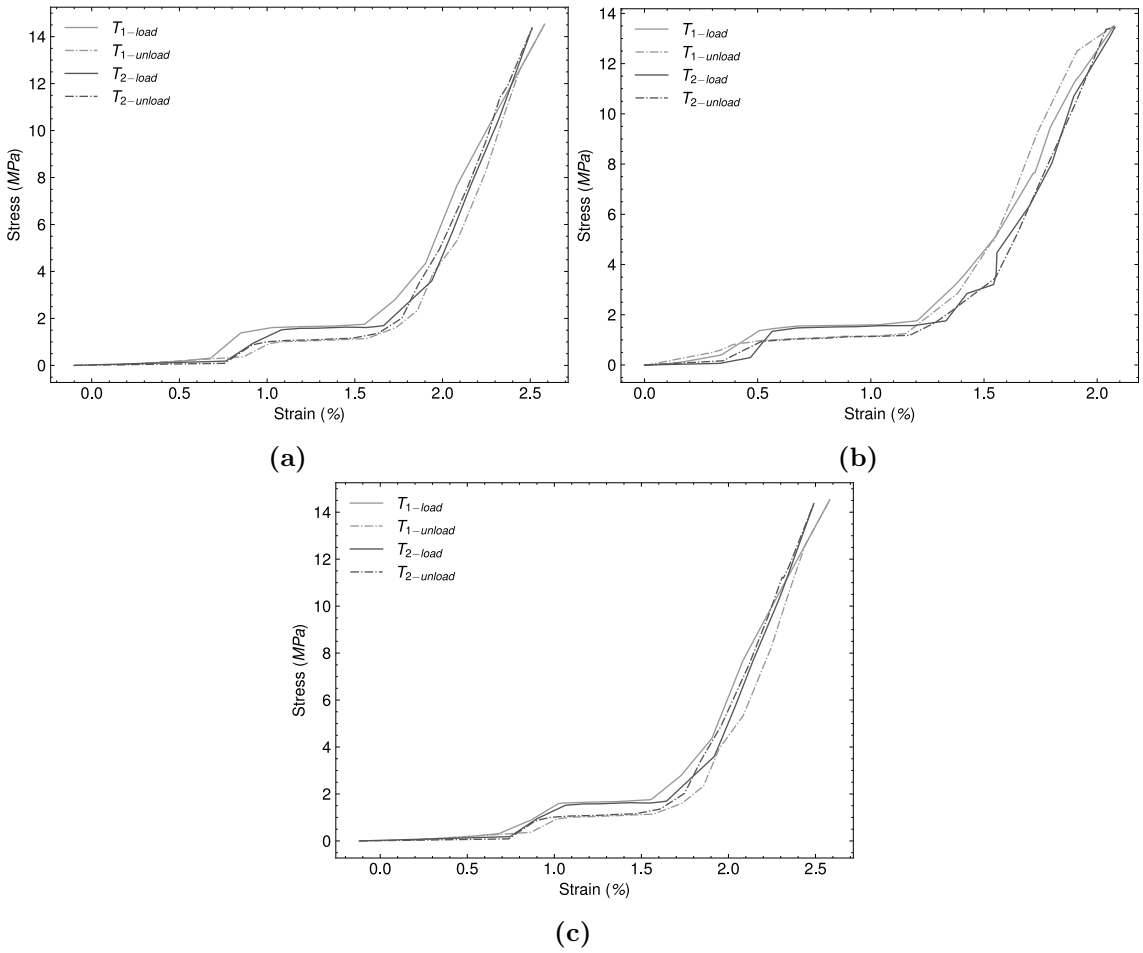

Figure C.3: Two successive cycles of load-unload tensile tests on thin epoxy samples at a strain rate of 8 $mm \cdot s^{-1}$ and initial temperature of 20 ℃.

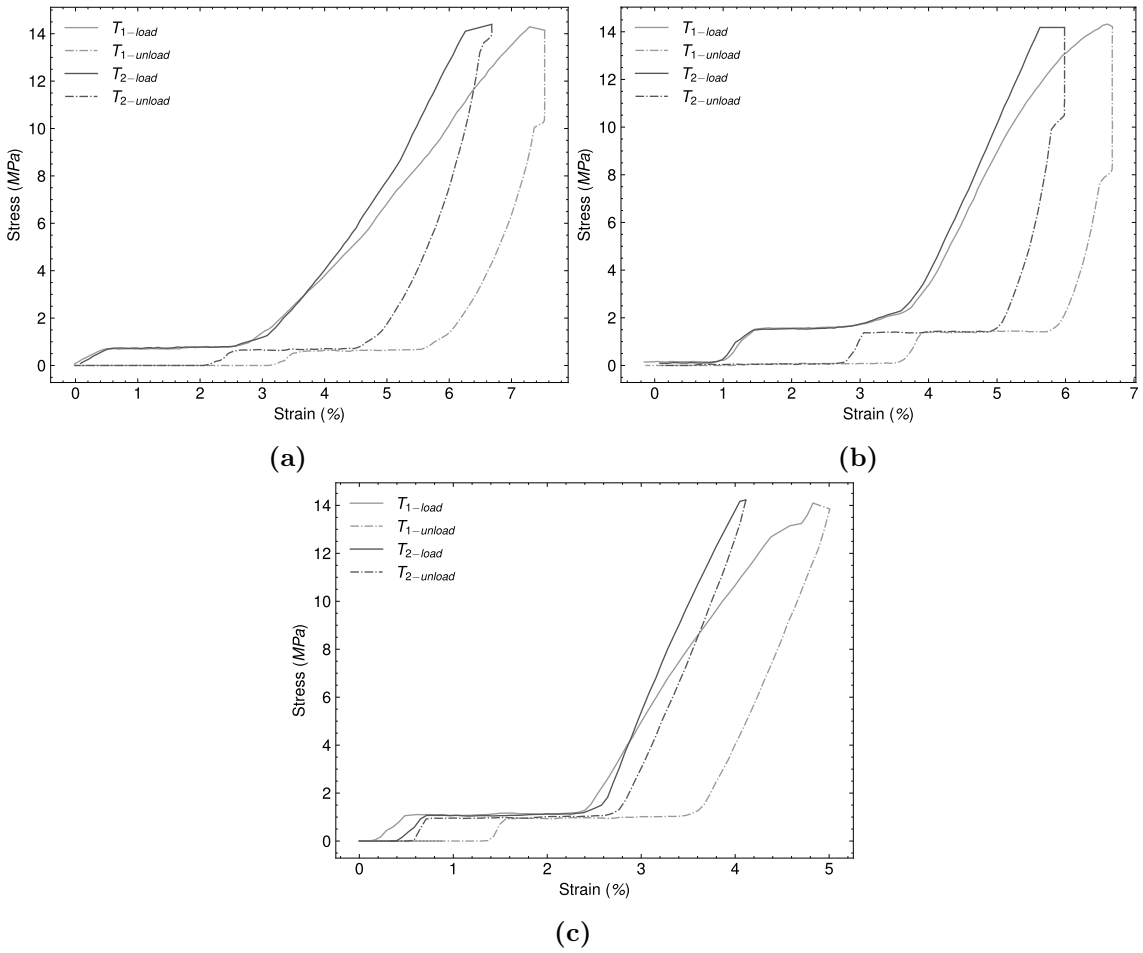

Figure C.4: Two successive cycles load-unload tensile test samples at a strain rate of 5 $mm \cdot s^{-1}$ and initial temperature of 30 ℃.

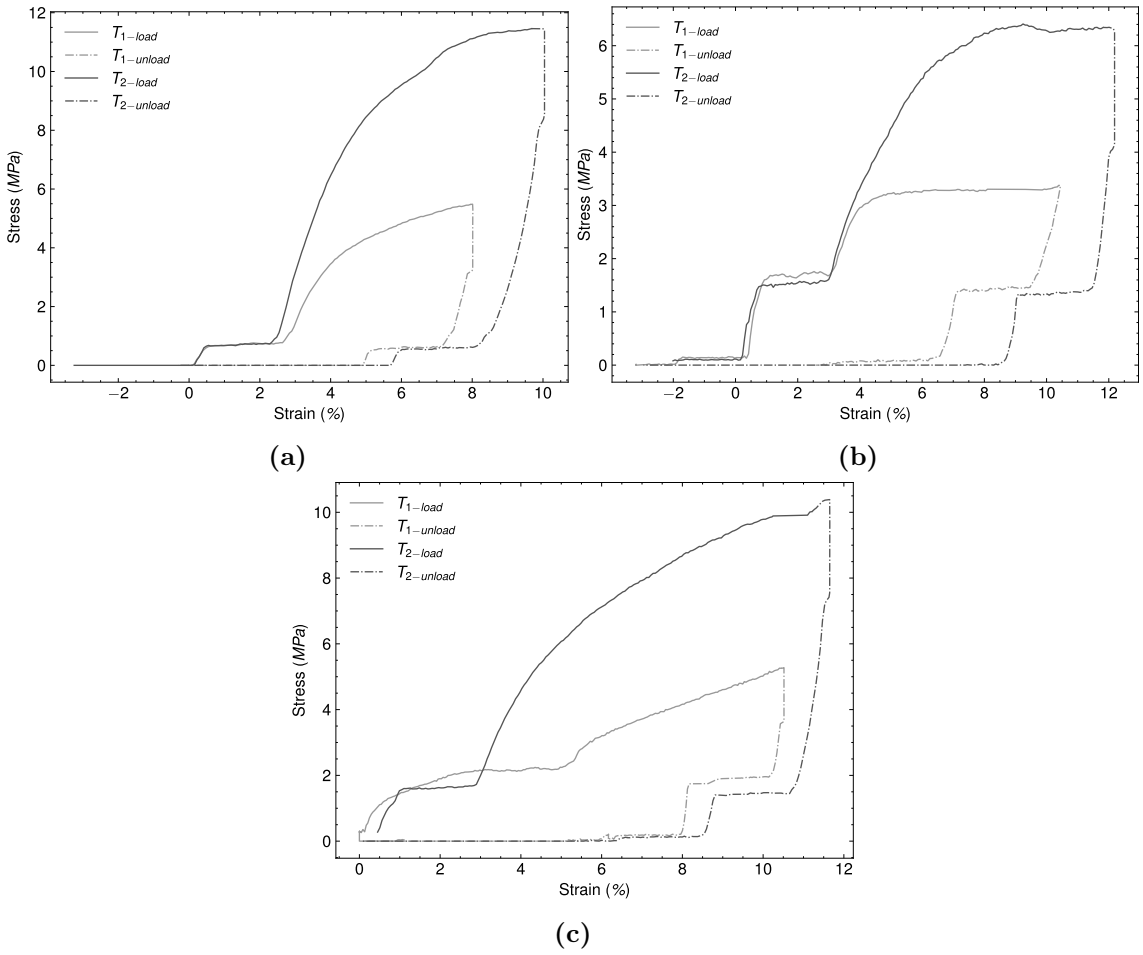

Figure C.5: Two successive cycles of load-unload tensile test thin epoxy samples at a strain rate of 5 $mm \cdot s^{-1}$ and initial temperature of 50 ℃.

Appendix D

Actuator Evaluation

D.1 Effects due to Fibre Diameter

D.1.1 Mechanical Properties

Table D.1: Monotonic to Failure Uniaxial Summary of 200 μm Carbon Nanotube Pre-twisted Samples

Sample	Tensile Strength (MPa)	Ultimate Strain ($\%$)	Necking Strain ($\%$)	Young's Modulus ($GPa \cdot m^{-1}$)	Toughness ($MJ \cdot m^{-3}$)
s_{13}	1465	12.4	2.45	12.07	75.87
s_{14}	1234.70	14.37	5.40	8.59	86.79

Table D.2: Monotonic to Failure Uniaxial of 200 μm Carbon Nanotube Twisted-Coiled Samples

Sample	Tensile Strength (MPa)	Ultimate Strain ($\%$)	Necking Strain ($\%$)	Young's Modulus ($GPa \cdot m^{-1}$)	Toughness ($MJ \cdot m^{-3}$)
s_{15}	203.24	39.29	12.22	0.52	22.44

Table D.3: Monotonic to Failure Uniaxial of 200 μm Carbon Nanotube Stiffness-Variable Samples

Sample	Tensile Strength (MPa)	Ultimate Strain ($\%$)	Necking Strain ($\%$)	Young's Modulus ($GPa \cdot m^{-1}$)	Toughness ($MJ \cdot m^{-3}$)
s_{16}	423.83	206.68	105.34	0.21	370.83
s_{17}	626.53	107.17	33.70	0.58	222.32

D.1.2 Electrothermal Response

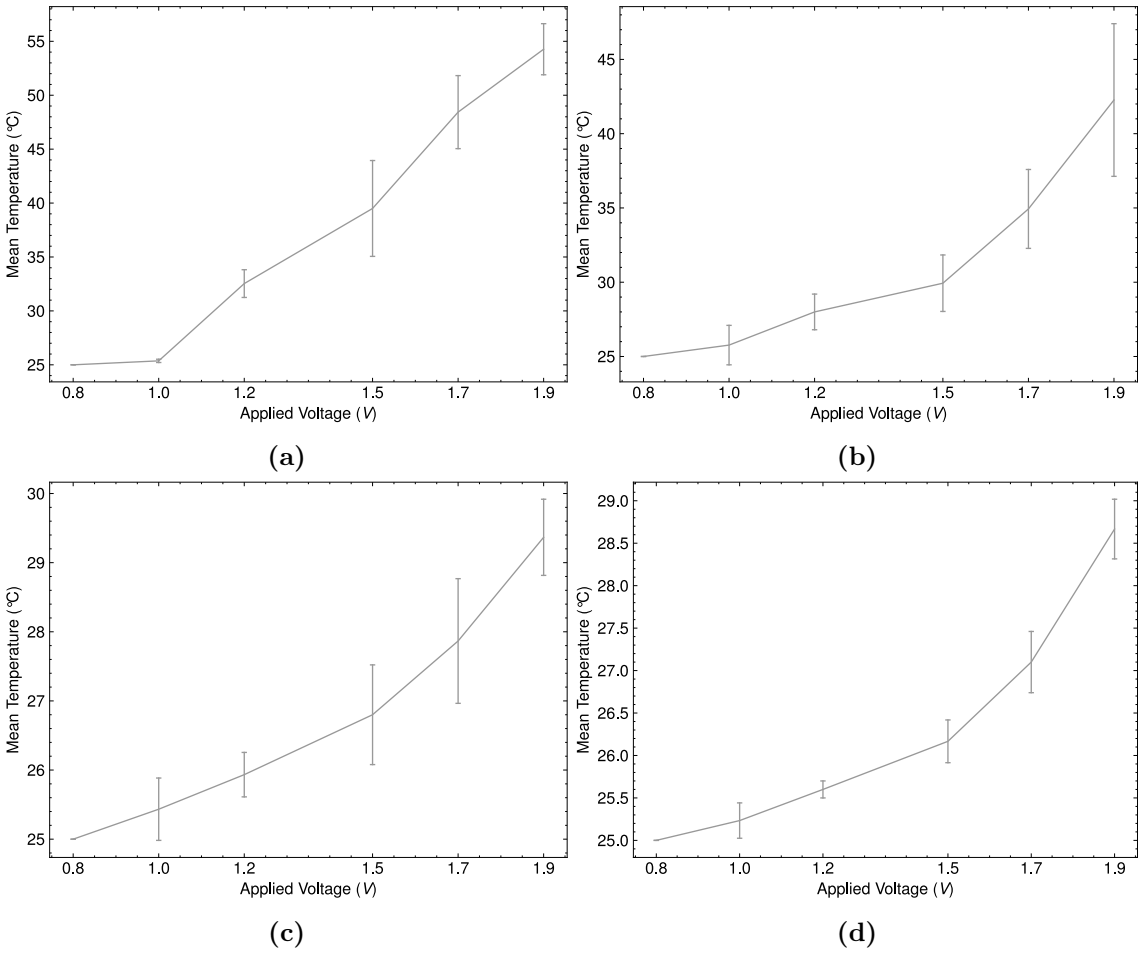

Figure D.1: Mean temperature vs applied voltage of three fabricated samples with 100 (left) and 200 (right) μm products in the (a) and (b) stiffness-variable, and the (c) and (d) twisted-coiled designs.

D.1.3 Electromechanical Response

Table D.4: Isometric Test Summary of 100 μm Carbon Nanotube Stiffness-Variable Samples with 20% Pre-stretch

Sample	Contractile Stress (MPa)					
	0.8 V	1.0 V	1.2 V	1.5 V	1.7 V	1.9 V
s_1	5.09	7.64	18.97	30.43	30.43	30.43
s_2	4.07	10.19	17.74	24.45	28.27	26.99
s_3	5.86	9.68	18.97	24.83	27.45	29.92

Table D.5: Isometric Test Summary of 200 μm Carbon Nanotube Stiffness-Variable Samples with 20% Pre-stretch

Sample	Contractile Stress (MPa)					
	0.8 V	1.0 V	1.2 V	1.5 V	1.7 V	1.9 V
s_4	0.80	1.27	2.39	3.15	3.69	2.93
s_5	1.02	1.59	2.55	3.57	4.01	3.06
s_6	0.95	1.11	2.23	4.01	4.33	3.63

Table D.6: Isometric Test Summary of 100 μm Carbon Nanotube Twisted-Coiled Samples with 20% Pre-stretch

Sample	Contractile Stress (MPa)					
	0.8 V	1.0 V	1.2 V	1.5 V	1.7 V	1.9 V
s_7	9.80	12.61	19.48	24.19	36.16	35.52
s_8	5.93	6.79	10.22	20.08	24.10	33.87
s_9	6.75	9.17	14.04	16.97	26.62	35.21

Table D.7: Isometric Test Summary of 200 μm Carbon Nanotube Twisted-Coiled Samples with 20% Pre-stretch

Sample	Contractile Stress (MPa)					
	0.8 V	1.0 V	1.2 V	1.5 V	1.7 V	1.9 V
s_{10}	1.75	2.32	4.65	5.06	5.60	6.75
s_{11}	1.27	2.32	3.26	5.59	7.61	7.70
s_{12}	2.01	2.51	3.79	5.08	6.24	6.97

Table D.8: Isotonic Test Summary of 100 μm Carbon Nanotube Stiffness-Variable Samples with 20% Pre-stretch

Sample	Contractile Strain (%)					
	0.8 V	1.0 V	1.2 V	1.5 V	1.7 V	1.9 V
s_1	0.00	0.00	0.16	0.25	0.54	0.82
s_2	0.07	0.20	0.30	0.31	0.60	0.88
s_3	0.00	0.05	0.29	0.36	0.45	0.82

Table D.9: Isotonic Test Summary of 200 μm Carbon Nanotube Stiffness-Variable Samples with 20% Pre-stretch

Sample	Contractile Strain (%)					
	0.8 V	1.0 V	1.2 V	1.5 V	1.7 V	1.9 V
s_4	0.00	0.03	0.00	0.00	0.06	0.17
s_5	0.00	0.00	0.00	0.05	0.09	0.14
s_6	0.04	0.00	0.00	0.00	0.07	0.13

Table D.10: Isotonic Test Summary of 100 μm Carbon Nanotube Twisted-Coiled Samples with 20% Pre-stretch

Sample	Contractile Strain (%)					
	0.8 V	1.0 V	1.2 V	1.5 V	1.7 V	1.9 V
s_7	0.00	0.00	0.05	0.07	0.21	0.29
s_8	0.00	0.00	0.07	0.07	0.24	0.30
s_9	0.00	0.12	0.18	0.24	0.41	0.41

Table D.11: Isotonic Test Summary of 200 μm Carbon Nanotube Twisted-Coiled Samples with 20% Pre-stretch

Sample	Contractile Strain (%)					
	0.8 V	1.0 V	1.2 V	1.5 V	1.7 V	1.9 V
s_{10}	0.00	0.17	0.22	0.28	0.42	0.52
s_{11}	0.07	0.28	0.14	0.28	0.21	0.38
s_{12}	0.04	0.00	0.14	0.22	0.27	0.36

D.2 Effects due to Pre-stretch Percentage

D.2.1 Electromechanical Response

Table D.12: Isometric Test Summary of 100 μm Carbon Nanotube Stiffness-Variable Samples with Selected Pre-stretch

Sample	Contractile Stress (MPa)					
	0.8 V	1.0 V	1.2 V	1.5 V	1.7 V	1.9 V
s_1	4.97	5.35	6.24	12.86	17.19	21.52
s_2	4.33	4.97	6.02	9.99	13.43	18.67
s_3	5.47	6.37	8.79	18.97	24.45	28.65
s_4	4.75	5.95	7.26	16.48	22.14	25.83
s_5	5.09	9.68	18.97	24.83	27.45	29.92
s_6	4.07	10.19	17.74	24.45	28.27	26.99
s_7	4.90	5.88	7.95	9.97	11.90	14.90
s_8	5.30	6.72	7.66	9.27	11.60	17.12

Table D.13: Isometric Test Summary of 100 μm Carbon Nanotube Twisted-Coiled Samples with Selected Pre-stretch

Sample	Contractile Stress (MPa)					
	0.8 V	1.0 V	1.2 V	1.5 V	1.7 V	1.9 V
s_{9a}	4.97	7.64	10.95	16.93	22.28	29.16
s_{9b}	8.79	10.57	16.42	18.46	23.05	32.85
s_{9c}	9.80	12.61	19.48	24.19	36.16	35.52
s_{9d}	9.42	14.26	21.52	35.01	40.11	45.07
s_{10a}	4.93	8.44	12.49	14.13	16.87	22.92
s_{10b}	5.47	8.91	13.11	14.61	25.66	34.12
s_{10c}	6.75	9.17	14.04	16.97	26.62	35.21
s_{10d}	7.13	10.06	15.72	21.77	34.89	48.81
s_{11a}	4.42	5.61	7.05	11.31	15.48	25.68
s_{11b}	5.09	6.12	12.75	19.42	22.62	28.78
s_{11c}	5.93	6.79	10.22	20.08	24.10	33.87
s_{11d}	6.75	7.08	11.33	21.10	29.37	39.13

Table D.14: Isotonic Test Summary of 100 μm Carbon Nanotube Stiffness-Variable Samples with Selected Pre-stretch

Sample	Contractile Strain (%)					
	0.8 V	1.0 V	1.2 V	1.5 V	1.7 V	1.9 V
s_1	0.00	0.04	0.04	0.10	0.17	0.34
s_2	0.00	0.00	0.00	0.08	0.13	0.45
s_3	0.05	0.07	0.20	0.51	0.41	0.76
s_4	0.04	0.03	0.18	0.24	0.36	0.54
s_5	0.07	0.20	0.30	0.31	0.60	0.88
s_6	0.00	0.05	0.29	0.36	0.45	0.82
s_7	0.00	0.00	0.05	0.14	0.23	0.55
s_8	0.00	0.00	0.05	0.23	0.41	0.57

D.3 Effects due to Coating Application Interval

D.3.1 Electromechanical Response

Table D.15: Isometric Test Summary of 100 μm Carbon Nanotube Stiffness-Variable Samples with 10 *min* Coating Application Interval

Sample	Contractile Stress (MPa)					
	0.8 V	1.0 V	1.2 V	1.5 V	1.7 V	1.9 V
s_1	5.09	5.73	7.13	14.64	20.50	26.10
s_2	5.47	6.37	8.79	18.97	24.45	28.65
s_3	4.75	5.95	7.26	16.48	22.14	25.83

Table D.16: Isometric Test Summary of 100 μm Carbon Nanotube Stiffness-Variable Samples with 20 *min* Coating Application Interval

Sample	Contractile Stress (MPa)					
	0.8 V	1.0 V	1.2 V	1.5 V	1.7 V	1.9 V
s_4	4.84	5.09	8.40	15.41	18.08	21.90
s_5	3.95	5.09	8.02	15.15	17.70	20.24
s_6	4.46	5.35	6.37	13.50	15.15	19.74

Table D.17: Isometric Test Summary of 100 μm Carbon Nanotube Stiffness-Variable Samples with 30 *min* Coating Application Interval

Sample	Contractile Stress (MPa)					
	0.8 V	1.0 V	1.2 V	1.5 V	1.7 V	1.9 V
s_7	0.00	2.55	3.06	6.11	10.25	12.24
s_8	0.00	0.00	2.16	2.57	3.59	8.72
s_9	0.00	1.27	4.71	6.96	10.25	15.85

Table D.18: Isotonic Test Summary of 100 μm Carbon Nanotube Stiffness-Variable Samples with 10 *min* Coating Application Interval

Sample	Contractile Strain (%)					
	0.8 V	1.0 V	1.2 V	1.5 V	1.7 V	1.9 V
s_1	0.00	0.00	0.14	0.25	0.36	0.53
s_2	0.05	0.07	0.20	0.51	0.41	0.76
s_3	0.04	0.03	0.18	0.24	0.36	0.54

Table D.19: Isometric Test Summary of 100 μm Carbon Nanotube Stiffness-Variable Samples with 20 *min* Coating Application Interval

Sample	Contractile Strain (%)					
	0.8 *V*	1.0 *V*	1.2 *V*	1.5 *V*	1.7 *V*	1.9 *V*
s_4	0.00	0.16	0.38	0.49	0.72	1.27
s_5	0.05	0.05	0.19	0.33	0.62	0.76
s_6	0.05	0.00	0.25	0.39	0.57	0.73

Table D.20: Isometric Test Summary of 100 μm Carbon Nanotube Stiffness-Variable Samples with 30 *min* Coating Application Interval

Sample	Contractile Strain (%)					
	0.8 *V*	1.0 *V*	1.2 *V*	1.5 *V*	1.7 *V*	1.9 *V*
s_7	0.00	0.02	0.00	0.36	0.37	0.39
s_8	0.06	0.04	0.15	0.27	0.15	0.44
s_9	-0.04	-0.02	0.06	0.41	0.37	0.39